University of Canterbury

Doctoral Thesis

Bubbles, Crystals and Cracks in Cooling Magma

Author:

Felix Wendelin von Aulock

Supervisors:

Dr. Ben Kennedy

Dr. Chris Oze

A thesis submitted in fulfilment of the requirements

for the degree of Doctor of Philosophy

in the

Department of Geological Sciences

June 2013

"Bestaubt sind unsere Bücher, der Bierkrug macht uns klüger. Das Bier schafft uns Genuss, die Bücher nur Verdruss."

Johann Wolfgang von Goethe

UNIVERSITY OF CANTERBURY

Abstract

College of Science

Department of Geological Sciences

Doctor of Philosophy

Bubbles, Crystals and Cracks in Cooling Magma

by Felix Wendelin von Aulock

Ascent of magma results in drastic drops of pressure and temperature during eruption. Exsolution or dissolution of water changes the physical and chemical properties of the magma and can promote or inhibit the formation of bubbles, crystals and cracks. The microstructural relations between bubbles, crystals and cracks are important records of processes immediately before and during volcanic eruptions and during deposition of volcanic products. This is an integrated study of analyses, conceptual and numerical models of textural relations, and water distribution patterns of natural and experimentally altered samples. Synchrotron Fourier transform infrared spectroscopy and focal plane array detectors open new possibilities for the analysis of the spatial distribution of volatiles in volcanic rocks. New ways of sample preparation, measurements and data analyses helped to create water distribution maps with spatial resolutions that are close to the diffraction limit ($\approx 3\ \mu$m). In order to constrain eruptive processes and mechanisms of lava emplacement, I describe textural features in volcanic glasses including bubbles, flow bands of crystals or bubbles, spherulites and different generations of cracks. In experiments, bubbles were grown under isobaric conditions, at one or two cooling steps,

their textures were described and volume changes tracked. Water distribution patterns in the glass around the textures were described and categorized, and where possible, diffusion modeling was used to infer temperature- and timescales of formation. Rocks that are quenched within short periods of time after bubble growth preserve negative gradients of water toward the bubble margins. These gradients are generally not observed if the sample is kept at high temperatures for extended periods. If, however, a second step of cooling is added, water may be re-dissolved into the surrounding melt, which may lead to the complete resorption of bubbles. A conceptual of water redistribution during bubble resorption or collapse is used to interpret water heterogeneities across linear flow banding. These heterogeneities can be caused by shearing of bubbly magma, leading to collapse, degassing and resorption of water into the melt, creating a bubble free melt. Anhydrous spherulitic crystals grow both above and below the glass transition temperature (T_{g}) redistributiong water into the surrounding melt. Below T_{g}, cracks form and are successively hydrated by magmatic water from crystal growth or by meteoric water at temperatures far below T_{g}. The hydrated perlitic cracks in the samples of this study formed at elevated temperatures and are distinct from cracks formed at ambient temperatures without hydrated margins. This study shows that the heterogeneous distribution of water in volcanic rocks preserves the complex and non-linear degassing and cooling history of eruptive products. The timescales and temperatures discovered here provide new ways to interpret textural observations, water distribution patterns and signals of shallow volcanic unrest.

Acknowledgements

Thank you ...

- Ben Kennedy for believing in me, taking your time for me, supporting me and teaching me!
- Chris Oze for being the best editor in the world, showing me how it's done and for helping me even in the moments of greatest sleep deprivation!
- Both my supervisors Ben and Chris together, who are a perfect team!
- My family for being so supportive despite the fact that I was so far away and didn't make up for all the goodness you sent down under! Ich liebe euch!
- Alex Nichols for welcoming me in Japan and helping me with great patience with my first publication.
- Signe and Kathy for sharing their partners!
- Eva, for taking care that I didn't go crazy, didn't starve, did sleep, did do some exercise, didn't drink too much ... you're making me happy!
- Paul Ashwell for almost all the same reasons at times.
- Jackie, you are awesome!
- Fabian, thanks for asking tons of questions! And thank you for being a great scientist and friend.
- Flo, Toni, and Paul for their help at the Synchrotron.
- The department of Geological Sciences at the University of Canterbury for being such a great bunch of people. Especially and in no particular order ...
- The lecturers and staff!
- The postgraduate students and other friends that have been my family for all this time!
- In no particular order, really! Jon de Lux, Bermuda Johnny, Marie-Claude, Flo, Joh, Theo and Pinelopi, James, Rose, Stu, Vicky, Tom, Tory and Greg, Tim, Brendan, Elke, Louise, Louise, Lauren, Kris, Paul, Josh, Melissa and Simon, Ali, Sabrina, Simon, Oshi, Lizzy and Paul, Emily and Tim, Emily, Emma, Camilla, Katrin, Dan, Dan, ...

- The people of Canterbury for being so strong and giving so much support in difficult times! Kia Kaha!
- The College of Science for the Doctoral Scholarship.
- GNS Science for their financial support.
- DAAD (German Academic Exchange Service) for their financial Service.
- Dr. Danielle Martin and Dr. Mark Tobin for their help at the IRM beamline of the Australian Synchrotron
- The Australian Synchrotron and the New Zealand Synchrotron Group for granting beamtime and travel funds.
- Sabrina Ke for helping me with the furnace.
- Colin Wilson for giving me a sample from Mayor Island!
- Rob Spiers for teaching me how to polish.
- The scientists around the world who taught me and discussed with me at JAMSTEC, Uni Lancaster, LMU Munich, Massey University, Victoria University and at conferences.
- And many, many more ...

Contents

List of Figures

List of Tables

List of Publications

This is a short overview of the publications that are currently under preparation or have been published as peer reviewed articles and conference presentations. All of these are based on the work I did during my doctoral degree, however, some of them are not relevant to the topic of this thesis and are therefore not included as part of this doctoral thesis. I am a leading author or co-author on all these papers, and I contributed to (1) fieldwork or experimental work, (2) results analysis and intellectual discussion, and (3) editing of the manuscripts, in all cases.

- Chapter 5: **F. W. von Aulock**, A. R. L. Nichols, B. M. Kennedy, and C. Oze, Timescales of texture development in a cooling lava dome, Geochimica et Cosmochimica Acta, Mar. 2013. [177].
- Chapter 2: **F. W. von Aulock** et al., Advances in Fourier transform infrared spectroscopy of natural glasses: From sample preparation to data analysis, *in prep.* Invited Review Article for *Lithos*[1].
- Chapter 3: **F. W. von Aulock** et al., Water diffusion during bubble growth in magma, *in prep.* for *Earth and Planetary Science Letters.*
- Chapter 4: **F. W. von Aulock** et al., Flow band formation in vesicular magma, *in prep.* for Special Issue *Textural Evolution of Volcanic Rocks: Investigating Magma Rheology, Petrology, and Eruptive Processes* in *American Mineralogist.*
- P. A. Ashwell, J. W. Cole, B. M. Kennedy, D. M. Gravley, and **F. W. von Aulock**, Insights into caldera and regional structures and magma body distribution from lava domes at Rotorua Caldera, New Zealand, Journal of Volcanology and Geothermal Research, vol. Accepted, 2013 [5].
- F. B. Wadsworth, B. M. Kennedy, M. J. Branney, Y. Lavalle, **F. W. von Aulock**, B. Cordonnier, J. Vasseur, and D. B. Dingwell, Textures and dynamics of magma draining from a late-stage basaltic-andesite dyke, *in prep.* for *Geology.*

Conference presentations:

- **F. W. Von Aulock**, B. Kennedy, C. Oze, and P. A. Ashwell, Isobaric bubble growth and collapse in magma, IAVCEI Kagoshima, 2013.

[1]This is going to be a collaboration between many scientists who will add important information about the advances in the analytics of melt inclusions or basaltic glasses. However, none of the collaborating authors were involved in the work for this chapter.

- **F. W. Von Aulock**, B. M. Kennedy, C. Oze, Y. Lavallee, A. R. Nichols, K.-U. Hess, and P. A. Ashwell, The formation and hydration of cracks in cooling volcanic glass, IAVCEI Kagoshima, 2013.

- **F. W. Von Aulock**, C. Oze, B. Kennedy, T. Cox, F. Bégué, and P.A. Ashwell, Distribution of Water Related to Flow Banding and Microlites in Obsidian, Geosciences 2011 Conference, Nelson, New Zealand. 2011.

- **F. W. Von Aulock**, C. Oze, B. Kennedy, F. Bégué, The Distribution of Water in Collapsing Foams of Magma, Geosciences 2011 Conference, Nelson, New Zealand. 2011.

- **F. W. Von Aulock**; Nichols, A. R.; Tuffen, H.; Wadsworth, F. B.; Ashwell, P. A.; Kennedy, B. (2010), Hydration of a Rhyolitic Magma by Spherulite Growth, 2010 Fall Meeting, AGU, San Francisco,

- **F. W. Von Aulock**, A. R. L. Nichols, F. Wadsworth, P. A. Ashwell, H. Tuffen, B. Kennedy (2010). Hydration Of A Rhyolitic Magma By Spherulite Growth., GeoNZ 2010 Conference, Auckland, New Zealand.

- Wadsworth, F. B.; **F. W. Von Aulock**.; Kennedy, B.; Branney, M.; Bardsley, C. J. (2010), The death of a Strombolian eruption: Evidence for dyke drainage from Red Crater, Tongariro volcano, New Zealand, 2010 Fall Meeting, AGU, San Francisco, Calif., 13-17 Dec.

- Ashwell, P.; Kennedy, B. M.; Buchanan, K.; Drabble, D.; **von Aulock F. W.** (2009), Volcano in the basement, a new experimental rig for the development of volcanic textures, Eos Trans. AGU, 90(52), Fall Meet. Suppl., Abstract V13B-2025,

- F. Wadsworth, **F. W. Von Aulock**, C. Bardsley, B. Kennedy, M. Branney, The Death Of A Strombolian Eruption: Evidence Of Dike Drainage From Red Crater, Tongariro Volcano., GeoNZ 2010 Conference, Auckland, New Zealand.

- P. A. Ashwell, B. Kennedy, **F. W. Von Aulock**, J. Cole, Eruption Style And Emplacement Processes Of Ngongotaha Dome, Rotorua. GeoNZ 2010 Conference, Auckland, New Zealand.

- P.A. Ashwell, B. Kennedy, **F. W. Von Aulock**, K. Buchanan, D. Drabble and J. Cole (2009). Playing Vulcan: Re-Creating The Subterranean Conditions That Spawn Rocks., Geosciences 09 Conference, Oamaru, New Zealand.

Chapter 1

Introduction

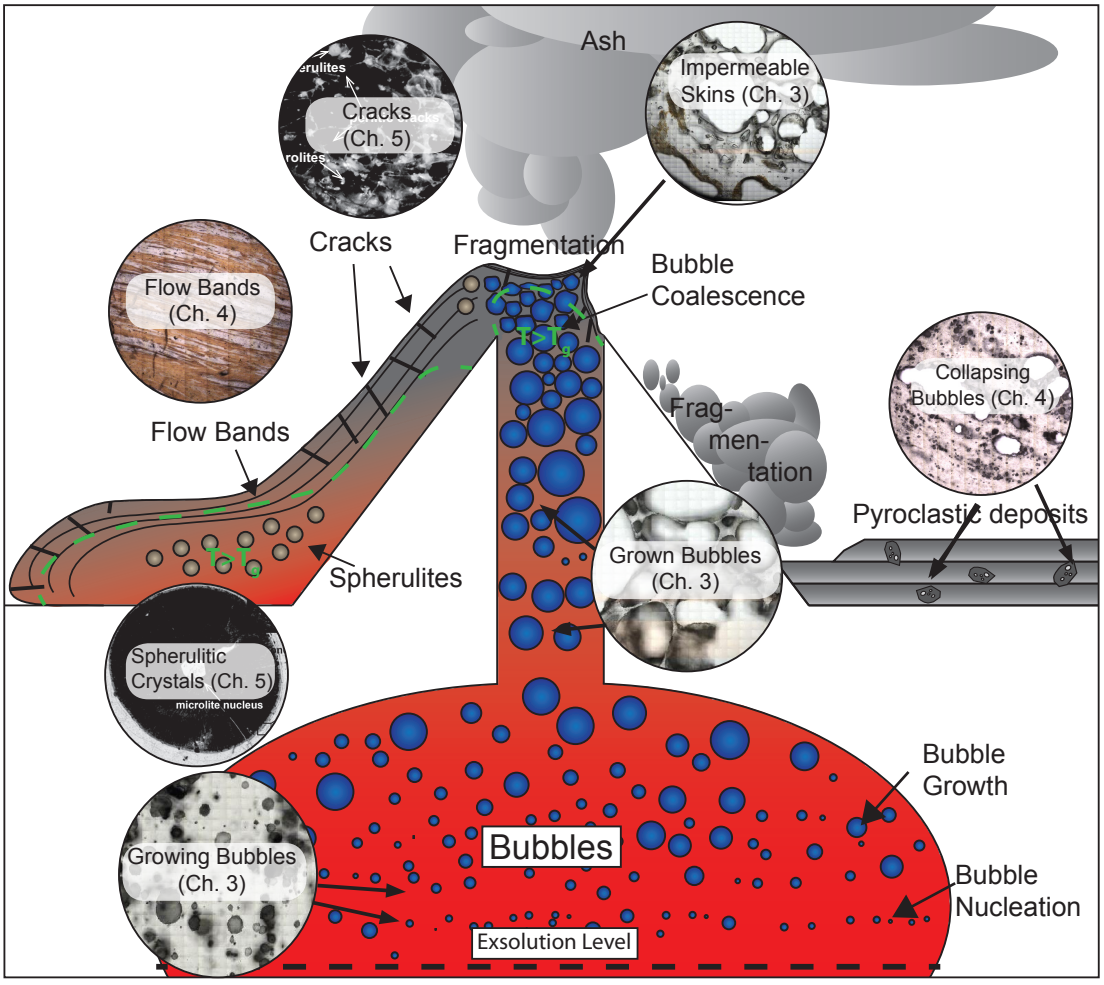

FIGURE 1.1: Common textures in magma evolve during ascent, eruption and emplacement. The formation of bubbles, flow bands, crystals and cracks occurs over wide ranges of temperatures and is associated with water redistribution.

1.1 Abstract

Magma consists of silicate melt or glass, bubbles, cracks and crystals in varying proportions (Fig. 1.1). Textural relations of these constituents are one of the major tools of volcanology that aid in interpreting the dynamic processes before, during and after a volcanic eruption [10, 24, 88, 102, 137, 143, 145, 173, 187]. Silicate melts are a connected network of (mostly) silica tetrahedrons with short-range order. When the temperature drops below the glass transition temperature (T_g), the structure of the melt is frozen in, and the supercooled melt behaves as a brittle, solid glass. The glass transition temperature is defined as the onset of the change in a physical property [108] e.g. viscosity [59, 182], the thermal expansion coefficient [123] or the heat capacity of the glass [127, 168]. Therefore, the glass transition not only depends on the chemical composition (e.g. on the water content), it is also determined by the state of relaxation of the glass and, therefore, its thermal history [43]. T_g is a key discussion topic in all chapters in this thesis, as crossing T_g can mark transitions in eruption style from effusive to explosive [43] (Fig. 1.1).

1.2 Water in magmas and melts

The solubility of water highly depends on pressure [40, 71, 90, 105], temperature [71, 138, 191] and composition [71, 120, 138] of the melt (Fig. 1.2).

Water is a main volatile constituent of melt inclusions in crystals, which are quenched and isolated during crystallization. These inclusions can contain water contents of up to 8 wt.% [e.g. 178, 179]. The degassed volcanic products, however, usually contain $\lesssim$1 wt.% water which corresponds to the low pressures the melt experiences before eruption and quenching [e.g. 24, 119](Chapters 3 and 4). Exceptions exist in perlitic glass which can show up to ≈10 wt.% H_2O[e.g. 38](5). How the water gets oversaturated remains unknown and there is a lack of solubility data in intermediate temperatures between atmospheric temperatures (relevant for archeological artefacts of natural glass [2]) and magmatic temperatures [105]. I present data of hydration that ranges from magmatic temperatures during bubble growth (Chapter 3) to temperatures of emplacement (Chapter 4) and post-emplacement alteration (Chapter 5) covering temperatures from 850 °C to ambient temperatures of ≈10 °C. Stolper [159] could show that water is dissolved as two species: molecular water (H_2O) and hydroxyl groups (OH^-) which interconvert in an equilibrium reaction:

$$H_2O_m(melt) + O^{2-}(melt) \rightleftharpoons 2OH^-(melt) \tag{1.1}$$

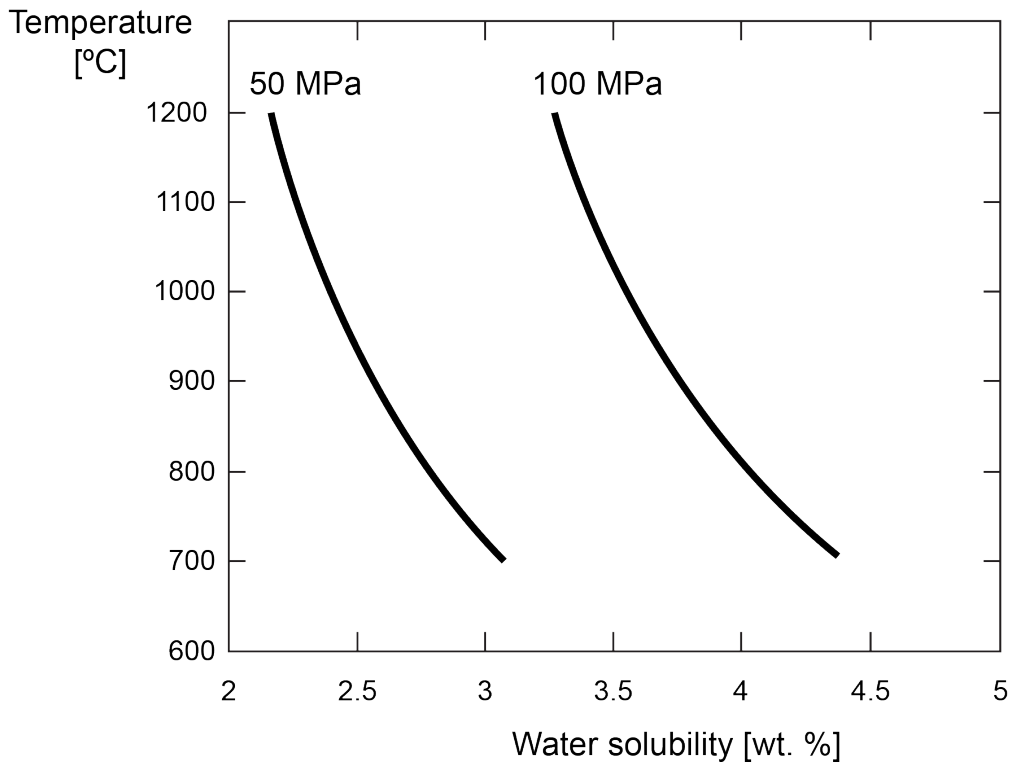

FIGURE 1.2: Water solubilities in rhyolitic melts at different pressures and temperatures (note the higher solubilities at lower temperatures). Modified figure from Yamashita [191]

This equilibrium reaction is only appropriate above T_g (or rather the fictive temperature, which is equal to T_g in a relaxed melt) [196], making re-equilibration [130] below T_g unknown. Hydroxyl groups form a larger proportion of the total water than H_2O_m at low total water content. The proportion present as OH^-- decreases with increasing total water content [115, 130, 159, 159, 195]. The kinetics of re-equilibration has been suggested as a proxy for cooling timescales of degassing magma [198]. I discuss how different water species are measured in Chapter 2, and although I collected FTIR data on different water species (Appendix), I have omitted this data from the bulk of the thesis as the relevance and reproducibility of species data at low temperatures is still to poorly constrained [115].

1.3 Diffusion

The diffusion of water in melts and glass is covered by several review articles [e.g. 2, 196, 199]. At oxidizing conditions that prevail in most situations in magma presented in this study, diffusion of H_2 does not occur and water only diffuses as H_2O and OH^-. Of these two species, H_2O is the dominant diffusion species, whereas OH^- occurs mainly

due to interconversion of the two species, even at low water contents ($\lesssim$0.2 wt.% in the mentioned study of Zhang et al. [197]). At low water concentrations the diffusivity is approximately proportional to the total water content, whereas, at higher water content (>3 wt.%) this assumption does not match experimental data [196]. We used known rates of diffusivity to estimate timescales of volcanic processes in Chapters 3 and 5.

1.4 Impacts of water on the properties of magma

Water can account for up to 8 wt.% of the composition of the melt and physical properties of the melt are drastically changed by hydration and dehydration. Small amounts of water can drastically change the rheological properties of the melt because of its network modifying qualities (Fig. 1.3). The solution of water effectively creates non-bridging oxygens in the structure of the melt. This lowers the viscosity, T_{g} [68] and density [150] of the melt.

Diffusivity is directly proportional to the viscosity (based on the Einstein relation [47]) and, therefore, diffusive processes are generally faster at higher water contents. Diffusion is necessary for crystals or bubbles to grow. At very high viscosities, the growth of crystals can be completely inhibited leading to crystal free glass despite high bulk-oversaturation of the respective phases. In addition, if water is added to the melt, liquidus and solidus temperatures for most mineral phases are shifted to lower temperatures which may allow partial melting of the mantle in subduction zones [e.g. 176]. I discuss the interplay between water solubility, diffusion and viscosity as temperature changes as crystals and cracks form in Chapter 5 and as bubbles form in Chapter 3. Bubble nucleation and growth is largely controlled by viscosity and gas diffusion [e.g. 95, 99, 124, 166].

1.5 Bubble nucleation

During ascent, magma depressurizes, volatiles exsolve and bubbles nucleate (Fig. 1.1). Continued exsolution and limited growth creates overpressurization that may lead to an explosive or effusive volcanic eruption. Water exsolution is, therefore, a dominant driving force behind volcanic eruptions [147]. Bubble formation can occur by homogeneous and/or heterogeneous nucleation. Homogenous bubble nucleation is the nucleation of a bubble in a crystal- and bubble free melt. Initially, high energy is required to propagate bubble growth as melt surface tension acts to resist growth proportional to the bubble size; therefore, nucleation and initial growth requires high amounts of volatile supersaturation [98, 107]. Heterogeneous bubble nucleation is the nucleation of a bubble on phase

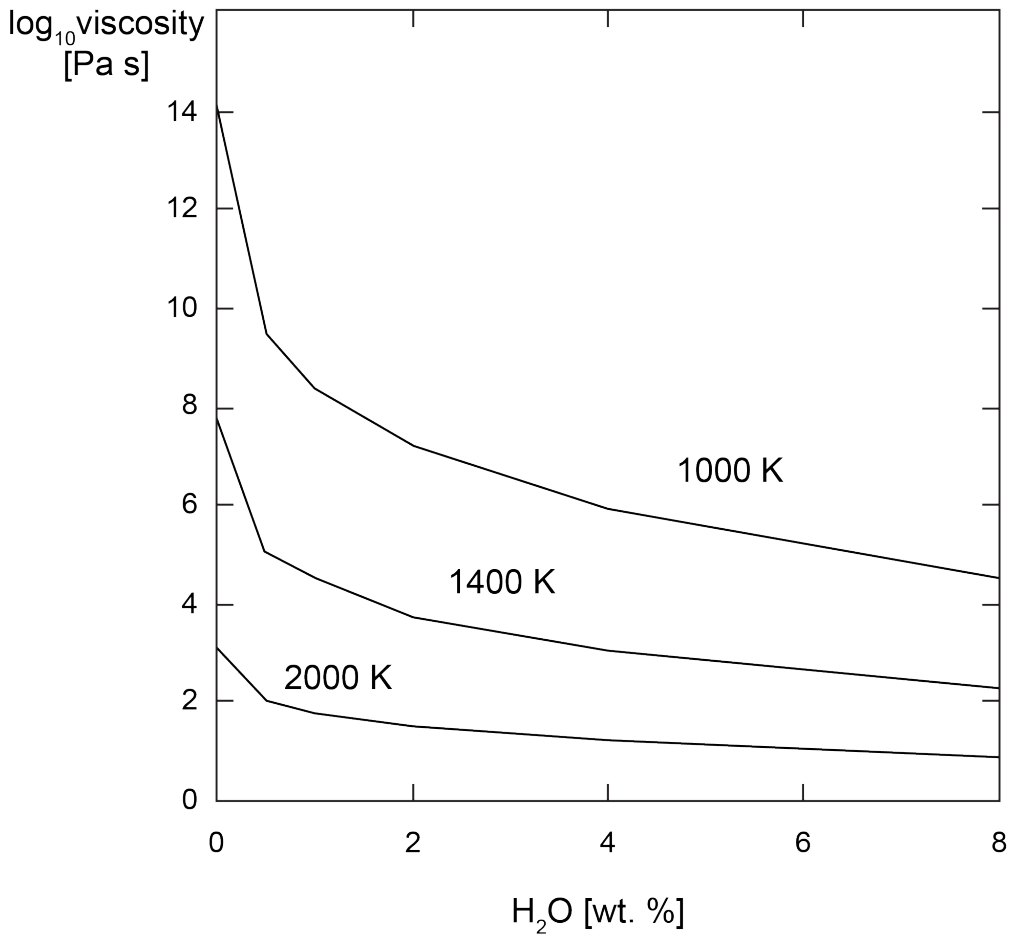

FIGURE 1.3: The viscosity of a hydrous granitic melt at different temperatures. Note that the decrease of viscosity is the most drastic for the first wt. % of water added. Modified after Hess and Dingwell [68]).

boundaries such as the surface of a microlite, inclusion, or xenolith. The heterogeneous bubble nucleation at a phase boundary is more efficient and does not require as high amounts of volatile supersaturation as homogeneous nucleation [74]. The bubble growth that I investigate in Chapter 3 follows a period of homogeneous bubble nucleation from a supersaturated crystal-free obsidian.

1.6 Bubble growth

Both depressurization and exsolution control the growth of bubbles [125]. Depressurization facilitates bubble growth in two ways: oversaturation of the melt in volatiles, and a decrease of the density of the volatiles. Volatiles diffuse into nucleated bubbles if the melt is oversaturated due to depressurization, temperature increase or changes in composition. The exsolution rate is controlled by the amount of oversaturation and the

diffusivity of the volatile exsolving [125]. After nucleation, the internal pressure in the small bubbles is high due to the melt surface tension acting on a high surface area to volume ratio, keeping growth rates low. As soon as the surface/volume ratio decreases with bubble growth, the relative effect of surface tension is reduced, and bubbles grow more rapidly.

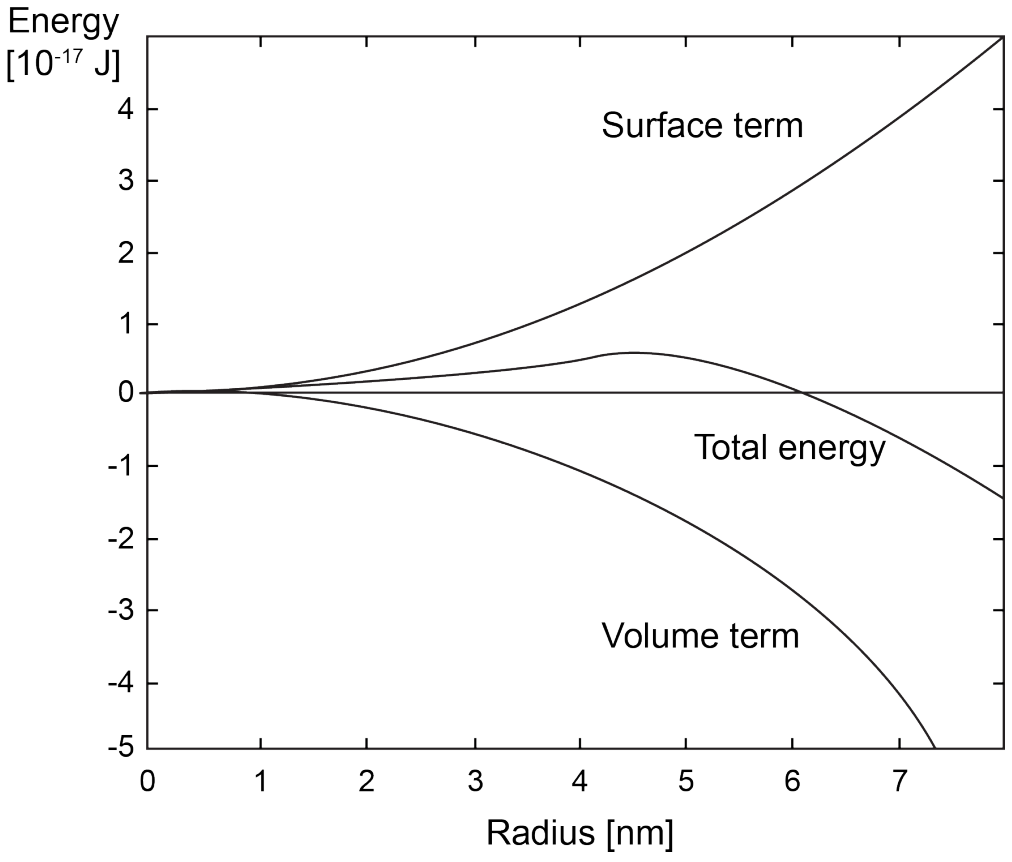

FIGURE 1.4: The energy of formation of a nucleus as a function of its radius. As soon as the surface term is overtaken by the volume term, the nucleus grows spontaneously. Modified after Navon and Lyakhovsky [110]

Bubble growth can be described by the Péclet number (Pe) [95], whether controlled by diffusion of water in melt or by viscosity. Pe is the product of the Reynolds number (the ratio of inertial to viscous forces of the melt) and the Schmidt number (the ratio of the momentum diffusivity to molecular diffusivity) or simplified, the ratio of timescale of diffusion ($t_d = R^2/D$ where R is the bubble radius and D is the diffusion coefficient) over the timescale of viscous deformation ($t_v = \eta/\Delta P$ where η is the viscosity and ΔP is the saturation pressure).

$$Pe = \frac{t_d}{t_v} = \frac{\Delta P R^2}{\eta D} \tag{1.2}$$

A purely diffusion controlled bubble growth takes place at Pe >1, whereas, a Pe <1 indicates a viscosity limited growth of bubbles. A supercooled melt below T_g, such as in a cooled lava dome, will not allow any bubble growth or collapse within reasonable timescales even though diffusion is still possible. As bubble growth is hindered, continued degassing and increasing overpressurisation of pores may lead to brittle fragmentation [111, 162]. The initial growth of bubbles in low viscosity magma, however, is purely controlled by the diffusion of water into the melt. Many studies have investigated the growth rates of bubbles during depressurization[e.g. 63, 86, 99, 110, 111, 166, 169, 170, 193]; however, these studies neglect bubble growth at isobaric conditions. Isobaric bubble growth is the case for stagnating magma in the magma chamber, conduit and for erupted volcanic products. Most volcanic products preserve either whole vesicles (such as in lava, pumice, scoria or large volcanic bombs) or shards of glass that represented bubble walls before fragmentation [129]. In Chapter 3, we investigate isobaric bubble growth in a lava as an oversaturated melt re-equilibrates.

1.7 Bubble coalescence and connectivity

Ostwald ripening of foam minimizes the surface/volume ratios of the existing bubbles: smaller bubbles are consumed by bigger bubbles through diffusion and average bubble sizes increase [85]. Coalescence is caused by the interaction of two or more bubbles and the rupture of the melt wall(s) that separate them, surface tension acts to retract the melt film(s) and re-round the new, larger bubble [62]. As the volumetric bubble/melt ratio increases during bubble growth, chances of bubble interconnectedness increases and this drives coalescence. A closest packing of equally sized spheres takes up ≈74% of the total volume. In natural bubble-bearing melts an increase in connectivity occurs at ≈60% porosity. However, this threshold varies drastically according to bubble size and shape [e.g. 20]. Percolation theory may predict the connectivity of randomly dispersed pore space [e.g. 55, 94]; however, its application is non-trivial for magmatic foams as the range of bubble sizes and shapes is highly variable [31]. Shearing of the magma has an additional positive effect on the connectivity of the pore-volume (permeability) of magma [19, 118]. During slow decompression, the connectivity can allow outgassing and lower overall pressures leading to non-explosive outgassing [118]. During rapid decompression, the connectivity can aid fragmentation due to bubble wall thinning and cascading fragmentation through a network of bubbles [81]. Bubble coalescence occurs during bubble growth experiments described in Chapter 3, and is a crucial component of bubble collapse which I discuss in Chapters 3 and 4.

1.8 Outgassing and foam collapse

The porosity of magmatic foams decreases during coalescence of bubbles if outgassing occurs through a permeable network and the foam begins to collapse. Collapse of foamed magma is assumed to be mostly driven by either connection of bubbles and open-system degassing through a permeable network [104, 185], repressurization of the foam resulting in resorption of bubbles [180] or due to shearing of the foam [19, 118]. Sheared magma often produces bands of heterogeneities in crystal and bubble number densities and shapes broadly parallel to the flow direction [27, 62]. In a fully crystallized magma or lava, the direction of shearing is preserved in bands of different minerals and mineral orientations. It has been suggested that these textural features either cause a redistribution of water [27] or are the result of mingling of melts of different water contents [62, 154]. We present a new conceptual model of flow band formation in Chapter 4.

1.9 Crystallization

Magmas are typically far below the solidus temperature of crystal phases at the moment they erupt and, therefore, often contain crystals. Crystallization above the solidus is not the focus of this thesis, however, crystallization at or below solidus temperatures is an important component of Chapters 4 and 5. The high viscosity of the melt often prohibits nucleation and/or the growth of crystals, which leads to the formation of volcanic glass (as a rhyolitic glass called obsidian). At a high ΔT, i.e. at a high supercooling from the solidus, the viscosity is so high (and therefore diffusion is low), that heterogeneous nucleation dominates, which leads to a low crystal number density while growth of the crystals can still be rapid due to the high over saturation. This often leads to spherulitic growth of crystals (i.e. the radial growth of often branched needles which tend to form spheres). Spherulites are described in a variety of materials [144] and have been extensively studied ([e.g. 29, 30, 36, 57, 69, 100, 102, 106, 144, 146, 161, 181]). Spherulites are an ideal material for studies of crystal growth in magma because of their well-defined geometrical shape, as well as the unconvoluted chemical and textural data of their surroundings due to their sparseness and the homogeneous and isotropic nature of the melt in which they grow. Spherulites in volcanic rocks contain mostly anhydrous minerals and redistribute the incompatible water in diffusional haloes around the spherulites (see Fig. 1.5).

Studies that have modeled timescales of spherulite growth [29, 69, 181] suggested growth continues below the glass transition temperature (T_g); however, no conclusive evidence could be shown. In Chapter 5, I give a detailed summary of existing models of spherulite

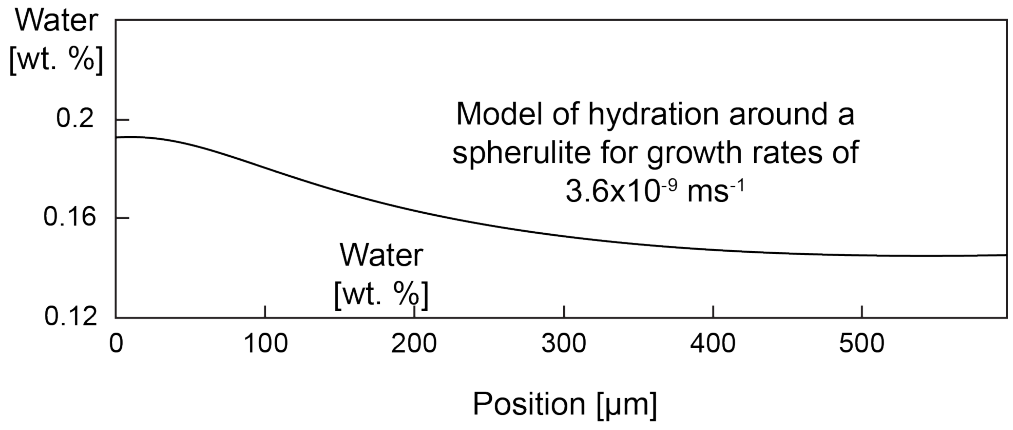

FIGURE 1.5: Hydration around a spherulite in a rhyolitic melt (position 0 μm marks the boundary of the spherulite). A numerical model yields a growth rate of the spherulite of 3.6x10^{-9} ms^{-1}. Modified from Castro et al. [29]

growth and discuss timescales and temperature of spherulite growth in the context of texture formation in a cooling lava dome based on analytical and numerical data.

1.10 Brittle deformation and fragmentation

When silicate melts are cooled below T_g, they behave as a brittle glass [183]. In the solid glass, kinetic processes are drastically slower, prohibiting bubble growth or collapse and slowing down or stalling crystal growth [155]. Continued exsolution and addition of volatiles or volatile expansion from decompression will exert stress on the walls of bubbles. Likewise, stress can be exerted by flow from magmatic pressure [87]. If this stress is rapidly applied (i.e. exsolution or flow rates are high), high strain rates shift the glass transition to higher temperatures as the time required for relaxation is exceeded by the rate of strain [43]. Therefore, cracks can form in an otherwise relaxed melt. A relaxed bubbly melt can be viewed as a gas suspension in a melt continuum, however, if cracks are pervasive and join up with gas bubbles/pores this creates a melt suspension in a gas continuum, fragmentation occurs and pyroclasts form [20, 22, 151]. If sufficient energy is contained in the expanding volatiles prior to fragmentation, these pyroclasts may be ejected in an explosive eruption. Alternatively, these fractures can heal again if eruption does not occur and temperatures remain high enough for relaxation[18, 79, 174]. At lower temperatures and with insufficient overpressure to generate an explosive eruption, cracks remain an open texture, decreasing the stability of volcanic domes or plugs and increase permeabilities [89]. An increase in permeability allows for more efficient degassing of a magma, effectively changing the eruptive behavior of the volcano to a more effusive eruption style [e.g. 75, 121]. Degassing through a fracture can be shown by gradients

of water across cracks in obsidian [18, 32]. An overview of different generations of cracks formed during the emplacement and cooling of a lava dome is given in Chapter 5, together with temperatures and timescales of first hydration of magma by magmatic and meteoric water.

1.11 Introduction summary

During ascent, eruption and emplacement of magma, bubbles form and collapse, crystals nucleate and grow and cracks open and heal. Questions relating to these processes are presented below in Table 1.1, and answering these questions is the aim of this thesis. During formation of these textures, important physical and chemical properties of the melt change which has a direct influence on the eruptive behavior of the volcano. Water heterogeneities are created during the formation of the textures and often remain as a record of eruptive processes. This study uses high-resolution water distribution mapping around textural features to support textural proxies of timescales and temperatures and conceptual models of texture development in magma. In Chapter 2, I will discuss FTIR preparation and analytical techniques used to achieve highest possible spatial resolutions to analyze textures in magma that form during ascent, eruption and emplacement at volcanoes.

Question	What could provide answers to this question?	
1. What technique is best suited for quantitative water analysis at high spatial resolution?	A comparison of recent developments in the analytics for geosciences.	Chapter 2
2. What is the best way to prepare fragile samples of vesicular, cracked and fragile glass?	Experience and trial and error of common techniques as well as exchange with other scientists.	
3. What are typical water distribution patterns around bubbles and can they be used as a proxy for volcanic processes?	High - resolution fourier transform infrared measurements around a number of vesicles in glass of a natural composition	Chapter 3
4. Is bubble resorption due to cooling possible and what is the impact on volume and water distribution of volcanic rocks?	Experiments of bubble growth with stagnation at a lower temperature and comparison of water profiles with quenched samples	
3. What are typical timescales of isobaric bubble growth and could this be measured in natural samples?	Volumetric measurements of bubble growth in combination with water diffusion profiles around the formed bubbles	
5. Are there water heterogeneities associated to flow bands?	High-resolution water measurements across a flow band with little or no vesicles and crystals that could distort the measurement.	Chapter 4
6. What are flow bands and how do they form?	Textural descriptions and comparison to vesicular volcanic rocks.	
7. Could flow banding be associated to the collapse of magmatic foams?	Measurements of water around bubbles that could have collapsed.	
8. At what temperatures do spherulites form and do they form below the glass transition?	Models of water diffusion profiles in combination with textural observations.Are there cracks preserved that were formed during the formation of the spherulite?	Chapter 5
9. How do Spherulites relate to other textures in volcanic domes in terms of temperature, timescales and formation processes?	Hydration patterns around textures that are associated to spherulitic growth, as well as textural relations that could give evidence of the order of formation during cooling.	
10. Have all cracks found in volcanic glass formed at the same time and temperature?	Comparison of hydration patterns around cracks that are connected to a source of water since formation.	
11. What are possible processes that lead to cracking in magma?	Textural relations and temperatures/timescales from diffusion modelling	
12. What are perlitic cracks, how do they form and at what temperature range and timescales.	Textural relations and temperatures/timescales from diffusion modelling, as well as hydration patterns: Was there hydration before the perlite formed, or is hydration a result of perlitic cracking?	

TABLE 1.1: Questions and aims of this study

Preamble

In the introduction of this thesis, I show that the volcanic textures that control volcanic processes are frequently microscopic. Microscopic structures include bubbles, crystals and cracks in the glassy groundmass of volcanic rocks. These textures are driven by microscopic temperature, pressure, and water saturation gradients. Therefore, the associated water heterogeneities are on a similar microscopic scale. Amplitudes of water heterogeneities can be miniscule, depending on the size of the textural feature itself. This leads to analytical challenges that made it impossible to detect and quantify these heterogeneities until recently. Modern techniques of synchrotron-sourced Fourier transform infrared spectroscopy (FTIR) allow for quantitative measurements of water at high resolution and signal to noise ratios. Focal plane array (FPA) detectors and high precision motorized microscopic stages in combination with better computers make it possible to collect thousands of spectra for images of water distribution within minutes. However, with higher resolution, sample preparation has to be more precise. When measuring volcanic glass with suspended textural features such as cracks and bubbles, the thin, double-polished wafers are even more fragile. When working with synchrotron radiation, beamtime is limited and sample preparation cannot be corrected if the thickness leads to oversaturation of the detector. Therefore, I developed and refined existing techniques to account for the fragility of textured samples. The following chapter gives an overview of the most important steps in sample preparation, execution of measurements and analysis of data for modern techniques in FTIR. The intention of this chapter is to share practical experience in order to encourage other users to employ these techniques successfully on volcanic glass and rocks that show textures and water heterogeneities.

Chapter 2

Advances in Fourier transform infrared spectroscopy of natural glasses: From sample preparation to data analysis

Fourier transform infrared spectroscopy (FTIR) is a common analytical technique utilized to measure volatile content in volcanic rocks. Water and CO_2 are the most common volatile species that drive volcanic eruptions. Water has a higher solubility at lower pressures and is therefore the main volatile forming bubbles during volcanic eruptions. Water concentration and distribution controls most magmatic processes and properties. FTIR has become one of the most widely used analytical methods for estimating water distributions in volcanic rocks. Additionally, quantitative measurements of different water species can be achieved at high spatial resolution. Basic FTIR equipment is comparatively inexpensive and requires minimal maintenance. Recent developments in core components of the analytical equipment such as synchrotron light sources or the development of focal plane array (FPA) detectors allow measurement at higher resolutions and the collection of concentration maps. Here practical insights from sample preparation to analyzing the distribution and speciation of water in volcanic rocks using FTIR spectroscopy are discussed. This chapter should encourage the usage of modern techniques in FTIR analyses for studies of volcanic rocks and discusses the main steps of this method to ensure best possible results.

2.1 Introduction

Volatiles are the driving force behind volcanic eruptions [147]. Dissolved volatiles drastically change the physical and chemical properties of silicate melts and magmatic rocks [68]. Therefore high spatial and quantitative resolution are essential for the understanding of magmatic processes from the subduction of crustal rocks to the emplacement of volcanic rocks [e.g. 20, 178, 179]. Specifically, the spatial distribution of volatiles in volcanic rocks are a record of diffusion and therefore a quantitative proxy for timescales and temperatures of hydration or dehydration mechanisms; such as the growth of bubbles [28, 79, 180](Chapter 3), hydration of archeological artefacts [153], or the formation of crystals [29] (Chapter 5). Analysis of melt inclusions is the main tool to understanding initial volatile contents of melts and to estimate the depth of magma crystalization [e.g. 178]. Volatile contents of glass inclusions and groundmass volcanic glass host records of diffusional changes in volatile concentrations over time, temperature and pressure and are therefore of utter importance for establishing models of fundamental processes from the lithosphere to volcanoes and volcanic eruptions.

Numerous studies discuss a variety of analytical tools for the measurement of volatiles in volcanic rocks [e.g. 33, 39, 76]. Routes of volatile analysis include: Fourier transform infrared spectroscopy (FTIR; here discussed) [11, 113, 159, 160], secondary ion mass spectrometry (SIMS) [37, 65–67, 178], Raman spectroscopy [13], analysis of the Loss-on-Ignition (LOI) by Karl Fischer titration [175, 184] and/or thermo gravitational analysis (TGA) [3, 38], as well as electron backscatter methods [73, 101]. Apart from availability, funding and other personal considerations such as experience of the user, there are specific strengths and drawbacks of each analytical method.

Fourier transform infrared spectroscopy, the focus of this article, measures the fundamental vibration and the associated overtones in the infrared region of the electromagnetic spectrum. FTIR instrumentation is comparatively simple (unless a synchrotron source is used) and it can deliver accurate and precise measurements of high spatial and quantitative resolution [e.g. 39, 76, 112, 159, 160, 195]. Specifically, a spatial resolution of up to 3 μm under synchrotron light sources and up to 20μm under conventional light sources and detectors can be achieved [103]. Depending on the absorption bands investigated, the detection limit can be as low as 0.001 wt.% of either: hydroxyl groups, molecular water or total water. Discriminating different bonds in hydrous compounds is one of the major strengths of FTIR analysis and allows the quantification of hydrous species to determine equilibration timescales [198]. Perhaps the major drawback of this method is related to sample preparation, which, in most cases requires doubly polished, thin, unsupported wafers. More importantly, sample preparation can be the primary

accuracy limitation as the measured values are directly proportional to the thickness and water content of the sample.

Secondary ion mass spectrometry uses an ion gun to emit secondary ions from the surface of the analyzed material, which are then collected by a mass analyzer. Samples only need to be polished on one side. Both the spatial resolution and detection range can be extremely high at micrometer scale with detection limits down to parts per million [33, 65, 67]. Accurate quantitative measurements require careful calibrations (often done in reference to FTIR data) and the matrix effects of natural glasses can be complicated, requiring standards of similar chemical compositions. A major limitation of this method is that the characterization of water speciation is not possible [67, 76].

Raman spectroscopy is based on molecular vibrations caused by the scattering of light [76]. The use of a coherent light source (i.e., a laser) allows for higher spatial resolution than conventional FTIR, however, calibrations for quantitative measurements are limited, but are constantly being developed and refined [e.g. 13, 41, 93]. Before Raman spectroscopic measurements can be used as a reliable quantitative method, combined studies with FTIR are necessary to provide a reliable calibration, where doubly polished samples are hard to prepare.

A way of determining bulk water concentrations without the use of spectroscopic methods is to force complete degassing by heating the samples to high temperatures in a furnace or by using laser ablation. The released gas can then be detected by quantitative methods with low detection limits (60 ppm for 1 g of sample [184]) via Karl Fischer titration [e.g. 175, 184] or by measuring the difference in weight coupled with qualitative measurements by quadrupole mass spectrometry [38]. The advantages of this method are that it is inexpensive, it measures the bulk volatile contents of larger masses of rocks, and that the degassing temperatures potentially contain information about volatile species degassing patterns [3, 171]. However, the processes of degassing at high temperatures are not fully understood, neither are the impacts of sample preparation. Further disadvantages are that this method also measures adsorbed volatiles, the contents of fluid inclusions and minerals, in addition to the volatiles dissolved in the glass and the method is destructive. A potential future advantage of the development of this technique includes the ability to target and measure particular dehydration events at specific temperatures [3, 171].

Backscattering of atoms at the surface in nuclear microprobes used in elastic recoil detection (ERD) or Rutherford backscattering (RBS) can produce accurate and precise measurements of hydrogen contents in volcanic glass. For example, the study of Bureau et al. [16] gives a limit of 4x16 μm^2 as a maximum spatial resolution and 94 wt. ppm as a detection limit. Recent studies show promising results in the use of backscatter electron

analysis for measuring water concentrations in volcanic glass [73, 101] but matrix effects and the impact of the polishing quality are not fully understood, therefore, analyses have to be treated as qualitative.

A number of analytical methods are suited for analysis of volatiles in volcanic rocks, however, funding and availability limit the choice significantly. FTIR is widely available, is a well-documented method and is therefore preferred by many scientists. The list of methods, however, is constantly growing, which makes it important to review the choice of analytical method regularly, based on recent developments in literature and technology. Comparatively, the increasing possibilities for volatile analysis and the increasing body of literature available on analytical FTIR techniques make this an ideal method for many applications when measuring volatile contents of volcanic glass. In the following sections, we provide an overview of recent techniques and developments in FTIR and share our practical experience in sample preparation, measurement and analysis of the resultant data.

2.2 Fourier transform infrared spectroscopy

The vibrations of bonds in volatile species are usually elucidated by the absorption of light in the region of near- and mid-IR (at wavelengths of $\approx$1.257 μm, which corresponds to wavenumbers of 1400-8000 cm^{-1}). The vibrations within the volatile species can either be bending or stretching in two (e.g. for OH^- and H_2O) or three dimensions (for CO_3^{2-}) resulting in several peaks in absorbance.

In addition, the vibrations have overtones at higher wavenumbers in the near-IR region (see Fig. 2.1 for a typical spectrum). The peaks caused by overtones are usually smaller (at constant volatile concentrations and thickness; see Fig. 2.3 for comparison) and typically less convoluted than the vibrational absorption peaks in the mid-IR region (see Fig. 2.1), making them the preferred bands for measurements of quantities of species at high volatile contents ($\gtrsim$1 wt.%) where absorbtion can be detected in reasonably thick samples. At low volatile contents ($\lesssim$1 wt.%), however, these peaks are too small to be detected in translucent samples (see Fig. 2.3). In FTIR, all wavelengths of the spectral area are created by a Michelson interferometer and the produced interferogram is transformed into a spectrum by a Fourier transformation. In a Michelson interferometer, the incoming beam of light passes through a half translucent mirror (i.e. the beam splitter) and interferes with the incoming beam while the additional beam path oscillates. This creates an interference pattern of the wavelengths of interest within a short period of time. In contrast to a prism, the light does not have to pass through a small slit and, therefore, the intensity of passing light remains high. Further, one interferogram

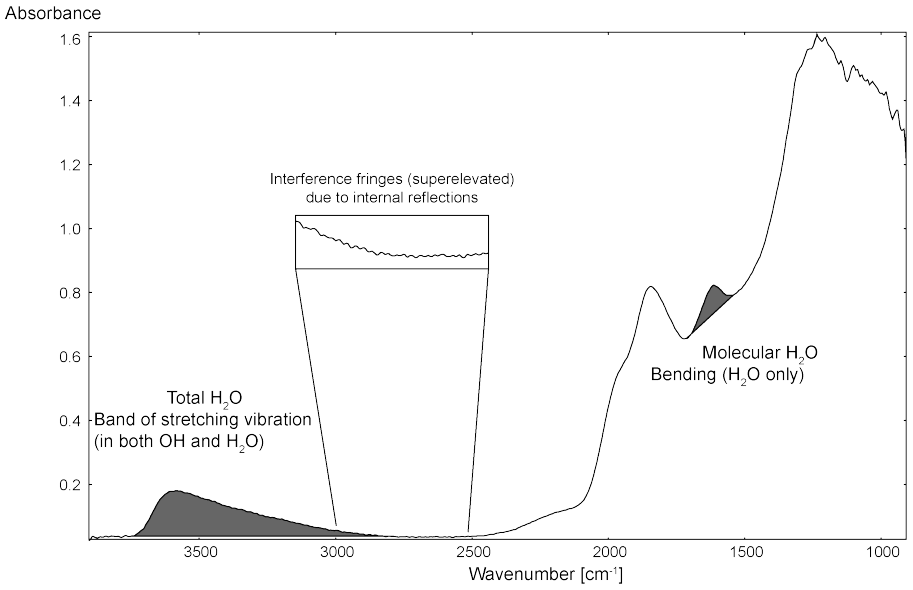

FIGURE 2.1: Spectrum of volcanic glass with low water contents (<0.2 wt.%) in the mid- IR region. Note the different shapes of the peaks for total water and molecular water. While measuring the peak height for the 3570 cm^{-1} peak limits the influence of correct positioning of the baseline, the peak at 1615 cm^{-1} would change drastically with small differences in the angle of the baseline. Therefore speciation measurements are often not possible because of difficulties in setting the baseline correctly while maintaining consistency in the measurement method.

contains the whole spectral data and a set of tens of scans through the whole spectrum (e.g. 1000 cm^{-1}–6000 cm^{-1} can be performed in seconds to minutes) and the absorbance of all relevant species can be measured concurrently.

2.3 Near IR versus mid IR

In most cases, the amount of water in the sample dictates the choice of bands for analyses (see Fig. 2.3). Sample thicknesses have to be prepared accordingly to ensure high signal to noise ratios. As discussed earlier, high resolution imaging of water using near-IR bands is not possible at low volatile concentrations that require thick wafers if small textural features create water heterogeneities within the thickness of the sample (see Fig. 2.2).

Thin samples that could produce interference fringes within the spectra can make analysis of the measurements difficult. This is especially the case for the spectral range of 2500 $\pm$ 500 cm^{-1} and makes the selection of an appropriate baseline difficult. If an aperture is used (i.e. in any method with conventional detectors), the diffraction limit

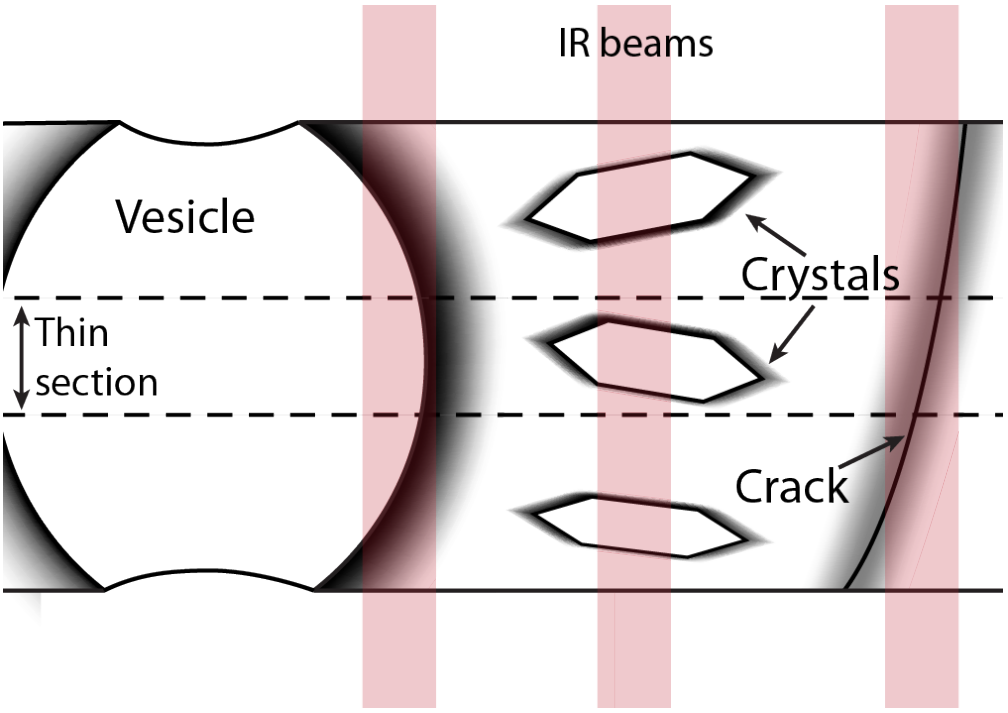

FIGURE 2.2: Thickness issues when performing FTIR analyses on textured volcanic glass. The chances of artefacts due to geometrical effects and/or hidden objects is higher when measuring through a thick section rather than a thin section.

of the measurements becomes apparent at wavenumbers $\lesssim$2000 cm^{-1} [103]. If an FPA detector is used, higher spatial resolutions are not limited by the diffraction of long wavelengths [103]. FPA detectors, however, are mostly available for the mid-IR region, and often synchrotron sources are set up for mid-IR measurements because of a wider user base.

2.4 Preparing your sample for optimal results

Sample preparation is the most time-consuming and important step in assuring successful measurements using transmitted light FTIR. A doubly polished wafer of the sample has to be prepared. This is usually done by cutting the sample, polishing it on one side and fixing it to a slide or similar, so the other side can be polished down to the final thickness. Before starting the actual preparation the choice of the thickness of the final wafer and an appropriate adhesive for mounting has to be selected.

To estimate the ideal thickness a volatile content has to be predicted and the absorption has to be calculated from that. The best result for measurements are achieved at absorptions between 0.2-0.7 [139], but even at absorptions up to 1 the noise levels are acceptable. Figure 2.3 shows curves for the most common cases of rhyolitic glasses and

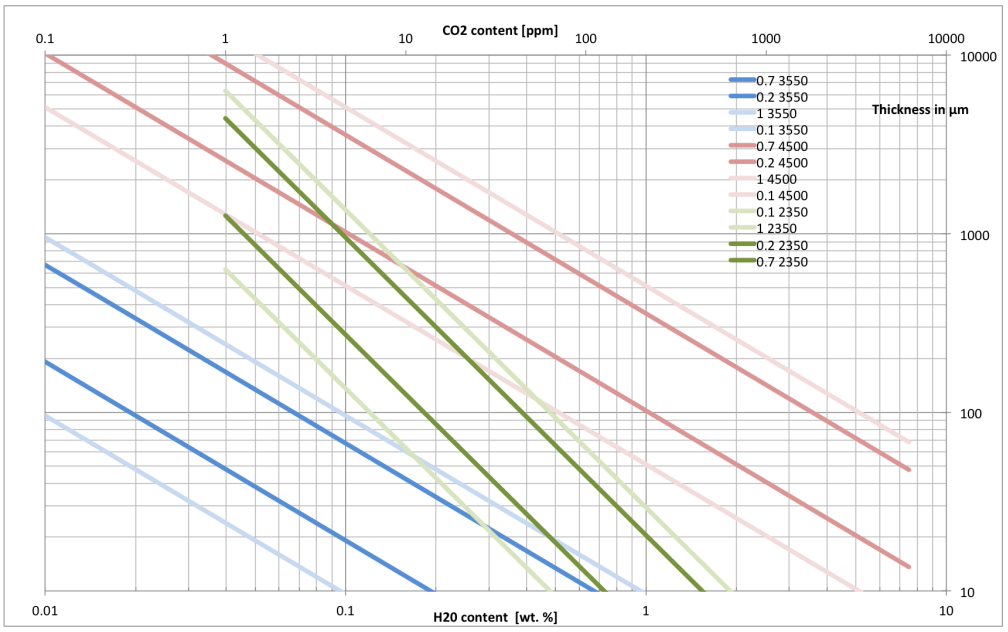

FIGURE 2.3: Thickness estimations to consider before sample preparation; This is a rough estimate of ideal absorptivities for rhyolitic samples at different volatile concentrations and thicknesses. Blue: water in Mid-IR, green: CO_2 in mid IR, red: water in Near IR. The limits can be varied, depending on experimental setup. However, at the values between 0.2-0.7, signal to noise ratios are the highest [139]. Absorptivities for more mafic materials is slightly different, however, opacity of the sample may be an issue when measuring samples of high iron contents. Therefore, these numbers should only be considered as a rough guideline.

can be used as a quick reference to calculate the necessary wafer thickness. These thicknesses should only be seen as approximate values and different values might be more appropriate for the objective for different reasons:

- If the sample shows opacity (e.g. mafic compositions), the sample has to be thinner to achieve a sufficiently strong signal. Absorption coefficients for rhyolitic compositions in Fig. 2.3 only differ slightly from basaltic absorption (see Table 2.1, therefore, this can be used as a rough guide for basalts as long as the sample is not too dark.

- If the sample contains crystals, cracks or vesicles, the sample has to be thin to avoid hidden features within the thickness of the wafer. See Fig. 2.2.

- Geometrical effects can distort concentration patterns and can only be minimized by preparing thinner samples and choosing locations where the distribution can be assumed to be homogeneous throughout the thickness of the sample, for example, sufficiently far from textural features of interest. See Fig. 2.2.

Conversely, thin samples are problematic in two ways:

- Thin samples are difficult to handle and prepare. They easily break or blow away.
- The accuracy of thin samples largely depends on the accuracy of thickness measurements. A nominally small error in thickness measurements can lead to large relative errors in composition quantification. If a sample measures 15 μm in thickness, and the thickness evaluation gives and error of ± 2 μm, the overall error is larger than 25%, however, at a thickness of 150 μm the error is lowered by an order of magnitude.

Therefore, properties of each individual sample have to be considered when targeting thicknesses during preparation. A homogeneous sample should always be as thick as possible to ensure good signal-to-noise ratios, heterogeneous samples and samples with unknown water contents should be polished to thinner wafers to keep the spatial resolution high and to avoid oversaturation of the detector. If in doubt, keeping the wafers thinner rather than thicker is the preferable option. Samples that need to be doubly polished should be mounted on a slide. For stable samples the first side can be polished without support, however, if samples are very fragile, vesicular or already fractured, they have to be impregnated with a bonding agent before the first polishing. Similarly, very small samples, such as crystals containing glass inclusions, have to be mounted using a resin or glue. Several different adhesives are commonly used and each of them has specific properties that have to be considered before using them.

- Crystalbond^{TM} 509 is an adhesive that can be melted onto the sample at $\approx$100 °C and removed with acetone. Crystalbond^{TM} is a good choice for both adhesive and impregnation purposes as long as the samples are small. Handling is particularly easy and the mounted sample can be adjusted at any time. Further advantages are fast setting and excellent solubility in acetone. Polishing should be done manually to avoid softening of the Crystalbond^{TM} due to heat production during preparation.
- Superglue (ethyl-2-cyanoacrylate) has a very defined chemical composition, is a strong adhesive and binds quickly at room temperature. It can be removed with acetone and residues can be easily spotted as a white film or fibrous material under the microscope. Superglue is stronger than Crystalbond^{TM} if used in small volumes, which may prevent low surface area samples from flaking from the slide during polishing. Removing the glue takes longer than for Crystalbond^{TM}, and the short hardening time can make handling challenging. Thinning the superglue with acetone is a good way of extending the working time, although it can produce bubbles in the set glue, which lower the stability during cutting and polishing.

- Epoxy resins such as Araldite® or Epo-thin™ offer highest stability as an adhesive and fill sample voids. However, epoxy cannot be removed and care has to be taken that it does not interfere with the measurements. To avoid alteration of the signal, mapping peak heights at a previously determined peak position that is characteristic for the applied epoxy can be used to ensure that the measured area is epoxy free. Epoxy resin is less brittle, easier to handle because it takes longer to set, but it cannot be removed and the spectra can be contaminated. However, it is easy to detect in the measured spectra and can be excluded from the data (Fig. 2.4).

  For small samples and very porous samples that need large volumes to be filled, Crystalbond™ works really well and is easy to handle, but it must be insured that the short periods of heating will not alter the samples.

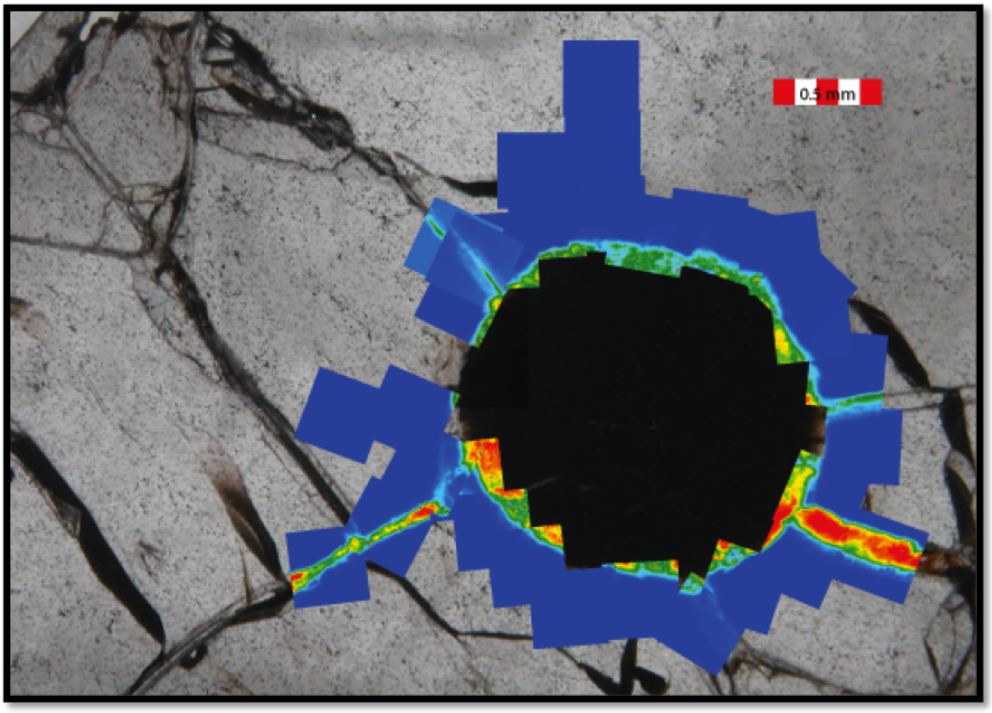

FIGURE 2.4: Distribution of epoxy resin in a cracked glass around a spherulite (See Chapter 5) measured at 2973 cm^{-1}. The confined distribution helps to identify cracks and to dismiss data that could be affected by absorption of the resin. Warm colors show elevated absorptions.

Small samples should be entirely covered with glue to make sure that the sides also remain embedded and enough surface area exists to effectively parallel polish the samples. Embedding polishing aids of similar hardness, such as little pieces of colored glass or garnets at a distance from the sample, can help keep a parallel polish by adding resistance to the otherwise comparatively soft adhesive.

If the samples have similar refractive indices as the adhesive, coloring of the sample with an acetone-soluble pen can make it easier to check the progress of the work.

The samples have to be polished to microscopically smooth surfaces. For this, it is best to polish with decreasing grit sizes down to at least 1 μm; however, the best results are achieved with a grit size of 0.25 μmm. The actual choice of material and grits depends on individual preferences and on properties of the samples, but a reliable choice is (in ISO/FEPA grit) P800 – P1200 – P1500 – P2000 as wet silicon carbide papers. At P2000 the average particle diameter is 10.3 μm. Lower grain sizes are best polished under rolling grain. If the measured area contains cracks, bubbles, crystals or the sample is very small ($\lesssim$3 mm, depending on the skills and equipment of the operator), care has to be taken not to polish shoulders into grain boundaries. These can be avoided by using ceramic polishing dishes instead of felt polishing covers where possible, and minimizing overall polishing times. If the sample is very brittle or contains crystals or other objects that could break loose, felt is a better choice to avoid scratches. In any case, ample sample lubrication should be provided at all times. As lubricants, water can be used and for finer grit polishing, lubricants containing propylene glycol (available as common antifreeze for combustion engines) or similar are suitable choices.

2.5 New Analytical capabilities

One of the most significant advances in FTIR measurements for the analysis of volcanic glasses is the automation of 2-dimensional distribution measurements at a very high signal to noise ratio and spatial resolution near- or at the diffraction limit. Two of these techniques are the measurements with focal plane array (FPA) detectors and the employment of synchrotron light sources combined with high precision motorized microscopy stages.

2.5.1 Focal Plane Array Detectors

Since the development of multiple channel detectors in the 1970's, this technology has improved drastically, allowing high resolution imaging μFTIR at high rates with globar light sources. All individual detector elements on the focal plane array simultaneously measure the absorbance of the spectral range of the system. This makes it possible to create maps of absorbances over large areas in very short timescales. The simultaneous measurements of wide areas of often hundreds of μm^2 occur within minutes compared to hours on a conventional FTIR. This makes FPA detectors ideal for mapping of large areas or reconnaissance measurements. However, the signal to noise ratios are lower

than that of synchrotron sourced FTIR due to the weaker light source, which can make quantitative measurements of small signals difficult. The spatial resolution is not only limited by the pixel size but also by signals off the focal plane as FPA measurements are not confocal. Signal to noise ratios can be significantly increased by pixel binning if spatial resolution is no concern. Unfortunately, these detectors are not being used in combination with synchrotron radiation due to limitations of the optical setup.

2.5.2 Synchrotron IR sources

Synchrotron radiation is widely available and the use for FTIR opens new possibilities for the analysis of volcanic glass. Synchrotron sources produce much brighter light than conventional globar sources. This keeps signal to noise ratios high, even at small apertures. The light is not only very powerful, it is also emitted in a small range of angles and, therefore, less light is blocked by the aperture. Miller and Smith [103] show that at an opening of 10 μm, more than 80% of the radiation of a globar source is blocked by the aperture, compared to less than 20% of a synchrotron light source. The spatial resolution is limited by diffraction, which becomes apparent at an aperture of 5x5 μm below 2000 cm^{-1} Miller and Smith [103]. At maximum resolutions, the slightly heterogeneous intensity of synchrotron light sources can become apparent, when the overlapping apertures during continuous measurements on a motorized stage are not compensating this effect. Therefore, baselines for the band of molecular water at 1630 cm^{-1} can be hard to determine at high spatial resolution. If compared to FPA detectors with a globar source, signal to noise ratios are much better and spatial resolution is only limited by diffraction.

2.5.3 Data volumes in imaging FTIR

Due to the vast amount of data created during measurements of arrays of points, the wavenumber resolution should be kept at a minimum and the number of scans should be appropriate for the overall resolution of the measurements. In most cases a resolution of 4 cm^{-1} or even 8 cm^{-1} is sufficient, if the signal is at a reasonably high level. The number of scans can be estimated in test runs, but for most applications, 64 or even 32 scans are adequate to keep measurement times at a minimum without compromising the quality of the data. Apodization, which is the method of cutting off the lobes of the interferogram, can lower the spectral resolution, but prevents wiggles on the lobes of absorption bands. Generally, a stable base is very important for consistent placement of baselines, and especially in the wide peaks in the range of 3500 cm^{-1}, a high spectral resolution is not the highest priority. Therefore, a stronger apodization (the way the interferogram is

limited in order to allow fourier transformation) rather than just a boxcar apodization (a rectangular cut off) should be used, such as a three-term Blackman-Harris window.

2.6 Data analysis for volatile concentration mapping in volcanic glass

Based on Beer's law, volatile contents can be determined by dividing the product of molar mass (M) of either CO_2 (44.01 g mol^{-1}) or H_2O (18.02 g mol^{-1}) and the absorbance as the peak height or integral after subtraction of the background (A) by the product of thickness (d), density (ρ) and an empirical value, the extinction coefficient (ϵ) [160].

$$c = \frac{M \cdot A}{d \cdot \rho \cdot \epsilon} \tag{2.1}$$

This is the same for imaging analysis except that it has to be decided whether these values can be assumed for a range of different measurements. Slight peak shifts and different baseline levels can introduce systematic errors. At the same time measurements should be kept as simple as possible to ensure that the results are reproducible. In most cases, the absorption is measured as the peak height, which does not mean that this method gives more reliable data. Especially at lower signal to noise ratios, the placement of a baseline can be difficult. However, most literature only presents extinction coefficients for peak height estimations. The baselines for the water-bands in the mid-IR range are commonly linear.

2.6.1 Parameters for quantitative FTIR analyses

Thickness measurements are a major concern for thin samples as this can possibly introduce large errors. The most common methods are:

- Measurement by interference fringes [190]: By counting the fringes that are produced by interference of the primary source of light and the light of internal reflections in the sample, the thickness can be accurately determined at a precision of up to ± 3 μm. The method is non-destructive and can sometimes be completed in the same measurement with transmitted light. However, this can only be done if the samples are well polished or when using the reflective mode with a gold plate in order to ensure higher signal to noise ratios at the fringes. The number of fringes is counted in the area between 2000–2700 cm^{-1} and the thickness can be

determined with the following relationship:

$$d = \frac{m}{2n(\nu 1 - \nu 2)} \tag{2.2}$$

where m is the number of waves in a selected wavenumber range, n is the refractive index of the sample and $\nu 1$ and $\nu 2$ are the highest and lowest wave numbers over the selected interval [190]. The biggest contribution to the error in the thickness estimations by interference is caused by the estimation of the refractive index [113]. This method can be successfully used for glassy, well polished samples of about 5–250 μm thickness, however, precision is higher for measurements of samples $\lesssim$100 μm [177](See Chapter 5).

- Micrometer or digital displacement gauges are probably the most common thickness measurements, with a maximum accuracy of $\pm$2-3 μm. The main issue is that the pointy tip of the micrometer can break the sample. If the sample is very porous, the tip can sink into the sample, damaging it and thus making the measurement is impossible. The measurement is also not confined to a small spot and not matching the position of the measurements. Nevertheless, for thick samples, this is the most reliable and quickest method and should also be performed as a reference measurement on samples that have already been measured with other methods.

- Calibrated stages of microscopes can make very precise measurements of samples of almost any thickness by measuring the vertical displacement between the focused surfaces of the wafer. However, calibrations should be performed regularly to eliminate drift.

Other parameters that are needed for quantitative analyses of volatile contents are densities and extinction coefficients.

- Densities can be estimated for individual measurement points using published data [83, 84, 116] or measured with Archimedes method for a bulk density. Densities mostly depend on individual sample compositions and are especially drastic for samples with large variations in water content. In these cases forward modeling of densities is important. However, qualitative results are not influenced by the assumption of constant densities and may be appropriate for low water contents and small changes within the sample.

- Values for the extinction coefficient (ϵ) exist for a range of compositions and it is up to the reader to decide which one to choose (See Table 2.1). Since the review article about volatile analysis in magma by Ihinger et al. [76], a broader range of

chemistries have been covered by reference measurements with a variety of analytical methods. Estimating extinction coefficients from equilibrated volatile species as reviewed by [33] should not be used for natural samples, as an equilibration of species cannot be guaranteed and species equilibrium constants are only known for certain ranges of temperatures [194]. We encourage the reader to either calibrate for accurate values of ϵ by employing other methods of analysis or to chose ϵ by the best fit of the composition of the sample.

Volatile Species	**OH**	**H_2O**	**H_2O**	**OH**	**OH**	**H_2O**	**OH**	**H_2O**	**H_2O**	**CO_2**	**CO_3^{2-}**	**CO_3^{2-}**	
Wavenumber [cm^{-1}]	*7100*	*7100*	*5200*	*4500*	*4000*	*4000*	*3550*	*3550*	*1630*	*2350*	*1500-1700*	*1350-1430*	
Stolper 1982	21	0.21	1.76	0.98	0.95	0.95	67	67					basalt
Newman 1986	0.32	0.184	1.61	1.73	1.14	1.07	100	56	55				rhyolite
±	0.008	0.012	0.05	0.02			2	4	2				
Integrated	96	83	248	341	290	350	44000	26300	2640				
±			24	25			1000	2200	200				
Dixon 1988							63	63					basalt
±							5	5					
Dobson 1989	0.26						88						rhyolite
±	0.01						2						
Ihinger & Stolper 1994			1.86	1.5			80						rhyolite
±			0.05	0.05			4						
Dixon 1995			0.62	0.67					25				basalt
			0.07	0.03					3				
Cocheo 1994			0.56	0.58									basanite
±			0.04	0.02									
Fine & Stolper 1985										945	200	235	SiO_2-$NaAlSiO_2$ glasses
±										45	15	20	
integrated										25200	24100	16800	
±										1200	1900	1500	
Fine and Stolper 1985											375	375	basalt; Ca-Mg silicates
±											20	20	Only for CO_2 <0.8 wt. %
Stolper et al. 1987											199	235	albite
±											17	20	
integrated											27300	16300	
±											2300	1400	
Thibault & Holloway 1994											355		leucitite
Behrens 2004										1214			rhyolite
±										78			
Okumura 2005				1.42	1.75								rhyolite
±				0.12	0.08								
integrated				285	239								
±				24	11								

TABLE 2.1: Overview of available extinction coefficients (ϵ), modified and updated from Ihinger et al. [76]. Sources: Behrens et al. [12], Cocheo [34], Dixon et al. [45], Dobson et al. [46, 46], Fine and Stolper [50], Ihinger et al. [76], Newman et al. [112], Okumura [117], Stolper et al. [158], Stolper [160], Thibault and Holloway [165]

2.6.2 Measurement of maps and ways to display results

In samples that are heavily textured and show complicated water distribution patterns care has to be taken to choose the measurement distribution. To ensure significance of the data, spot measurements or even a profile of the volatile distribution is often

not sufficient and the 2-dimensional distribution has to be measured. Hidden textures or chemical heterogeneities can be identified by measuring the surrounding of the area of interest (Fig. 2.2). This can either be done by using FPA detectors or by a grid measurement on a motorized stage. However, contour maps of the distribution are often misleading and imply a higher resolution than actually measured. A grid of spots, however, is a simple way of showing the actual number of measurements while showing enough of the photomicrograph of the sample (Fig. 2.5).

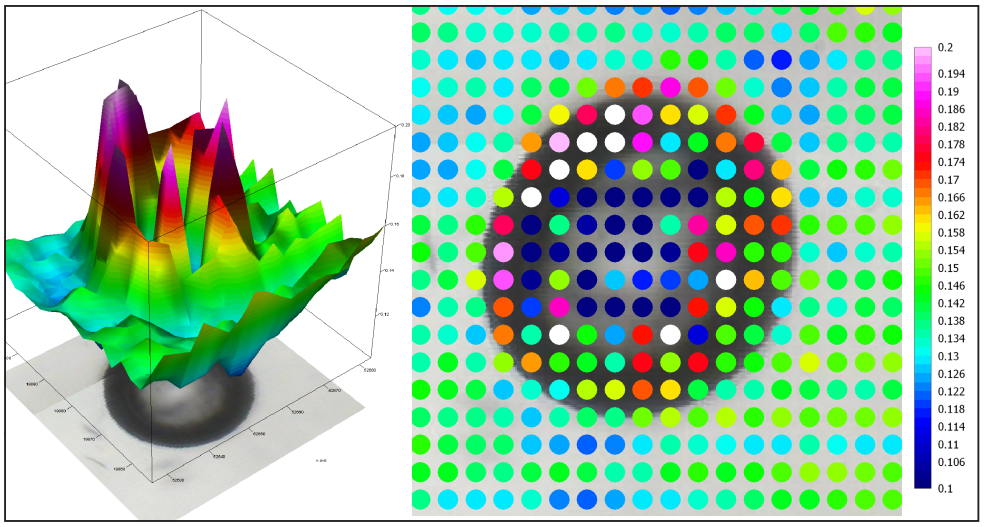

FIGURE 2.5: Two ways of showing the same data of the integration of the total water band around a small bubble in volcanic glass. Showing spots instead of a 3D graphic reveals that the sharp increases are in fact just artefacts inside the bubble rather than increases of water around this particular bubble. Warm colors indicate high absorbtivities of of total water. The bubble measures ≈30 μm in diameter.

2.7 Conclusions

FTIR is a potent method for analyzing volatiles in volcanic rocks. New possibilities of increased spatial resolution and faster processing of arrays of data present the opportunity for maps of volatile concentrations at a spatial resolution that is close to the limit of diffraction. However, sample preparation and the choice of measurement parameters are still in the hands of the operator. In order to encourage the community of geosciences to use modern techniques in FTIR, we present advice for sample preparation, measurement and data analysis for new techniques such as synchrotron sourced FTIR and FPA detectors in FTIR.

Preamble

The preceeding chapter outlined the most up to date techniques for analyzing microscopic changes in water content and mapping these changes in a meaningful way. Maps and gradients produced by these techniques allow inferences to be made about the formation of volcanic textures which are crucial to understanding why volcanoes erupt. The formation of bubbles marks the onset of volcanic eruptions. Water gradients around bubbles can be used to deduce the timescales of magmatic processes such as magma ascent, eruption and emplacement of individual samples. Better constraints on these processes is essential for monitoring and evaluating the past and current eruptive patterns of a volcano, i.e. whether periods of magma stagnation, dome growth, or sub-surface degassing existed or whether magma was erupted during initial ascent and exsolution of volatiles. While the growth of bubbles due to depressurization accounts for most of the volume increase, important information about the thermal and temporal history of individual bubbles may be reconstructed by modelling diffusion profiles around bubbles. In this chapter, I present water distribution patterns around bubbles in experimental samples of foaming magma. I discuss possible scenarios for the formation of clearly and qualitatively distinguishable patterns of water heterogeneities for a universal classification of ascent and cooling processes. This chapter is going to be submitted to the Journal "Earth and Planetary Science Letters" to be considered for publication.

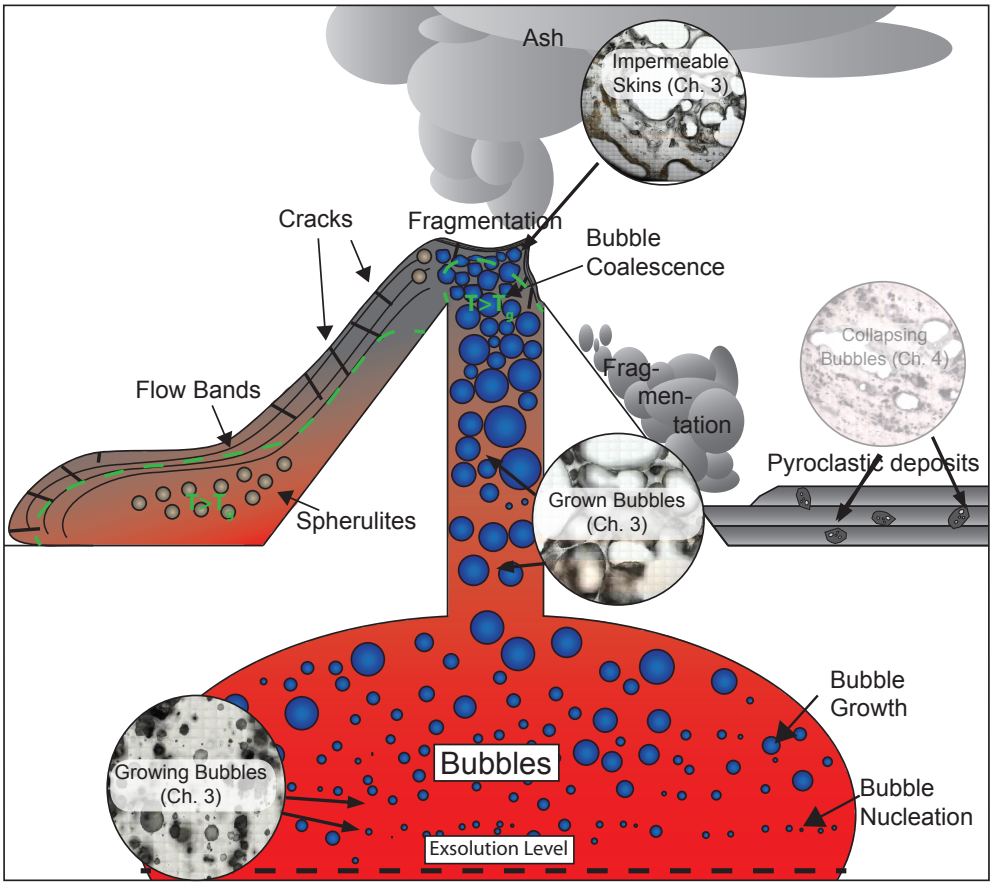

FIGURE 2.6: Overview of textures in Chapter 3

Chapter 3

Water diffusion during bubble growth in magma

Water diffuses into and out of bubbles in magma controlling the eruption style of a volcano. Evidence of this is recorded in water concentration profiles frozen around vesicles in volcanic glass. Previous to this study, these diffusion-driven profiles were analyzed in natural samples; however, they have never been systematically experimentally characterized. Here, we present the first high-resolution water distribution analyses during experimental bubble growth and cooling. At isobaric bubble growth conditions, we produce negative, positive and flat water gradients in glass towards vesicle walls. We heat cores of bubble-free rhyolite with ≈0.13 wt.% H_2O to 950 °C under isobaric conditions. These samples foam to produce an initial volume increase of up to 450% followed by a loss of ≈10% of the maximum volume. During bubble growth, negative gradients of water content form towards bubble surfaces until bubbles sizes maximize and water homogenizes. Upon cooling, water increases towards bubble surfaces related to resorption and the retrograde solubility of water in melt. Our experimental results can be used to imply distinct stages of bubble growth during magma stagnation, either on the conduit wall, in a lava dome or as an erupted pyroclast.

3.1 Introduction

Bubble growth forces magma to rise in volcanic conduits, produces overpressure within the conduit and leads to fragmentation of the melt during explosive eruptions. The foaming magma rises [147] and is fragmented in explosive eruptions [151]. Explosive eruptions

often evolve into effusive eruptions and vice versa; producing slowly cooling lava domes [e.g. 121, 186]. Numerous studies associate changes in porosity and permeability with the transition of explosive to effusive eruption styles [e.g. 75, 81, 185]. Degassing of magmatic foams during collapse is primarily controlled by gas release through a permeable network after bubble coalescence [17, 81] and shearing [19, 118]. This suggests an open system degassing of highly vesicular magma, supported by hydrogen isotopic records [1]. The reduced permeability of conduits plugged by volcanic domes can lead to large explosive eruptions or the dome itself can collapse producing block and ash flows [e.g. 35]. The timescales and microscopic texture changes during these phases of eruptions, however, are poorly constrained. Timescales of foaming, ascent, fragmentation and emplacement can be as short as 4h [25]. But at the same time, recycling of material in eruptive pulses [180], and secondary heating and/or hydration [18, 177] (Chapter: 5), can affect these timescales. Textural observations, zoning profiles in crystals, and phase equilibria experiments have been used successfully to constrain spatial and temporal proxies of volcanic rocks [e.g. 18, 28, 32, 177]. Within the short timescales of some eruptive processes, a linear depressurization and cooling history proves to be inappropriate.

3.1.1 Bubble growth

Bubble formation and growth can be divided into different phases during magma ascent. When oversaturation of a volatile species is reached bubbles nucleate heterogeneously and preferentially on existing surfaces, such as microlites [74], or homogenously at higher levels of supersaturation [e.g. 98, 107]. The growth of the bubble is controlled by (1) diffusion of water into the bubble [e.g. 126, 147] and (2) inflation due to depressurization [95, 125, 166, 170]. Several studies describe or model the volume change of bubbles in magma at different conditions: isobaric [70, 126], during decompression [56, 95, 125, 166, 170] and under re-pressurization [180, 185]. Studies have attempted to reproduce bubble growth in experiments [e.g. 7–10, 14, 56, 61, 86, 95, 97, 170, 193]. Heterogeneous and homogeneous bubble nucleation, and bubble growth in closed and open environments at various decompression rates and temperatures are explored [56, 92, 95, 111]. Most of these studies concentrate on determining valid forward models for bubble growth during decompression. After nucleation, the internal pressure in the small bubbles needs to be high to resist the high surface tension of the melt [6, 98], keeping growth rates low. As the surface/volume ratio increases with bubble growth, the relative effect of surface tension is reduced, and bubbles grow more rapidly with more surface area becoming available for diffusion. Proussevitch et al. [126] model a drastic increase in the bubble growth rate at this point, and an accompanying steep negative gradient of H_2O toward the bubble

surface. A measurable depletion of water in melt surrounding bubbles has been shown in natural samples [28]. Proussevitch et al. [126] also predict that the length-scale of the decrease in water will increase until it interacts with the decreased water contents of surrounding bubbles. The overall water content equilibrates to the respective solubility at given pressures and temperatures over timescales proportional to the melt viscosity, and the magnitude of the gradient produced [126].

3.1.2 Bubble resorption

Gardner et al. [56] show that successive re-pressurization would allow for bubble resorption, eventually obliterating textural evidence of the bubbles. Increases and decreases in water contents are also shown in depressurization experiments of CO_2- and H_2O-bearing bubbles [193]. However, the resorption of water is attributed to effects of solubility changes during re-equilibration with the CO_2-rich atmosphere in these experiments. McIntosh et al. [101] shows that even fast quenching can produce resorption rims in isobaric experiments. The study of Watkins et al. [180] shows increases of water toward bubbles in pyroclastic obsidian, interpreted to be the result of pressure changes in the melt. Cyclic pressure changes were confirmed by the occurrence of haloes of small vesicles around large vesicles and the heterogeneous CO_2 distribution indicated disequilibrium conditions at greater depth and high temperatures. The obsidian chips of Watkins et al. [180] are described as a rare case of preservation of evidence for degassing because the low permeability of the obsidian chips protected them from secondary hydration with meteoric water. Most natural pyroclasts from explosive eruptions are highly permeable pumices with thin bubble walls that are notoriously hard to prepare for water analysis and easily affected by post eruption secondary hydration by rainwater [52–54, 164, 177](Chapter 5) To fully understand the mechanisms of foam collapse, it is nevertheless important to have an idea of temperature changes in volcanic rocks and the resulting degassing timescales. Isothermal bubble growth during depressurization, however, does not account for many situations in volcanic eruptions. Magma remains for extended periods of time in the Earth's crust stationary and hot. During such times bubble growth that occurs at high temperatures and isobaric conditions is diffusion-controlled. Isobaric conditions also prevail in volcanic domes. Here, ripening and strain of the vesicular magma as well as ongoing bubble growth were presented as the main process controlling increases in permeability and thus open degassing [28, 51]. But at the same time, temperatures are not constant and volumes of individual rocks are finite. If there is no change in pressure and the pores are sealed, diffusion is the only way of collapsing the vesicles in these magmas. Sealing of individual pieces of vesicular lava can happen during fast quenching in air (such as breadcrust bombs [189]) or in

water [132]. Volcanic domes show highest permeabilities along fractures in the magma itself [136] and the surrounding conduit walls [135], which indicates that the foams in magma are often spatially constrained to single blocks surrounded by hot atmosphere. Isobaric conditions prevail at any stage of volcanic eruptions, however, the growth and collapse of bubbles within the magma that are purely controlled by diffusion, are poorly understood. Water measurements in vesicular rocks proved to be difficult with conventional FTIR techniques, however, synchrotron sourced FTIR allows for measurements at high spatial resolution and signal to noise ratios. This opens new possibilities for the investigation of bubble growth and collapse by water diffusion, which is essential to understanding volcanic eruptions.

Here we synthetically grow and collapse bubbles in isobaric conditions and measure the resultant water distributions in natural rhyolitic glass to create a tool to identify bubble growth and collapse mechanisms in volcanic rocks.

3.2 Methods

Glassy (<5 vol. % crystals), peraluminous rhyolite samples were collected from a road cutting exposure of the surface of Ben Lomond Dome, New Zealand [154]. A macroscopically homogenous hand-sample of pristine glass was cut into cylindrical cores of around 9.6 cm length and 1-2 cm diameter. Of each of these cylinders, a thin slice was kept to determine initial water concentrations. The samples were heated to 950 °C within 45-50 min, held at constant temperature for 2-24 h and cooled either to room temperature or to 850 °C where they were kept for the same amount of time (e.g. 12 h each and 24 h in total; Fig. 3.1). The samples were then quenched within about 20-30 min below 700 °C by shutting off the furnace. There were no visible changes of the volume during heating and cooling. Timescales were chosen to be in the minimum range of cooling rates of volcanic rocks [30, 49, 64].

Volumetric changes were recorded visually through a window into the furnace, and temperature at the sample was monitored with a thermocouple. The volume change was tracked by measuring the area of the profiles of the cylindrical cores. Gray-scale thresholds for the visual tracking had to be corrected for contrast changes at temperature changes. The measured area may include areas of the top of cylinders and shadows and, therefore, these data are slight overestimations. Because the initial samples did not show any porosity, any increase in volume represents the overall porosity. An equal growth factor for length and width of the cores was assumed to be able to estimate the volumetric changes. The volume change and the preservation of the aspect ratio could be confirmed by measuring dimensions of the cylindrical cores before and after

the experiments. Porosity estimates were confirmed by Helium pycnometry [82] on a sample of the same suite of rocks after heating to 950 °C. The initial samples and the foamed samples were cut into wafers of 130–180 μm and doubly polished. The water concentrations were measured at the IR microspectroscopy beam line of the Australian Synchrotron, using Fourier transform infrared spectroscopy (FTIR) with a step size of 3 μm and an aperture of 5 μm by 5 μm. Overview maps of water distributions were collected offline, using a focal plane array (FPA) detector at a pixel resolution of 2.7 μm. Despite similar spatial resolution of measurement points, signal to noise ratios were drastically higher for measurements using the globar light-source of the offline setup. Even with high resolution, the first three measurement points closest to textural features such as bubbles were rejected to ensure defect-free glass. The error in concentration depends largely on the thickness measured by micrometer, which is rated at ± 2 μm; however, we conservatively estimate the error to be within $\pm 2.5\%$ considering slight wedging of some of the wafers. Each area was also visually checked for bubbles and heterogeneity by moving the focus through the thickness of the wafer. Observations in low-resolution maps were checked with high-resolution online measurements. Total water contents were quantified using the band of fundamental OH stretching at a wavenumber of 3576 cm^{-1} [160]. The absorbance was taken as the height of the peak above a linear baseline. A density of 2350 kg/m^3 [154] and a molar absorption coefficient of 88 l/mol·cm [46] were used as representative of rhyolite.

3.3 Results

The samples show slight flow banding of microlites in thin section. All samples show similar volumetric changes during heating. Volume changes for isothermal and bithermal experiments are shown in Fig. 3.1.

After a short period of initial heating (40–45 min) foaming occurs at increasing rates of up to 1% of the maximum volume per minute. The peak in growth is reached after about 200–300 min., after which the growth slows down until the maximum volume is reached (Fig. 3.1). At this point, the volume more than doubled. This foaming can occur heterogeneously, forming bulges during initial stages of growth (Fig.3.2a(i)). After the growth phase, the volume of the samples slowly decreases by up to 10% of the maximum volume at a constant rate, and small dimples form at the surface of the samples (Fig. 3.2: B(i) and C(i)). The decrease in volume after the initial growth is not significantly higher for samples that had a cooler temperature step (See Fig. 3.1).

Maximum vesicle sizes are $\approx$1 mm in diameter, and minimum vesicle sizes are on the order of 5 μm. Signs for bubble coalescence such as thinned inter-vesicle walls and

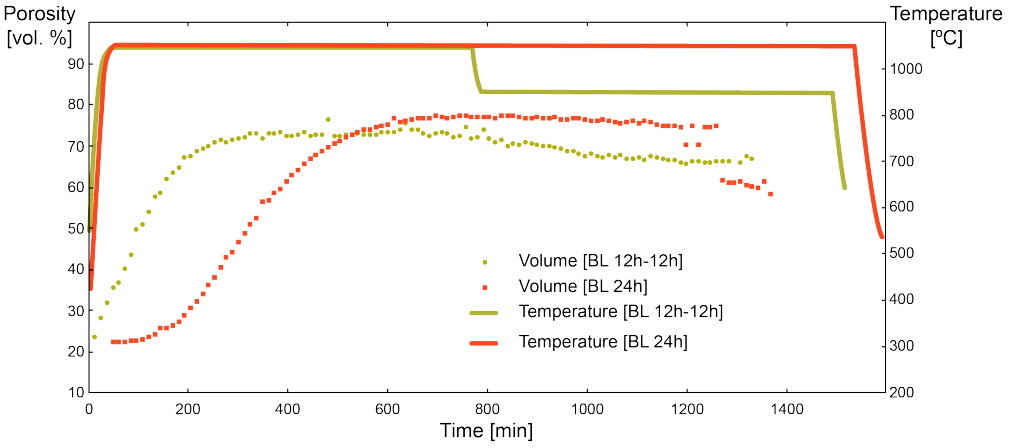

FIGURE 3.1: The porosity of two samples of Ben Lomond obsidian during heating for 24 h at 950 °C and 12 h at 950 °C followed by 12 h at 850 °C. Porosities are estimated by visual tracking of the profile area. The temperature was recorded at the base of the samples.

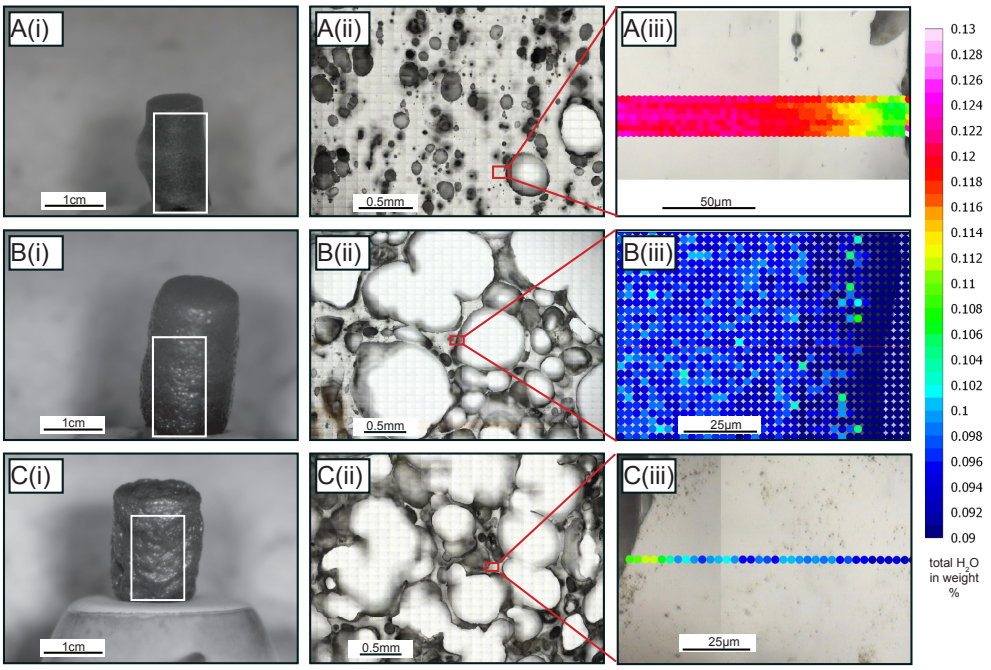

FIGURE 3.2: Experimentally foamed samples and their water distribution patterns around vesicles; Top row (A): Sample after 3 h at 950 °C, Middle row (B): Sample after 24 h at 950 °C; bottom row (C): Sample after 12h at 950 °C and 12h at 850 °C; Left column (i): samples at the end of each experiments, white boxes show initial dimensions; Middle column (ii): overview photomicrograph of each sample area; Right column (iii): overview of water distribution in each area, bottom map (C (iii) shows offline measurement to give a better overview, online data can be seen on Fig. 3.4.

vesicle collisions can be observed in samples that were heated for 24 h but in general, vesicles are round and show no contact to other vesicles. Within the samples, bands of higher vesicle number density and larger vesicles can be observed in some of the samples. These bands of higher porosity are parallel to the direction of microscopic flow banding. Overall volumes change by about 50% after 3 h to about 78% after 24 h at 950 °C (See Fig. 3.1). These volumetric changes are equivalent to the overall porosity, as starting porosity was zero. Pycnometric measurements of samples that were foamed for 24 h at 950 °C show a similar total porosity at ≈70% of which ≈62% is closed porosity. The samples do not show any significant difference in their volumetric changes when a second, cooler temperature step is added. All samples show a 50–80 μm skin of bubble free glass on the outer surface of the sample independent of their cooling temperatures (See Fig. 3.3). Based on their thermal history and the resulted foaming, the experiments are divided into three groups:

A Samples heated to 950 °C for periods during which the maximum volume was not reached (t<5 h)

B Samples held at 950 °C for long timescales at which the samples had fully foamed. (t≈24 h)

C Samples that were cooled to 850 °C after being heated to 950 °C and reaching maximum volume.

The water contents of the samples were measured using synchrotron source FTIR for detailed maps and conventional FTIR with an FPA detector for lower resolution overview maps. Initial water contents of the samples are consistent with previous studies on rocks from the same outcrop by [154, 156] at an average of 0.16 wt. % ± 0.2 wt. %. These initial water contents vary slightly across flow bands, which appear as slightly darker, parallel lines of usually a few micrometers to a few hundreds of micrometers. The average water contents of the heat-treated samples range from 0.045–0.14 wt.%. A total of 46 FTIR measurements were collected around bubbles and across rims (see 3.1). The glassy, bubble free rims (See Fig. 3.3) around all samples show a water decrease towards the surface of the sample down to 0.045 wt.%, which represents the minimum water contents measured in the samples.

Samples of group A (heated to 950 °C for 2-3 h) show mostly decreases of water towards the bubbles (e.g. sample BL 3-3 in Fig. 3.4). These gradients occur over typical lengthscales of 50-100 μm. Samples of group B (heated to 950 °C for 24 h) show mostly homogeneous water distributions around vesicles (e.g. sample BL 3-5 in Fig. 3.4). Increases can also be found in some samples with just one temperature step, however,

Sample	map	time		gradient toward bubble +/-	size (diameter longest axis in µm)	synchrotron source
BL 2-2	3	2h		-1	275	
BL 2-2	3	2h		-1	80	
BL 2-2	4	2h		0	115	
BL 2-2	1	2h		1		x
BL 2-2	3	2h		0		x
BL 2-4	1	2.5h		0		x
BL 2-4	2	2.5h		0		x
BL 2-4	3	2.5h		-1		x
BL 2-4	4	2.5h		-1		x
BL 2-4	5	2.5h		-1	50	x
BL 2-4	5	2.5h		-1		x
BL 2-4	1	2.5h	rim	-1		
BL 2-4	2	2.5h		0		
BL 2-4	3	2.5h		0	100	
BL 2-6	1	15h	rim	-1		
BL 3-3	1	3h		-1	100	
BL 3-3	2	3h		0	100	
BL 3-3	3	3h		-1	1000	
BL 3-3	4	3h		-1	100	
BL 3-3	4	3h		-1	70	
BL 3-3	2	3h		-1	450	x
BL 3-3	3	3h		-1	450	x
BL 3-3	4	3h		-1	450	x
BL 3-3	5	3h		-1	55	x
BL 3-3	7	3h		0		x
BL 3-5	1	24h		-1		
BL 3-5	2	24h		0	650	
BL 3-5	3	24h	rim			
BL 3-5	3	24h	rim			
BL 3-5	4	24h		0	900	
BL 3-5	5	24h	rim			
BL 3-5	5	24h		0		
BL 3-5	6	24h		0	1000	
BL 3-5	6	24h	rim			
BL 3-5	1	24h		0	1200	x
BL 3-5	2	24h		0	1200	x
BL 3-5	3	24h		0	120	x
BL 3-5	5	24h		0	15	x
BL 3-5	6	24h		0	1700	x
BL 3-5	4	24h		0	100	x
BL 3-5	7	24h		0	55	x
BL 6-1	1	2h/2h		-1	110	
BL 6-1	1	2h/2h		1	80	
BL 6-1	2	2h/2h		0	140	
BL 6-1	2	2h/2h		0	120	
BL 6-1	2	2h/2h		0	500	
BL 6-1	2	2h/2h		-1	250	
BL 6-1	2	2h/2h		-1	350	
BL 6-1	1	2h/2h		1	80	x
BL 6-1	3	2h/2h		0	550	x
BL 6-1	4	2h/2h		0	100	x
BL 3-2-2	1	4h/4h		-1	1000	x
BL 3-2-2	1	4h/4h		-1	500	x
BL 3-2-2	2	4h/4h		1	300	x
BL 4-2	1	12h/12h	??			
BL 4-2	2	12h/12h		0		
BL 4-2	2	12h/12h		1	350	x
BL 4-2	3	12h/12h		0	800	x
BL 4-2	1	12h/12h	rim			x

TABLE 3.1: All measured samples and a qualitative description of the water distribution patterns around bubbles: 1: increase towards bubble, -1: decrease towards bubble, 0: no gradient or no conclusive gradient; times refers to time at 950 °C or at 950 °C/850 °C.

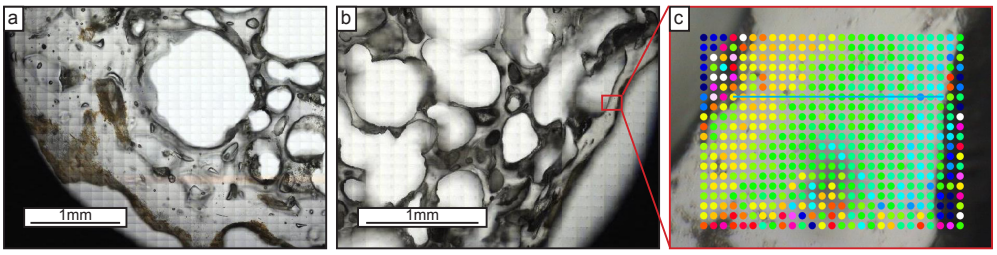

FIGURE 3.3: Fotomicrographs of (a): Sample after 24 h at 950 °C (same as Fig. 3.2,B(i)) (b) and (c): Sample after 12h at 950 °C and 12 h at 850 °C (same as Fig. 3.2,C(i))

only in shorter lengthscales of $\lesssim$10 μm which is at the limit of the spatial resolution and could be related to analytical artifacts or to quenching effects. Samples that were cooled to a second temperature step at 850 °C often show increases of water by up to $\approx$0.015 wt. % around vesicles at shorter length-scales of usually below 50 μm with mean length-scales around 20 μm (e.g. sample BL 4-2 in Fig. 3.4).

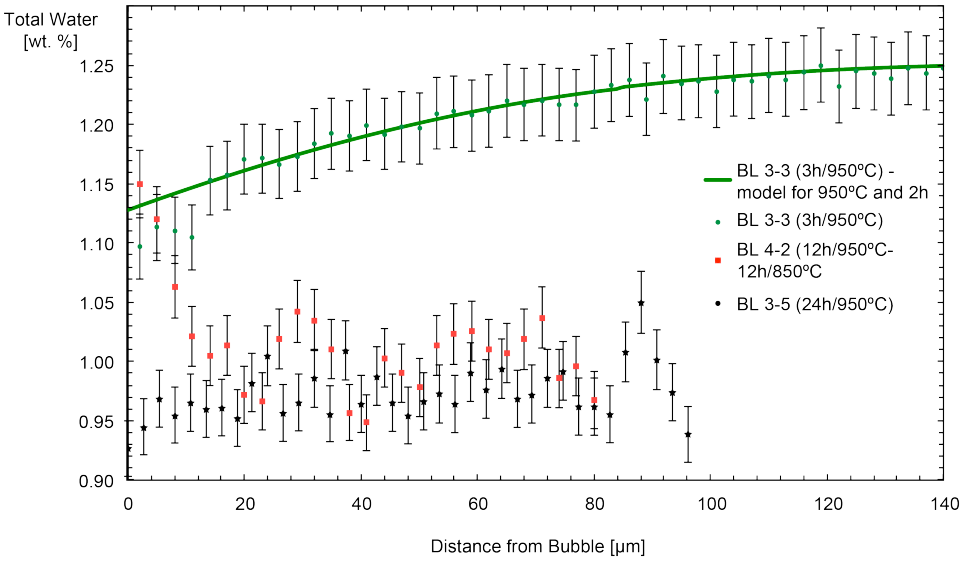

FIGURE 3.4: Water concentrations around vesicles after different thermal treatment. Refer to the text for detailed description.

3.4 Discussion

Our experiments provide insights into the processes of water diffusion during isobaric bubble growth, equilibration, and cooling. Water distribution profiles around bubbles vary depending on the thermal history during foaming. Samples contain 0.045-0.14 wt. % H_2O, which means that they are oversaturated at 950 °C and atmospheric conditions.

As a result, bubbles nucleate, water exsolves, then water diffuses into the growing bubble [126, etc.]. A range of different bubble sizes exist (Fig. 3.2A (ii); B(ii); and C(ii)) in each sample from all three different experiments which indicates that nucleation continues during the initial bubble growth stage [170]. The collapse of the samples by about 5% of their maximum volumes can be explained by degassing of the outer rims such as seen in experiments by Yoshimura and Nakamura [192]. They interpreted this as diffusional loss of water before bubbles could form. A dimply surface suggests a bursting of bubbles, leaving behind small indents and a degassed skin. However, a negative gradient of water (Fig. 3.3) towards the outside of the sample indicates additional diffusion. We assume that the minimum solubility of the samples at the experimental temperatures is represented by the water contents at the surface of the sample. These are as low as 0.045 wt.%, which is significantly lower than the average water content of the initial samples. It is also significantly lower than the minimum water content measured at the margins of bubbles in the inside of the sample (Fig. 3.2)

Without the possibility of losing volatiles through a permeable network of bubbles, gas flux is limited to the diffusion through the bubble-free rim, which prohibits equilibration within the timescales of the experiments. This impermeable skin prevents the interior of the sample from outgassing. After long timescales of foaming (24 h), the water contents equilibrate within the inside of the sample, however, at a higher level than the outside of the sample. This could be due to the increased pressures inside the samples, produced by limited expansion during bubble growth under the constraint of the outer rim of higher viscosity.

The decrease of water around bubbles from short (i.e. 2-3 h) single temperature step experiments shows a gradient typical for diffusion of water into the bubble. To demonstrate this we modeled the water distribution successfully by fixing concentrations at the bubble wall and the inside of the melt [177, 196]. Varying model parameters allowed us to match measured gradients with calculated timescales (see Fig. 3.4). These numerically derived timescales are close to actual experimental timescales validating the appropriateness of these models. However, the timescales are consistently shorter than the duration of the experiments (Fig. 3.4). This is expected, as it is unlikely that every bubble nucleated at the start of the experiment. Therefore, the timescale for the growth of an individual bubble is likely to be less than the timescale for the whole experiment. Unfortunately, the growth of individual bubbles could not be tracked, and neither onset nor terminus of growth can be estimated except by tracking of water diffusion.

As soon as bubble growth starts, heterogeneity in water concentration is created and water is moved following the diffusion-controlled growth of this bubble. This initial step of growth is purely dependent on the diffusion rate. Most negative gradients were

observed towards bubbles in samples that were heated for only a few hours, which represents the stage of fast growth. The overall decrease of water around vesicular areas in natural volcanic rocks was measured by Castro et al. [28], who determined rates of volatile loss between 2 x 10^{-4} to 3 x 10^{-3} wt.% h^{-1}. These dehydration rates from decompression are similar to the dehydration caused by heating in this study. The presented results can, therefore, also be seen as an analog to isothermal decompression of volcanic rocks.

The majority of vesicles in samples that were heated for 24 h do not show significant water gradients. However, they do show reduced water contents compared to the three hour experiments. We compared vesicles of equal size, and the overall water contents were consistent around the vesicles. Within the sample overall water contents varied and water gradients showed a decrease toward the outside of the sample. We propose that the bubbles within these samples equilibrated to a pressure associated to the pressurized interior of the foamed sample and that diffusion continued towards the outer rim of the sample. In this closed system, a new equilibrium pressure is reached and gradients towards bubble walls are lost, however, diffusion toward the sample surface and atmospheric pressure continues.

The samples that were cooled by 100 °C still allowed reasonable fast diffusion. In these samples increases in water content were common around vesicles. We interpret this as a result of increasing water solubility in the melt [71, 191]. The increasing solubility allows water to diffuse from the bubble back into the melt, driven by the lower temperature, and decreases the pressure within the bubble. This decrease in bubble pressure is not manifested by a large shrinkage in bubble volume, although some increased shrinkage was apparent (Fig. 3.1). The gradients we observe are steep and short, indicating short timescales of diffusion. The length of these gradients is similar for different bubble sizes and timescales of the experiments. Therefore, we cannot exclude the possibility of the increases being a quench process at lower temperatures.

The formation and collapse of bubbles generates diffusion gradients that redistribute water in the melt. Water diffuses into growing bubbles and produces negative gradients until bubbles have grown to equilibrium size proportional to their internal pressure. When these bubbles are cooled in an additional temperature step, water resorbs back into the melt due to a retrograde solubility of water.

3.5 Implications

The growth of bubbles in a static finite volume of magma is accompanied by bubble collapse on the surface of the melt. This leads to the formation of a water-depleted, impermeable skin that effectively limits further degassing of the magmatic foam. Explosive volcanic eruptions are often followed by effusive phases, during which volcanic conduits may be sealed with less permeable plugs of magma [42, 77]. However, the growth of domes is usually accompanied by structural failure of parts of these plugs [89]. Permeability of these plugs seems to be localized to structural weaknesses [136]. This contradicts the perception of a homogeneous and continuously degassing permeable foam. The temporary formation of thin, impermeable skins could lower the overall permeability of even highly vesicular foams drastically [79]. This would allow brittle failure on small scales to be crucial in controlling larger scale permeability [32]. For example, when the skin is removed of our sample, connected porosity increases drastically and the sample would collapse completely when heated well above T_g. We show that negative gradients of water concentrations develop around growing bubbles at experimental timescales of 3 h. All our experiments were conducted at isobaric conditions and, they were driven by a water supersaturation. Therefore, we propose that some of our results can be discussed with relevance to the diffusion into bubbles during ascent. We acknowledge that during ascent, depressurization may lead to further bubble expansion. Additionally, internal shearing within the ascending magma could increase permeability [118] and disrupt degassing skins.

We envisage several scenarios where magma/lava stagnates, re-equilibrating with new isobaric conditions (Fig. 3.5): (a) In a magma chamber, (b) in a conduit following an eruption(s) (c) in a lava flow or dome, or (d) as a pyroclast post eruption. In all these instances diffusion-controlled growth continues and volatile gradients are modified before a new equilibrium is reached. This new equilibrium can be affected by pressure fluctuations, CO_2 fluxing, or temperature variations [180]. Future studies of water distribution around bubbles can use this study to assist with their interpretations of the complex history of bubble formation during magma ascent. For the possible different patterns of water distribution (Fig. 3.5, (i)) around bubbles we present three possible scenarios (Fig. 3.5, (ii)):

1. Water depletion around vesicles: Water diffused towards the bubble in response to a diffusion gradient associated with a growing bubble (Fig. 3.5 a and b). Therefore, in the case of an explosive eruption one of the most likely causes for this hydration pattern was bubble growth followed by fast quenching (e.g. tephra being ejected after fragmentation of a bubbly magma(Fig. 3.5 b(ii))).

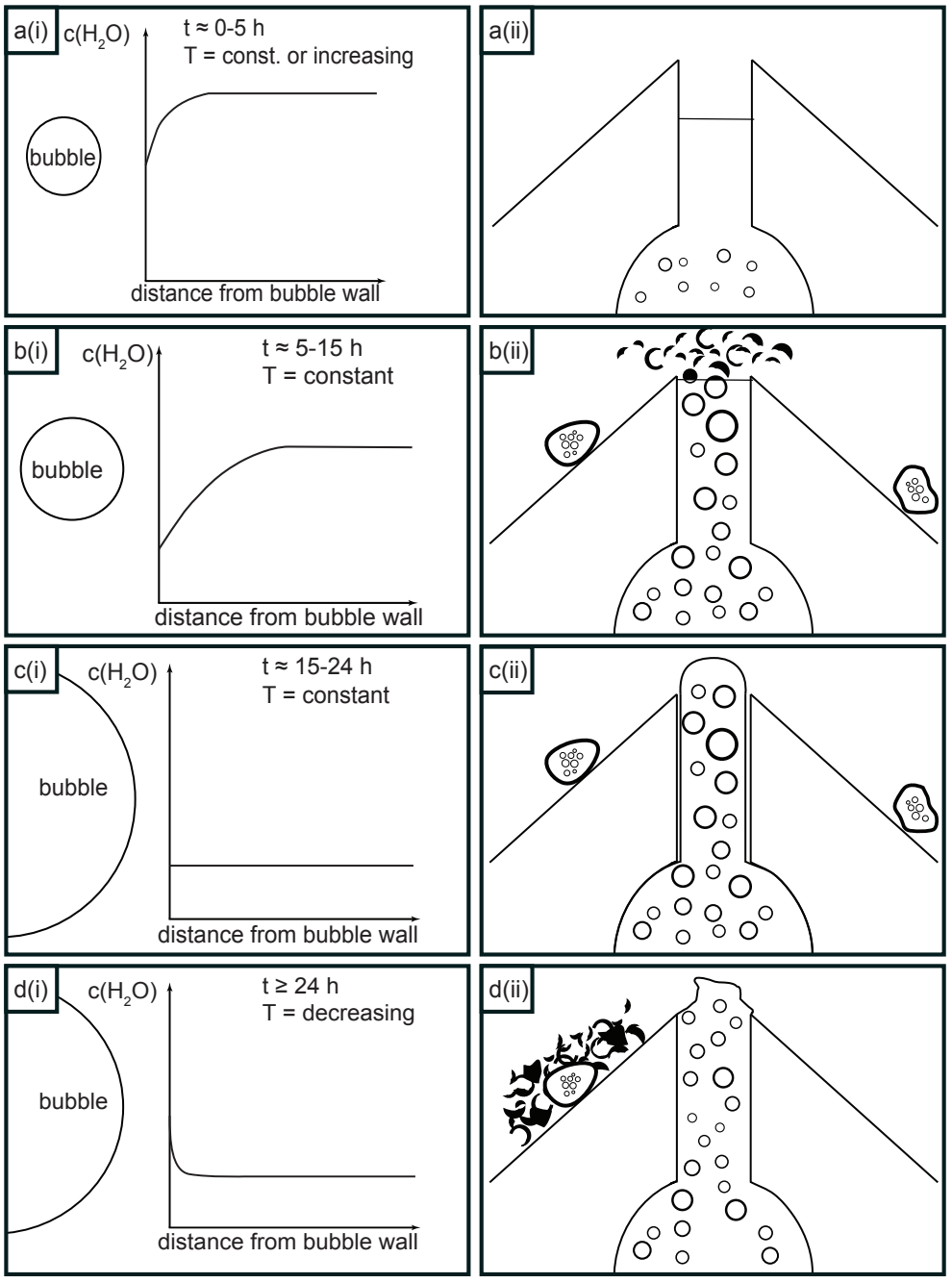

FIGURE 3.5: Possible water distribution patterns around bubbles and their eruptive products. : Left column: Possible water gradients found around vesicles in rhyolitic rocks at different timescales of growth, vesicle sizes should be seen as relative sizes of one individual vesicle. Right column: Possible scenarios and places within a volcano where these parameters apply. Refer to the text for detailed description.

2. Homogeneous water distribution around bubbles (Fig. 3.5 c): Bubbles have been quenched from equilibrium of volatile concentration in melt vs. bubble. Possible reasons for this could be:

   - Quenching of foamed melts that remained at magmatic temperatures at the surface for long timescales (≈15–20 h in our experiments) and did not experience plolonged periods at lower temperatures during cooling. This could be in the crust of a lava flow, dome or a large pyroclast (Fig. 3.5 c(ii)).
   - Depressurization and eruption of a stalled magma that occurs sufficiently rapidly to quench this equilibrated magma. An example of this could be the eruption of co-magmatic conduit wall material in a plinian eruption (Fig. 3.5 c(ii)).

3. Increasing water concentration in glass around bubbles (Fig. 3.5 d): Bubbles were either re-pressurized (as described by Watkins et al. [180]) or cooled stepwise, allowing retrograde solubility. Stepwise cooling can either occur when the ascent, eruption, or emplacement of the magma partially or completely stagnates or cooling is slight, such as during dome growth- and collapse or embedding of pyroclastic products (Fig. 3.5 d(ii)). In this scenario the resorption of isolated bubbles in a melt eventually leads to textural obliteration and the densification of a melt/magmatic suspension. The process we describe induces modest resorption but with the application of pure shear stress and over longer timescales this may be a contributing process to the formation of surficial low-porosity, water-rich obsidian [e.g. 119].

3.6 Conclusion

We show that in hydrous, rhyolitic melts bubbles grow for several hours at moderate heating rates above the glass transition. During this time, water diffuses into nucleating and growing bubbles, which can be detected as negative gradients of water concentration towards bubble rims. After this initial stage of bubble growth, bulk volume decreases as bubbles burst on the surface and form a sealing skin. Water concentration homogenizes until equilibrium after 24 h at constant pressure and temperature. During cooling and re-equilibration at a lower temperature, water may be resorbed into the melt surrounding the bubble.

Preamble

In Chapter 3, I showed that water profiles around bubbles grown in the laboratory reveal details of the timescale and equilibrium status of the growing and collapsing bubble. In Chapter 4, I apply this approach to naturally grown and collapsed bubbles in effusive lavas and pyroclasts to reveal the behavior of water during flow band formation. After an initial explosive phase, most volcanic eruptions change into more effusive eruptions styles. During effusive eruptions at intermediate and high-silica volcanoes, domes and short, glassy flows are produced. The affected material is less porous and permeable, which can lead to the formation of plugs that can build up pressure within the volcano. In contrast to foamy magma responsible for explosive eruptions, the rocks of volcanic domes, plugs and flows can be dense and flow banded. However, the behavior of water during bubble collapse, and flow band formation remains poorly understood. Flow bands are parallel or sub-parallel heterogeneities in crystal or bubble number densities that range from micrometer to meter scale. We propose that flow band formation is intricately linked with bubble collapse. The same tools of volatile analysis as described in Chapter 2 allow for detailed cross-sections of water distribution across flow bands. In this chapter, I use examples of water heterogeneities across flow bands and bubbles in cooling rocks, to assess the association of flow band formation with bubble collapse and lava cooling.

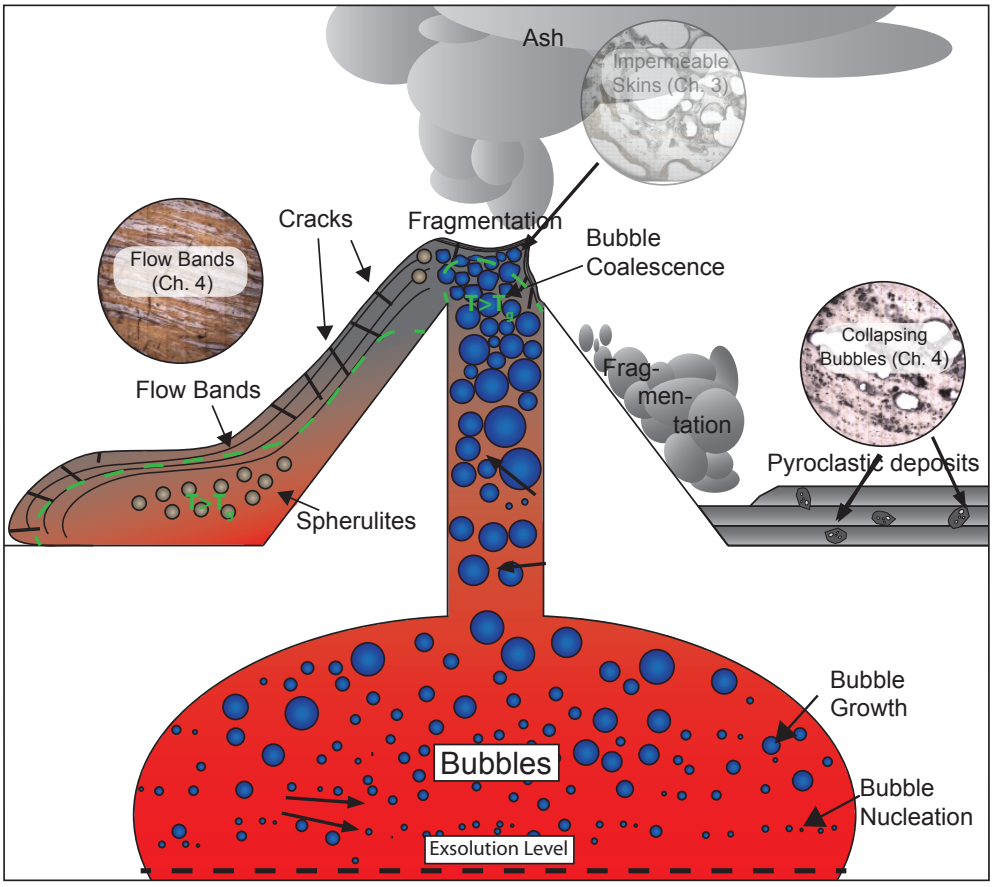

FIGURE 3.6: Overview of textures in Chapter 4

Chapter 4

Flow band formation in vesicular magma

4.1 Abstract

Flow bands in volcanic rocks are an important proxy of flow directions and rheological properties of magma during emplacement. Flow bands are local changes in color, crystal content and/or bubble number density that are usually parallel to the direction of shearing. Water heterogeneities in rhyolite lava flows are spatially associated with flow banding. However, the nature of the mechanisms that leads to the association of water distribution and flow bands is not fully understood. We present preliminary data of water distributions across vesicles and flow bands in New Zealand rhyolitic volcanic rocks from Ben Lomond, Ngongotaha and Mayor Island. Glassy rocks from Mayor Island show an increase of water around vesicles and water heterogeneities associated with bubble collapse textures. A sample from Ben Lomond, shows local increases of water across subtle flow banding without obvious associations to specific textural features such as bubbles or crystals. In addition, we show water heterogeneities across flow bands of microlites in a sample from Ngongotaha dome, which are parallel to the alignment of the crystals. Increasing water contents across flow bands could be interpreted as water heterogeneities from water resorption during bubble collapse. We suggest that, following outgassing through a permeable network of bubbles, a strained magma can ultimately lose its entire vesicularity, through a final stage of bubble resorption. This can be followed by crystal growth along the direction of shear. We integrate our new findings to produce a unifying model of flow band formation. We show that shearing of magma can produce

local increases in water concentration linked to the collapse of bubbles and crystals.

4.2 Introduction

Flow bands are parallel heterogeneities of bubbles and/or crystals along the direction of strain in volcanic rocks [27]. This texture is common in rhyolitic lava and dykes [e.g. 5, 27, 62, 140, 141, 145, 152, 172, 174] and can be used as a proxy for flow direction [5, 145] and shearing of lava [23, 26, 96, 134]. The formation of flow bands is suggested to be a result of either laminated mingling of melts of different volatile contents [62, 140–142], the fragmentation and rewelding of magma during ascent [174], or the collapse of foams of a melt [19, 118]. An overview of common flow band textures is given in Fig. 4.1.

Flow bands may be visible due to variations in crystal content (Fig. 4.1 a), vesicle content (Fig. 4.1 b), spherulite content (Fig. 4.1 c) or changes in color (Fig. 4.1 d). Increased crystal number densities along flow bands (Fig. 4.1 a) form by mingling of two batches of magma with different crystal- and/or water contents and/or bulk chemistry [141]. Vesicle contents may vary between flow bands (Fig. 4.1 b) because of heterogeneous degassing. Bubbles can coalesce and form a permeable network through which outgassing can drive foam collapse [185]. Additionally, coalescence and permeability increases when the foam is sheared [19, 118]. Flow banded lavas frequently show variation in bubble content with evidence of bubble collapse and coalescence (Fig. 4.1).

Water resorption was detected around vesicles (Chapter 3, [180]) and in welded deposits [149]. It is common that the spherulite content may be distinct between flow bands (Fig. 4.1 c) [29, 140, 177], which has been associated with higher water contents [140]. Alternate grading in brown to black or gray colors (Fig. 4.1 d) is either formed by heterogeneities in redox states of iron nanolites [30] or the abundance of microlites [142]. The formation of flow bands due to fracturing or fragmentation of rock could as well cause changes in crystal content [62, 174].

A characteristic of flow-banded lava is a frequent and systematic variation in water content (Fig. 4.2). Generally, the water content of magma is controlled by its solubility and varies according to pressure and, to a lesser extent, temperature, and volatile and magma composition [194]. Pressure decreases during ascent and water exsolves and forms bubbles. The water diffuses into the bubble, depleting the surrounding melt ([28, 125] and Chapter 3). Pressure can also increase prior to eruptions, which can enrich the melt surrounding bubbles in water [180]. Ascent rates within the rising melt vary

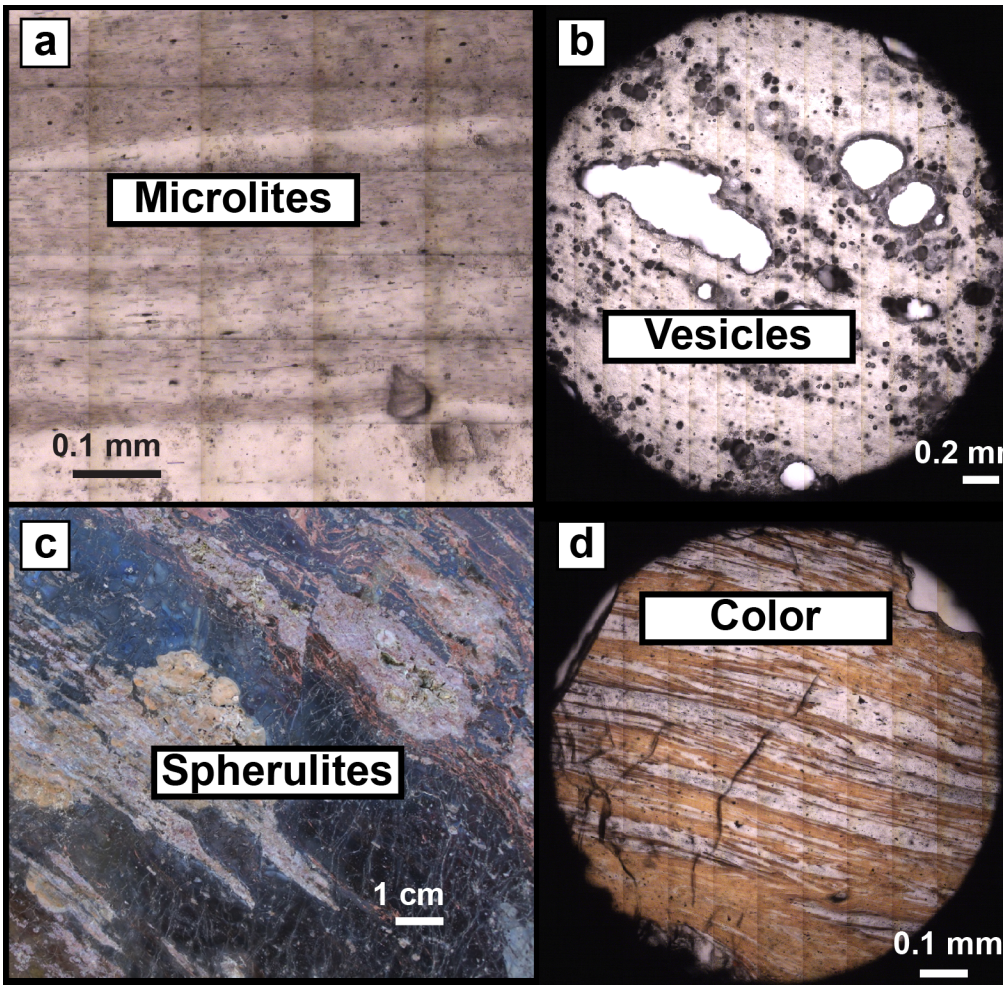

FIGURE 4.1: a: microlite flow bands in a sample from Ngongotaha dome (sample Ng11-1c); These flow bands consist of sub-parallel microlites. A microphenocryst at the bottom right corner slightly deflects the generally relatively straight boundary of a flow band. b: Sample MICA from Mayor Island, New Zealand; This sample of obsidian shows comparatively large vesicles that are well aligned. c: A sample from Ngongotaha dome, containing bands of increased amounts of spherulites. d: Sample from Ngongotaha dome containing red, thin bands. The red bands could be the result of heterogeneous iron oxidation states similar to the Fe-redox redistribution observed by Castro et al. [30] around spherulites.

largely across the conduit which produces shearing and locally varies pressure and water heterogeneities [114, 180]. As the melt cools, water solubility of the melt/glass generally increases, which could drive water resorption around bubbles ([180, 191]Chapter 3). Similarly, a change in volatile composition (e.g. CO_2/H_2O) could also drive water resorption [180]. A melt that crystallizes anhydrous crystals will also increase its water content [29, 177].

Profiles of water around bubbles can preserve information about the growth [28](Chapter 3) as well as the collapse of bubbles in quenched glass [180](Chapter 3). The use of synchrotron radiation for Fourier transform infrared spectroscopy (FTIR) makes it possible

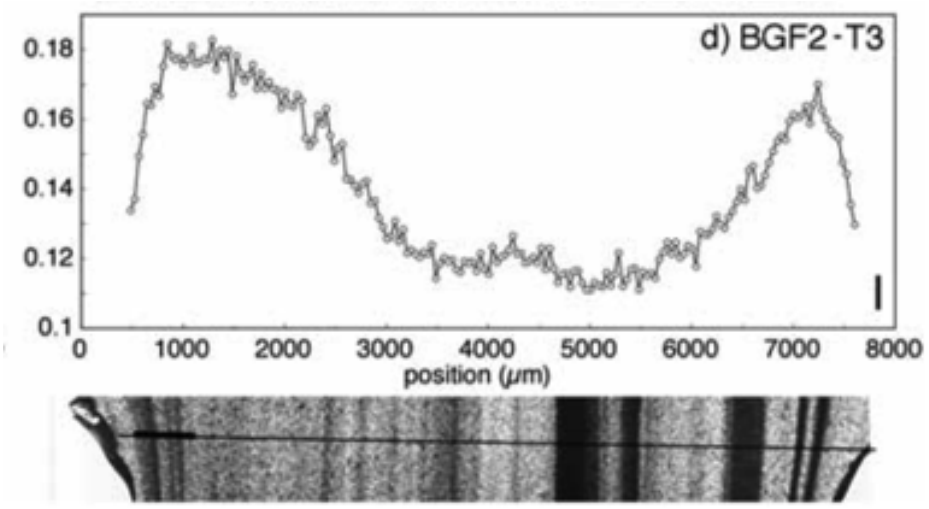

FIGURE 4.2: Water contents (in wt.%) across a flow banded sample in Castro et al. [28].

to measure the distribution of water at a very high spatial resolution around textural features. By measuring water across bubbles and flow bands, we assess the evolution of flow band formation by bubble collapse. Crystal growth is known to redistribute abundant water such as during the growth of spherulites [e.g. 29, 69, 177, 181]. The layering of crystal rich bands in microlite flow bands can show fractal mixing patterns [62], and the orientation can be used to quantify strain within the lava [26]. Flow bands are generally created during shearing. In this study, we discuss textures of both vesicle- and microlite-rich flow bands, and present a conceptual model of flow band formation that includes both these processes based on similarities in patterns of water heterogeneity.

4.3 Methodology

All samples were doubly polished to a thickness of 100-200 μm perpendicular to apparent flow banding. Water was measured by FTIR at the Australian Synchrotron either using synchrotron radiation on a Bruker Hyperion 2000 microscope or a Bruker Hyperion 3000 equipped with a 64x64 pixel Focal Plane Array (FPA) detector. Online measurements were collected at a step-size of 3 μm and an aperture of 5x5 μm. The amount of total water was estimated using the peak height of the band at 3576 cm^{-1}, the absorption coefficient by [46] and straight baselines over consistent spectral ranges for each measurement. Direct measurements of hydroxyl concentrations were not possible due to their low concentrations and baseline shifts due to high crystal contents of sample b, and d. Only measurements of the total water (H_2O + OH) are presented. By keeping the samples

as thin as possible, the signal to noise ratios are high and scattering and absorption of the beam by microlites and nanolites is kept to a minimum. Thicknesses of the samples were measured with a micrometer and by measuring of interference fringes according to Nichols and Wysoczanski [113], yielding similar results. Thickness variations due to slightly wedged samples were assessed as negligible. Densities used to calculate concentrations were kept at a constant value of 2350 kg/m^3 from the study of Stevenson et al. [154]. Keeping parameters constant may introduce a slightly larger overall quantitative error ($\ll$5% of the total water contents), but qualitative measurements of small-scale variations are not affected and can be compared throughout all samples. Particular care was taken to avoid geometrical effects of the bubble margin in the sample A from MI by neglecting all measurements within 10 μm of the bubble margin.

4.4 Results

4.4.1 Sample description

Glassy, rhyolitic samples from Mayor Island, Ben Lomond dome and Ngongotaha dome in New Zealand were collected. The samples A and B from Mayor Island (MI) are both pyroclasts from the Te Paritu Tephra (described in Houghton et al. [72]) (See Fig. 4.3 a and b). MI A shows slight breadcrusting and is foamed along flow bands (fig. 3a) with maximum bubble sizes around 1 mm. Small bubbles down to 1 μm can be found throughout the sample. The bubbles often are slightly elliptical but show no signs of connectedness. The sample is almost crystal-free and contains <1% microlites. The breadcrust surface of the sample only shows slight inflation and is glassy and does not show open pores. The shape of the sample is angular but slightly bulged due to inflation. MI B does not show any signs of foaming or breadcrusting and is not bulged. It shows similarly low percentages of microlites, however, there is an abundance of submicroscopic (<1 μm) crystals that appear as brown bands in photomicrographs (Fig. 4.3 b (i) and (ii)). The bands are irregular and can end abruptly i.e. they usually do not taper out (Fig. 4.3 b (iii)).

The Ben Lomond Dome samples (Fig. 4.3 c) are from an outcrop previously described by [154] and were collected within 10 m of the surface of a lobe of the dome. While there are areas of heavy perlitization, spherulitization and bands of foam as well as wider bands of higher microlite number density, this sample was collected from an area of pristine, glassy and bubble free obsidian within the top ten meters below the lobe surface. Crystal sizes are in the micrometer range and considered microlites Sharp et al. [142]. The overall crystallinity of the sample is <1%, and fits the description of the

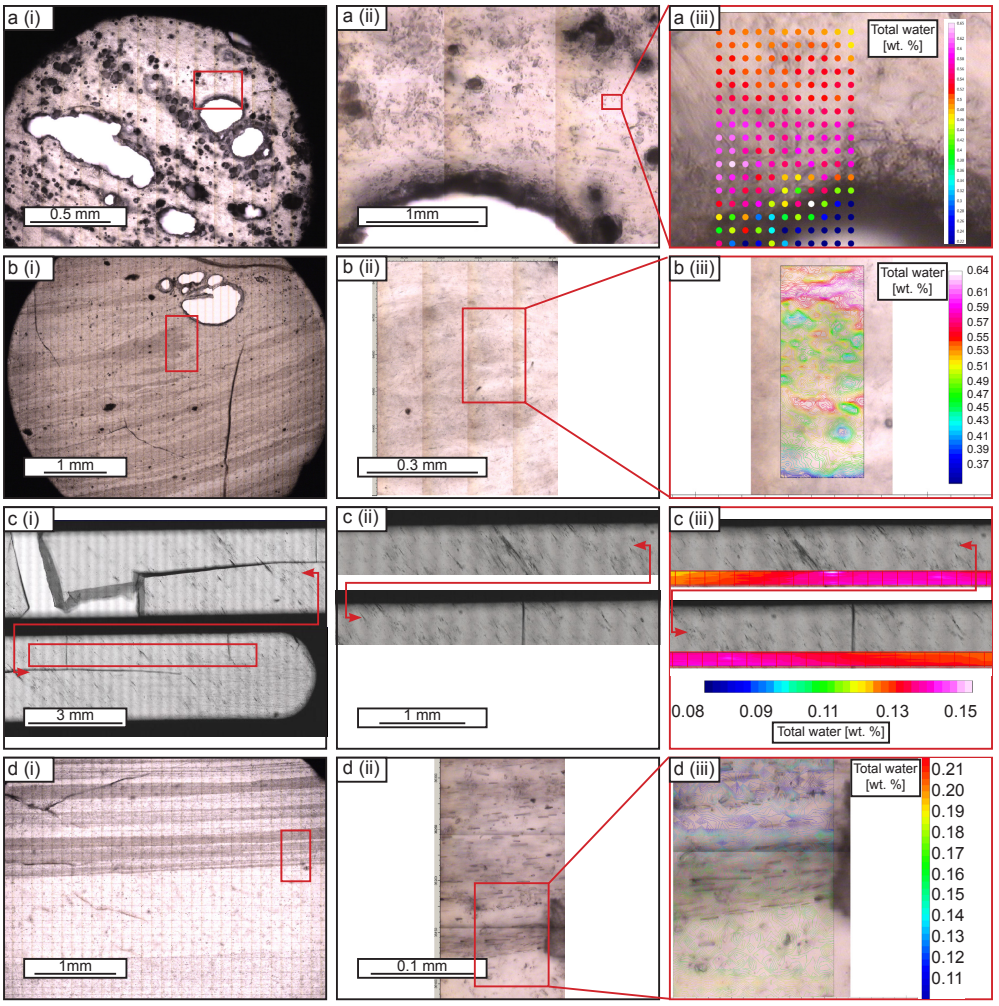

FIGURE 4.3: Overview of flow banded samples,their textures and water distribution patterns; a(i) Sample A from Mayor Island with vesicular flow bands, (ii) showing round isolated vesicles of varying sizes along linear bands, (iii). water increases can be found in the glass surrounding the vesicles. b(i) Sample B from Mayor Islandshows few bubbles and more irregular flow banding. b(ii) These flow bands are changes in color, possibly associated to devitrification and submicroscopic crystals. The bands are irregular and can end abruptly usually do not taper out b(iii).Water increases can be found in the brighter colored parts that fill interstices within and between the darker bands. c(i) A sample from Ben Lomond shows no obvious macroscopic flow banding c(ii) Narrow lines of usually >1 μm mark parallel flow banding c(iii). A wide increase of water could be detected in this sample. d(i) A glassy sample from Ngongotaha dome shows flow banding of varying thicknesses in the microlite number density. d(ii) Phenocrysts are rare (<5%) and not aligned with the microlites, which are sub-parallel to the flow banding. d(iii) Water contents change parallel to the macroscopic flow banding; however, the water heterogeneities only partially coincide with the margins of the flow bands.

sample BL6 of the study by Sharp et al. [142]. The few microlites in the sample show parallel banding (Fig. 4.3 c (ii)). Ngongotaha dome consists of more and less glassy lobes that all show heavy flow banding [5]. This particular sample (Fig. 4.3 d) shows parallel, sharp increases in microlite number density. There are no vesicles present and apart from little amounts of phenocrysts and spherulites ($\lesssim$5%), the microlites are surrounded by pristine glass. Crystal number densities vary widely in each separate band and individual microlites are well aligned (Fig. 4.3 d (ii) and (iii)).

4.4.2 Water analysis

Water distribution around bubbles and flow bands are shown in Fig. 4.3. The sample MI A shows slight increases of total water from 0.5 wt.% to 0.6 wt.% in over 3050 μm towards a $\approx$75 μm diameter bubble (Fig. 4.3 a (iii)). Water contents in the sample MI-B(Fig. 4.3 b (iii)) increase in the brighter zones between darker fingers and bands. This is especially apparent in the fingered end point where interstices of the darker melts are filled with hydrated glass. Overall water contents of the sample are similar to those of MI-A (Fig. 4.3 a (iii)) with 0.5–0.6 wt.%. Water in the almost bubble free glass of BL (Fig. 4.3 c (iii)), shows very uniform distribution compared to the foamed sample of MI. Sharp increases of water occur at the dark lines of microlites along flow banding. The total water, shows a systematic and gradual increase of $\approx$0.02 wt.% across a flow band. See Fig. 4.4

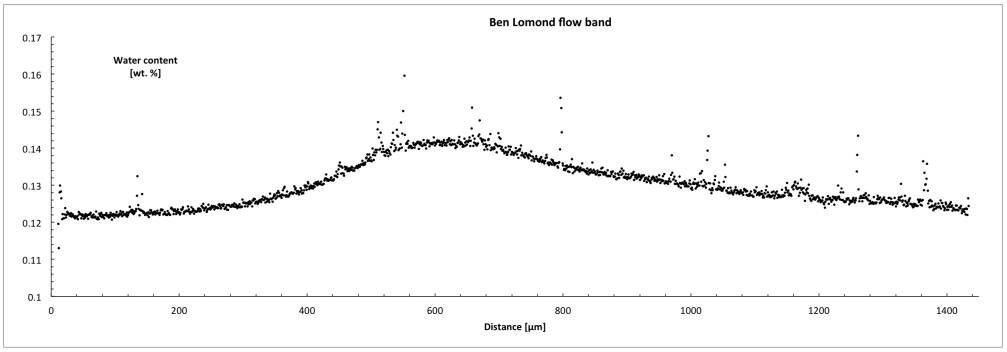

FIGURE 4.4: Water distribution across a flowband from Ben Lomond, NZ (Fig. 4.3 c (iii)).

4.5 Discussion

The textures and water concentration gradients reveal intricate magmatic and volcanic histories of the four samples. We propose that these four samples represent a continuum

and that each sample was quenched at a distinct stage. We integrate these stages into a model of flow band formation.

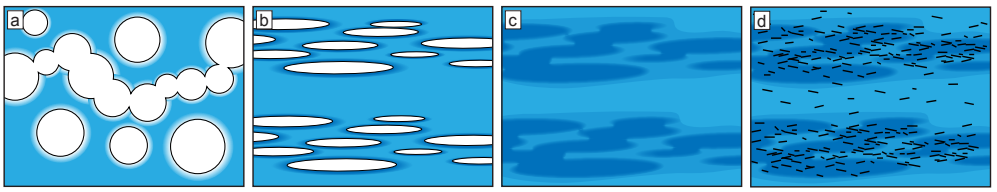

FIGURE 4.5: a: Water depleted haloes indicate exsolution growth of bubbles in the erupted/erupting foam of magma; b: shearing and rewelding during cooling and flow isolates, repressurizes and distorts bubbles driving water resorption. c: bubbles are entirely resorbed and water heterogeneities remain. d: crystals grow preferentially in the parts of the melt with higher bulk water concentration and may additionally redistribute that water into the melt. These crystals and water heterogeneities are further aligned due to continued shearing during flow.

The textures of pyroclast a from MI (Fig. 4.3 a) show signs of a complex thermal history. Flow banding indicates differential shear at temperatures above T_g. After fragmentation and emplacement bubbles continued to grow, and the quenched impermeable outer skin fractured forming a breadcrust texture. The increase in total water at the margin of the bubble indicates that either pressure increased [180], temperature decreased (Chapter 3, [149]), or that the composition of the volatile of magma changed [193]. We can exclude late hydration with meteoric water, as the sample was sealed by impermeable glass and the vesicles are not connected.

We propose that the pyroclast remained oversaturated in certain flow bands after fragmentation and eruption and foamed along flow bands with high water contents producing breadcrusting. Water then diffused back into the melt either due to the retrograde solubility of water during cooling (ref Chapter 3) in the magma or due to increased pressures in the vesicle due to hindered foaming after T_g was crossed. This could therefore be seen as an example of secondary resorption of bubbles in bubbly flow bands. Sample MI - B (Fig. 4.3 b) shows discontinuous flow bands and typical textures of foam collapse, comparable to fiamme in pyroclastic flow deposits [15, 102]. The water contents are higher in the areas of pristine glass. This could either be caused by heterogeneous exsolution or dissolution of water from the melt which is redistributed during flow and bubble collapse/bubbles.

If we assume a transition from a permeable foam to an impermeable bubbly melt such as in the case of MI-A, resorption and/or ripening with consecutive degassing are likely scenarios of formation of a non-vesicular, heterogeneously hydrated glass with the textures observed in MI-B. (see Fig. 4.5). The BL sample shows no textural association between domains of higher water contents, and phenocrysts, sub-solidus microlites or (Fig. 4.3

c (iii)). Small spikes are associated with nanocrystals or xenoliths (Fig. 4.4); however, these could be due to local artifacts caused by the crystals blocking the transmission of infrared light. The bulge in water contents (Fig. 4.4) is not a sharp increase and the lobes are close to symmetric, which excludes possible thickness effects of preparation issues. This would create either a rounded overall bulge or a distinct bend in the data.

Crystals can be observed in the samples, and these distinct sharp outliers are easily detected. The overall increase in total water could be due to heterogeneous degassing of water. However, resorption is also necessary to remove the last small bubbles account for the low porosity, as well as account for the elevated water contents. The equilibration time of hydrated or dehydrated bubble walls is hours to a few days 3. Equilibration across longer length scales of flow bands may require more time. The complete absence of textural evidence for bubble collapse indicates that this sample continued flowing after degassing, bubble isolation and regassing. Continued flow would allow mingling and juxtaposition of contrasting degassed and regassed bands with sharp boundaries [63]. However, we propose water diffused across these sharp boundaries in water content to produce the curve in Figure 4.4. The sample quenched before diffusion and equilibration was complete.

The sample from Ngongotaha dome (Fig. 4.3 d (iii)) shows an increase in water concentration across flow banding of defined by concentrations of microlites. Generally, water heterogeneities are parallel to the bands of microlites; however, the locations do not match exactly and there is an overlap (Fig. 3 d(iii)). Sharp et al. [142] concluded that microlite-rich, grey bands with up to 8% crystallinity were associated to late devolatization in an obsidian flow before flow band formation. However, Castro [24] showed that the processes leading to microlite-rich bands in obsidian are more complex and that microlites are not a reliable indicator of the extent of degassing. For example, the growth of sub-solidus microlites can preferentially occur in water rich flow bands [27].

The four samples presented in this study were chosen to represent a progression of events of texture formation that are associated with shearing and redistribution of water. Based on the textural observations and the water distributions, we suggest a conceptual model of flow band formation in bubbly magma (Fig. 4.5):

a A coalesced sheared magmatic foam degases through permeable pathways [118]. This depletes water around bubbles in permeable zones (Chapter 3) As these permeable zones collapse and continue to shear, residual bubbles become isolated and concentrate along shear planes.

b Bubbles isolated from permeable networks along shear planes completely resorb into the melt (Fig. 4.5 b and c). The remnant water heterogeneity from variably degassed and regassed flow parallel roughly shear planes (Fig. 4.5 c).

c Continued flow stretches and juxtaposes heterogeneous bands of water content, destroying textural evidence of bubble collapse (Fig. 4.5 c). Once shear upon a particular plane stops, water diffuses across this plane smoothing the contrast in water content (Fig. 4.5 c).

d The water-rich bands then act as zones of more rapid diffusion during sub-solidus crystal growth and microlites preferentially grow in these zones (Fig. 4.5 d).

We suggest that for sheared isolated bubbles with a small volume/surface area, resorption could be an effective process of bubble collapse and water redistribution. Such a mechanism produces significant bands of oversaturated melt, that could potentially refoam (Chapter 3). Our interpretation provides a model that allows bubble collapse and degassing in the conduit via a permeable foam [152, 185]. The potential of large volumes of oversaturated melt to remain in plugs and domes close to the surface also produces an intriguing mechanism to generate explosive eruptions without requiring replenished magma from depth.

4.6 Conclusion

We integrate our evidence of water resorption into a unifying model of flow band formation of (a) heterogeneous water degassing and foam collapse, (b) bubble isolation and rehydration, (c), continued flow, mingling and fractal band development and (d) late stage crystallization and enrichment. Bubbles in slowly cooling environments show signs of resorption due to the retrograde solubility of water in rhyolite. This can lead to the formation of water concentration heterogeneities across flow bands. Crystals are growing preferentially along these water heterogeneities. Therefore heterogeneous bubble collapse due to shearing drives the formation of flow bands and the redistribution of volatiles in magma. This has important implications for (1) the emplacement of lavas and welding of pyroclastic flow, and (2) volatile redistribution during ascent and the fragmentation and eruption of magma [e.g. 78].

Preamble

Chapter 4 explained how water is redistributed during growth and collapse of bubbly magma and shear during flow. Chapter 5 is the logical progression of Chapter 3 as once lava comes to rest it continues to cool. During cooling of volcanic flows, plugs and domes, flow band formation and bubble growth is prohibited by high viscosities. The viscous melt cools to a brittle solid and instead of flowing, the glass breaks under stress. Glass is unstable and crystals grow as it devitrifies. These crystals may form spherulites — radially growing spheres of crystals. Textures that formed during eruption may be altered drastically by crystal growth and cracking after emplacement. As cracks and crystals grow water is redistributed within the glass. I use similar techniques to Chapter 2 and 3 to map water distributions around textures. In this chapter, I discuss relations between crystals and cracks in cooling rhyolitic magma. I confine timescales and temperatures of the formation of cooling textures by correlating textural observations and maps of water distribution with diffusion modeling. The textures and the hydration discussed in this final chapter represent the final stage of texture formation during volcanic eruptions before the melt has fully cooled.

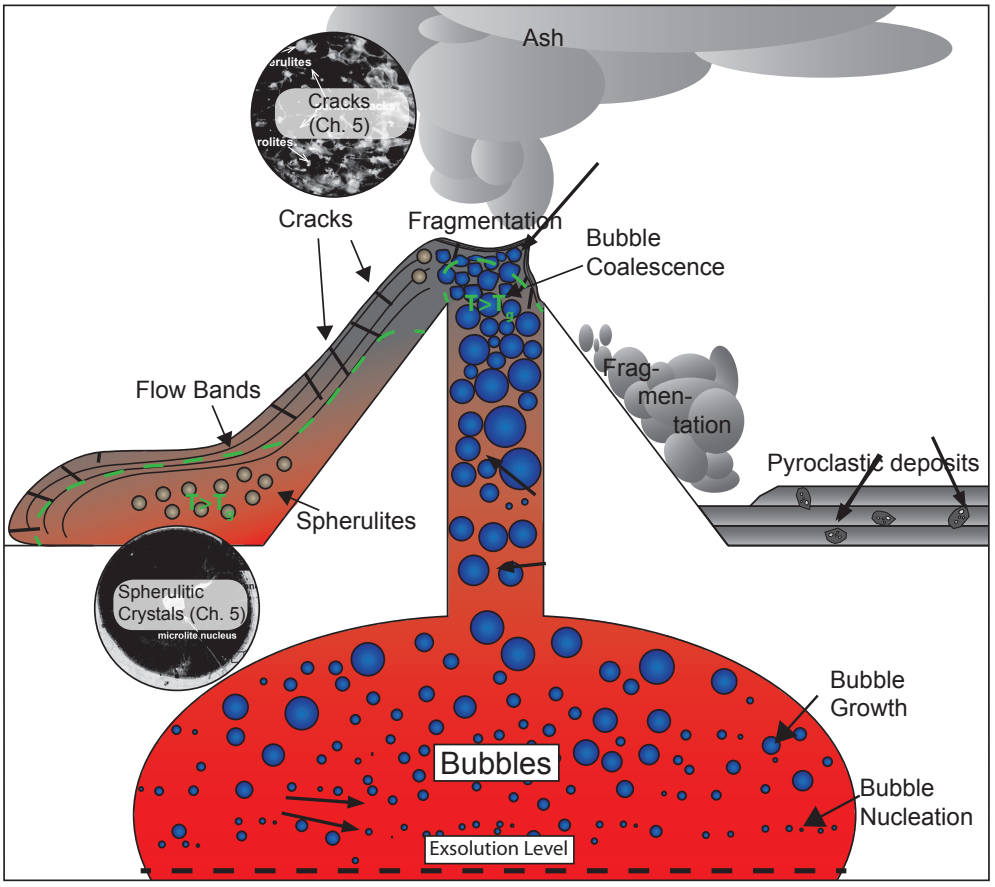

FIGURE 4.6: Overview of textures in Chapter 5

Chapter 5

Timescales of texture development in a cooling lava dome

Crystal growth and crack development in cooling lava domes are both capable of redistributing and mobilizing water. Cracking and hydration decrease the stability of a dome, which may lead to hazards including partial dome collapse and block and ash flows. By examining the distribution of water around crystals and cracks, we identify and confine temperature and timescales of texture development in glassy rocks of volcanic domes. Four generations of textures have been identified: type a: spherulites, type b: cracks associated with spherulite growth, type c: perlitic cracks, and type d: disparate cracks. High–resolution imaging using Fourier transform infrared spectroscopy (FTIR) performed on samples from the Ngongotaha dome, New Zealand, show an increase in H_2O of up to 450 % along gradients of around 100 μm up to 300 μm in length from perlitic cracks, spherulitic cracks and in haloes around spherulites. No gradients in water concentrations across the disparate cracks are present. Water diffusion models show potential timescale-temperature couples that coincide with textural observations and previous studies, and allow us to develop a conceptual model of spherulite growth and cracking in a cooling lava dome. Spherulite growth starts around the glass transition temperature (T_g) when the viscous melt cools to a brittle solid and proceeds with cracking related to volume changes at slightly lower temperatures and shorter timescales (days to weeks) compared to spherulite growth. Perlitic cracking happens at $T \ll T_g$, allowing hydration of a permeable network within weeks to months. Low temperature

($\lesssim$50 °C) cracks could not be hydrated in the time since eruption ($\simeq$230 ka). Our data show that textures in cooling glass develop during cooling below T_g within days, producing cracks and crystals that create inhomogeneities in the spatial distribution of water. The lengthscales of water diffusion away from spherulites, spherulite cracks, and perlite cracks suggest that most of the rehydration of melt/glass occurs at relatively high temperatures (>400 °C). Lack of evidence for water diffusion around other cracks suggests minor low-temperature meteoric water rehydration following emplacement.

5.1 Introduction

Crystallization and crack formation during lava dome cooling increases the likelihood that a lava dome will fail [122]. Crystal formation and cracking of lava can be observed at any volcanic outcrop; however, constraints of timescales and temperatures of these alteration processes are incomplete. Understanding the behavior of cooling magma is crucial for using volcanic textures as a proxy for volcanic processes and for estimating the weakening of volcanic rocks. During cooling of a melt crystals grow and cracks form [36]. The formation of cracks decreases the stability and changes the permeability of volcanic structures such as domes, spines and plugs [80, 109, 122]. The formation of anhydrous crystals rehydrates surrounding glass/melt [e.g. 29, 57, 146, 163, 181], whereas cracks shorten diffusion paths for degassing and act as channels for water to leave the rock [18]. Most studies focus on the degassing of melt [e.g. 18, 32, 63, 124, 163]. Fewer studies discuss the re-hydration of magmatic melts, which can either be just a redistribution of water or an actual increase of the bulk water content of the magma by hydration with meteoric water [54]. Sources of water for redistribution into the melt fraction are collapsing bubbles [e.g. 180, 193] and growing crystals [e.g. 148, 157, 164].

Around the glass transition temperature (T_g), where a viscous melt cools to a brittle glass, supercooled magma allows heterogeneous crystal growth on pre-existing mineral phases [144, 161]. In silicate glasses, crystals tend to grow as branched needles to form spherulites. Spherulites are fibrous, often radial aggregates of anhydrous, branched crystals such as SiO_2 phases and feldspars [102]. During spherulite formation, anhydrous crystal growth enriches the surrounding glass in water, as the water is incompatible in the anhydrous crystal phases [29, 30], resulting in a halo of increased water content [29, 146]. The high volume of exsolved volatiles can lead to the formation of lithophysae (i.e., inflated spherulites [102]) when exsolved volatiles form cavities in the center of the spherulite [161]. Timescales of spherulite growth in rhyolites typically range from a few tenths to hundredths of a millimeter per day at eruptive temperatures from 650 °C to

850 °C [29] and become prohibitively slow at temperatures less than 400 °C [181]. Below T_g, no studies on the possible brittle response of the surrounding glass due to volume changes during crystal growth and water exsolution have been presented.

At surface temperatures diffusion coefficients are too low to allow significant hydration of large volumes of volcanic glass post–eruption. Volcanic glasses with very high water contents of several wt.% are usually perlitic. Perlite is the network of hydrated, arcuate cracks that form during cooling in volcanic glasses [38, 102]. Experiments by Morse et al. [106] indicated that these cracks form due to the volume increase during hydration. Tuffen and Castro [172] show that this may explain perlite development in the products of subglacial eruptions. Another possible explanation for perlitic cracks is thermal cracking during fast cooling, although this is thought to produce more aligned cracks [36]. Depending on solubility and diffusion rates, interconnected cracks that develop from perlites lead to dehydration or hydration of the cooling magma [100, 106]. Spherulites are frequently surrounded by cracks comparable to fracturing resulting from growing bubbles [131]. This radial cracking and the resulting hydration of the surrounding glass have not been previously described in the literature. The dense network of cracks lowers the stability of glassy domes considerably [88].

In order to understand the alteration of volcanic domes during cooling, a better comprehension of common textures in volcanic glass is needed. In this study, we estimate time and temperature ranges of cooling textures by measuring water contents across common textural features of volcanic glass such as spherulitic crystals and perlitic cracks. Fourier transform infrared spectroscopy (FTIR) imaging is utilized to resolve the distribution of dissolved water around a spherulite. High–resolution images of water distribution identify and quantify the redistribution of water in a cooling glass and within a variety of textural features that occur during cooling of a magma. We present a detailed study of the hydration occurring around common magmatic textures and provide estimates of mechanisms, timescales and temperatures that lead to the formation of cracks and crystals in a cooling lava dome.

5.2 Methods

5.2.1 Sample Selection, Characterization and Preparation

Ngongotaha dome is a rhyolitic, peraluminous dome that erupted 230 ka ago [4] as part of the Rotorua caldera formation in the Taupo Volcanic Zone, New Zealand. It consists of several lobes of obsidian of homogeneous chemical composition and low initial crystallinity of <5 % [128]. A sample (Ng-10-7) with low spherulitization and perlitization

with pristine glass was chosen for analysis. X-ray powder diffractometry on a Philips PW1820/1710 of isolated spherulites yielded ≈ 60 wt.% albite and ≈ 40 wt. % cristobalite. X-ray diffraction patterns were collected between 2Θ values of 3° - 70° with a generator current of 50 kV, a generator potential of 40 mA (using Cu Kα radiation) and a scan speed of 0.02° 2Θ/s. Peak areas of each identified phase were measured to estimate relative amounts.

The sample was immersed in epoxy resin at atmospheric pressure in order to prevent further cracking during sample preparation. For FTIR measurements, samples were polished on two parallel surfaces to a thickness of 167 μm using silicon carbide and diamond paste of decreasing grain sizes to 0.25 μm to ensure highly polished surfaces. Ethyl cyanoacrylate (superglue) was used to mount the sample on a glass slide, allowing the second side of the sample to be polished. The superglue was completely removed with acetone to free the samples for analysis. No binding agent was present when the sample was viewed under the microscope.

5.2.2 Calorimetry

The glass transition temperature of 43.05 mg of chips of Ng-10-7 was estimated using a Netzsch Differential Scanning Calorimeter 404 (DSC) similar to Giordano et al. [59]. A sapphire crystal of approximately the same weight as the sample was used for heat capacity calibration and measurements. The specific heat capacity (C_{p}) was measured at a heating rate of 10 °C/min in a N_2-purged furnace. In this study, the temperature at the peak in C_{p} associated with the glass transition measured at 10 °C/min was used to define T_{g}.

5.2.3 Imaging Micro Fourier Transform Infrared Spectroscopy (FTIR)

Infrared absorption spectra were collected on a Varian FTS Stingray 7000 Micro Image Analyser spectrometer and attached UMA 600 microscope at the Institute for Research on Earth Evolution (IFREE), Japan Agency for Marine Earth Science and Technology (JAMSTEC), using a ceramic source and a Ge-coated KBr beamsplitter. The sample was placed on a dry KBr window, which is under N_2-purge along with the interior of the microscope and the spectrometer bench, and the area for analysis was selected using the microscope. The absorbance spectra were recorded using a Varian Inc. Lancer Focal Plane Array (FPA) camera with an infrared photovoltaic MCT array detector housed in the microscope. The FPA camera consists of 64 x 64 channels providing 4096 individual spectra over the spectral range 4000–900 cm^{-1}. The imaged area is 350 x 350 μm resulting in each channel, or spectrum in the image, having a resolution of 5.5 μm. The

detector was cooled with liquid nitrogen and calibrated regularly. Every 200 minutes a background measurement was performed and subtracted from the images. Sample wafer thicknesses were measured using a Mitutoyo micrometer, which can measure within ±1 μm. An average thickness of 167 ±3 μm was measured at 10 spots around the measured area in the samples. Measuring interference fringes in reflectance spectra following the method outlined in Nichols and Wysoczanski [113] and a refractive index for rhyolite of 1.5 [91] yielded a higher standard deviation of up to ±5 μm around a similar median value of 170 μm. Total water contents were quantified using the band of fundamental OH stretching at a wavenumber of 3576 cm^{-1} [159] . The absorbance was taken as the height of the peak above a linear baseline. A density of 2350 kg/m^3 [154] and a molar absorption coefficient of 88 l/mol·cm [46] were used as representative of rhyolite.

5.3 Results and Discussion

In this section, the calorimetric properties and textures of the rhyolitic obsidian (Ng 10-7) are assessed and the order in which textures could have developed during cooling examined. Water distributions in the sample and numerical models of water diffusion are used to constrain the temperatures and timescales of alteration of the volcanic dome.

5.3.1 Calorimetry

The peak of specific heat capacity during initial heating at 10 °C/min defined the glass transition at a temperature of 655 °C . However, the peak height is not large enough for cooling rates to be quantified by relaxation geospeedometry measurements as previously performed on other samples by Gottsmann and Dingwell [64] and Ferk et al. [49] . The model of Giordano et al. [60] predicts T_g to be 657 °C for a melt of the Nongotaha's chemical composition (as given by Richnow [128]) with a total water content of 0.3 wt.% H_2O equivalent to the average water content of the samples.

5.3.2 Textural Descriptions

Typical textures within rocks that outcrop at the Ngongotaha Dome, New Zealand, are shown in Fig. 5.1. Most glassy areas in the dome have arcuate, randomly distributed perlitic cracks, spherulites and microlites. Black areas represent pure glass that grades into gray, highly devitrified areas (Fig. 5.1a). The spherulites are spheres of radially oriented crystals, that grow around nuclei such as microlite crystals of metal oxides or feldspars. The glass surrounding spherulites is both radially and concentrically cracked.

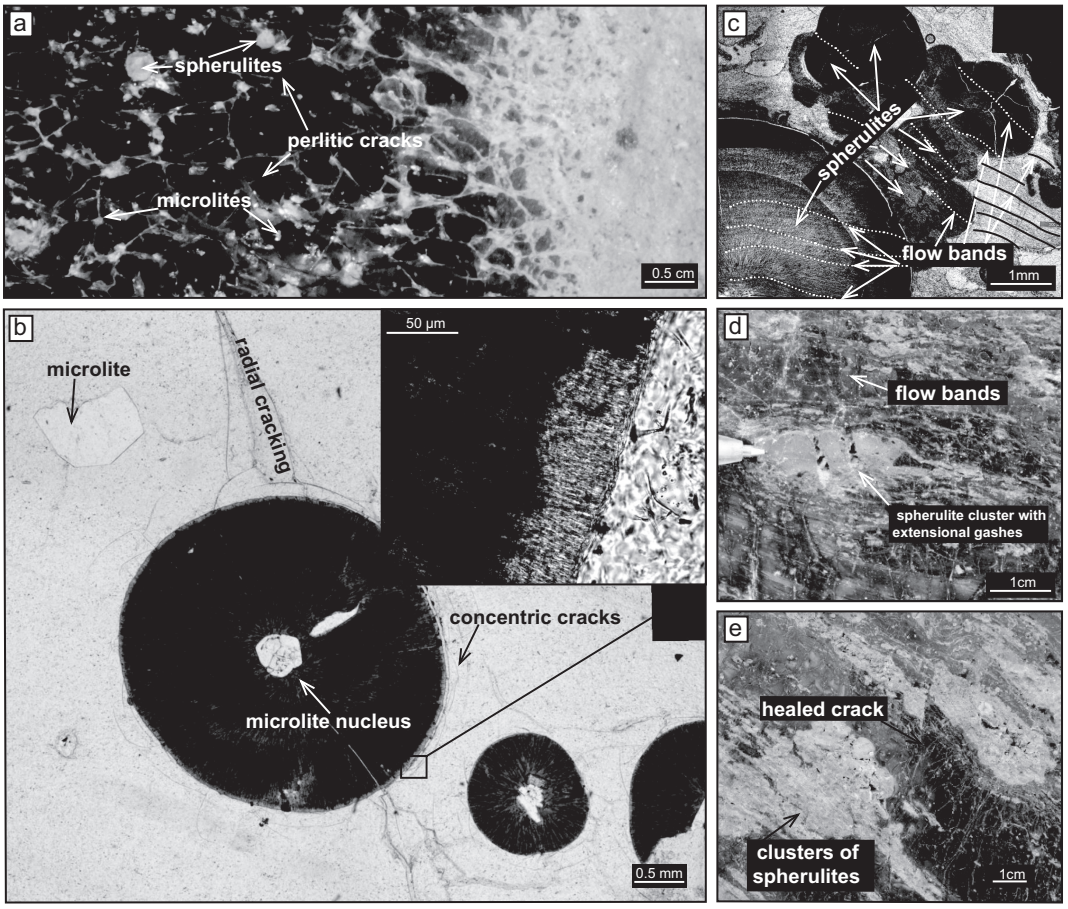

FIGURE 5.1: a: Glass with arcuate perlitic cracks, spherulites and microlites. b: Spherulites present in sample Ng-10-7. c: Typical progressively growing spherulites in more devitrified samples. Some flow bands are deflected by spherulite growth d: A spherulite cluster shows extensional gashes ≈70 ° to the direction of flow banding. e: Macroscopic clusters of spherulites along flow bands are displaced by a healed crack. (All images are from Ngongotaha dome)

In contrast, the glass surrounding microlites is rarely cracked (Fig. 5.1b). In more devitrified areas, spherulites occur in clusters, where smaller spherulites frequently grow in radial patterns around larger spherulites. Flow bands can be traced through the spherulites, although they have been deflected by the growth of the spherulite (Fig. 5.1c). Some spherulite clusters show extensional gashes, perpendicular to the direction of flow banding (Fig. 5.1e). Macroscopic clusters of spherulites are elongate along existing flow bands. Flow bands are lined with variably colored palagonite along with clusters of spherulites. In one case (Fig. 5.1e) the bands are displaced by a fault that appears to have healed. A key observation is that perlitic cracks have not been displaced by this fault.

Both cracks and spherulites can be sources of hydration if the timescales and temperatures allow water to diffuse into the glass. In order to investigate the intricate relationship between spherulites and cracks, a single glassy sample was chosen for detailed FTIR measurements to characterize the distribution of water. This sample (Fig. 5.2) shows cracks and spherulites as well as opaque microlites in otherwise clear glass. No textural features such as microlites or vesicles are present in the analyzed sample to indicate a direction of shearing expressed by flow banding.

The most common textures within this sample are divided into four types by their petrographic appearance (marked a–d in Fig.5.2).

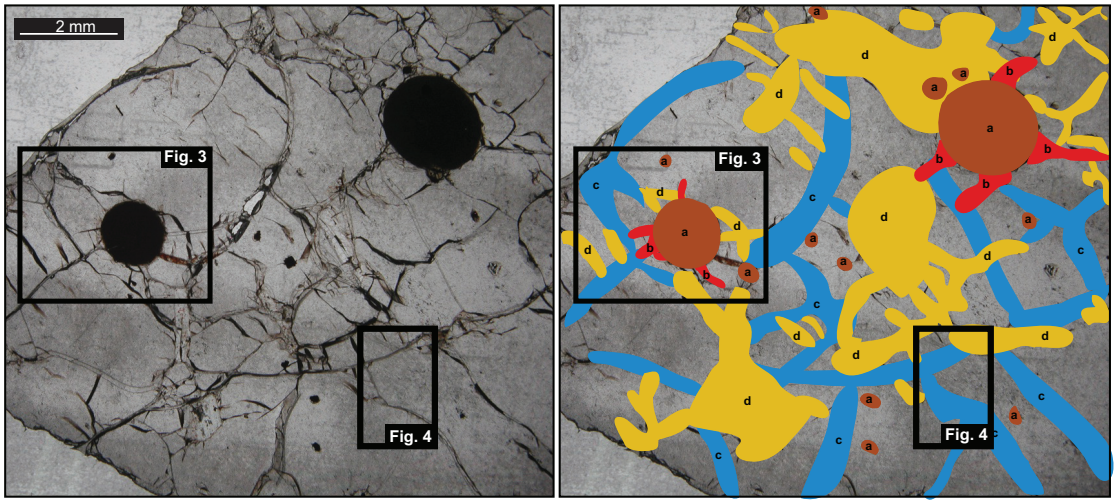

FIGURE 5.2: The different types of texture in the Ngongotaha dome sample: Type a: Spherulites and other crystals (mostly metaloxides) brown. Type b: Radial cracks associated with spherulites red. Type c: network of cracks blue. Type d: individual cracks without any association yellow.

Type a: Spherulites: 5-10 vol.% of this sample consist of spherulites, which accounts for most of the overall crystallinity of the rock. The spherulites are typically ≈2 ±1 mm in diameter. The spherulites are distributed heterogeneously in this sample and are not clustered or aligned.

Type b: Thin cracks (≤1 μm wide) of usually a few hundred micrometers in length radiate from the spherulites.

Type c: Slightly curved cracks that form a network over the whole thin section and are broader and longer than type b and type d cracks. These curved cracks do not cross spherulites and terminate at spherulite rims. Additionally, they do not appear to be diverted by spherulites and end roughly perpendicular to spherulite surfaces.

Type d: Sharp and disparate cracks are randomly oriented and typically ≈1 mm long.

5.3.3 Textural constraints on timing of crack formation

Textures preserved in the glassy samples from Ngongotaha dome provide information about the processes and the order of events during cooling of a volcanic dome. The crack displacing spherulites and flow bands in Fig. 5.1 shows that high temperatures (close to T_g) existed after spherulite growth due to crack healing. In addition, T_g could have been crossed multiple times by elevated strain rates at temperatures greater than the calorimetric T_g [44, 174].

The displacement of flow bands by spherulites indicates that the spherulites began growing at $T > T_g$. The brittle nature of the type b fractures around the spherulite indicates that $T < T_g$ may have existed towards the end of spherulite growth. Circular cracks, parallel to the surface of spherulites, resulted from a pressure imbalance associated either with volume reduction caused by spherulites replacing the glass or from a difference in the thermal expansion coefficient present between glass and crystals. Concentric and radial fractures are related to volume changes associated with crystal growth, hydration, and volatile exsolution.

Type c cracks are randomly distributed throughout the sample. Generally, these cracks do not cross–cut spherulites but terminate at the surface of the spherulite. Reasons for this include that the crack stopped at the spherulite margin or that these cracks joined up with preexisting radial cracks of type b that surround the spherulites. Regardless, this supports the hypothesis that the cracks of type c were formed after the spherulites and after the formation of cracks of type b (i.e., at lower temperatures). The arcuate shape and the hydration and the homogeneous anisotropic distribution of type c cracks throughout the rock fit the definition of perlitic cracks [102]. To further confine timescales and temperatures of formation of these textures, they were targeted for FTIR measurements.

5.3.4 FTIR Results

An overview of the total water concentrations in sample Ng-10-7 is shown in Figs. 5.3 and 5.4. Each color map shows the distribution of total water over an area of 350 x 350 μm. Warmer colors indicate higher water contents. This immediately shows a redistribution of water around the textural features. Water concentrations are as low as 0.2 wt.% in unaffected areas of glass and reach $\approx$ 0.9 wt.% close to the spherulites and around the cracks of types b and c. The water contents decrease to the low values over distances typically of about 100 μm (see Fig. 5.3). This considers only hydrated margins with symmetric diffusion profiles due to the cracks being aligned parallel to the

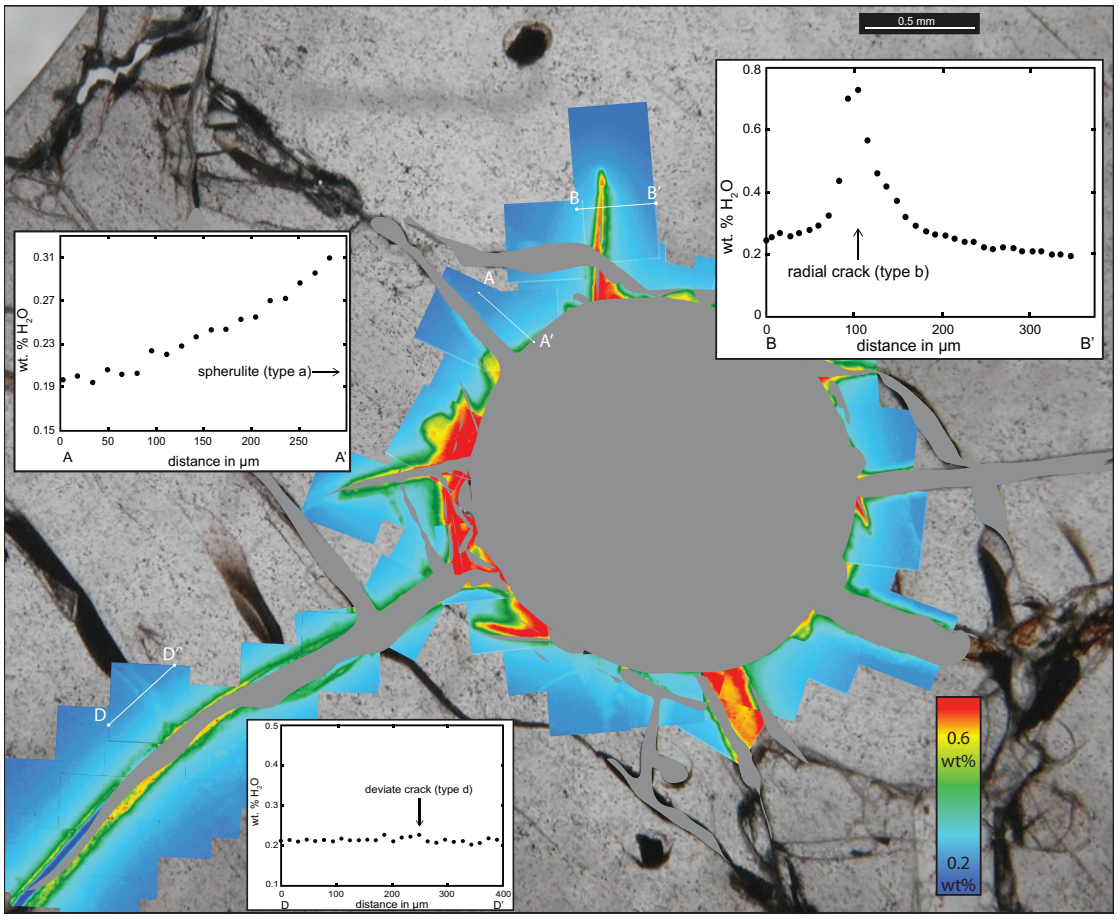

FIGURE 5.3: Overview of water distribution around a spherulite in sample Ng-10-7. Colors represent the amount of total H_2O, with higher water contents drawn in warmer colors. Cracks and spherulites have been masked gray.

beam path. Water contents in areas of resin filled cracks and areas of alteration are masked out in Figs. 5.3 and 5.4.

5.3.5 Water Diffusion

The distribution of water around (a) the spherulite, (b) the spherulitic cracks and (c) the arcuate cracks follows similar patterns, suggesting that hydration was caused by similar mechanisms. Water concentration around the type c arcuate cracks shows a gradient, indicating that hydration occurred after the crack formed. This is contrary to hydration being the reason for development of perlitic cracks as outlined by Morse et al. [106] and Friedman et al. [54] but rather is a result of the cracking. Type d cracks do not have any water enrichment associated with them. This suggests that they formed at a very low temperature at which diffusion rates would be sufficiently low to prohibit any water from entering the glass after formation. The high contrast, the sharp edges, the lack of

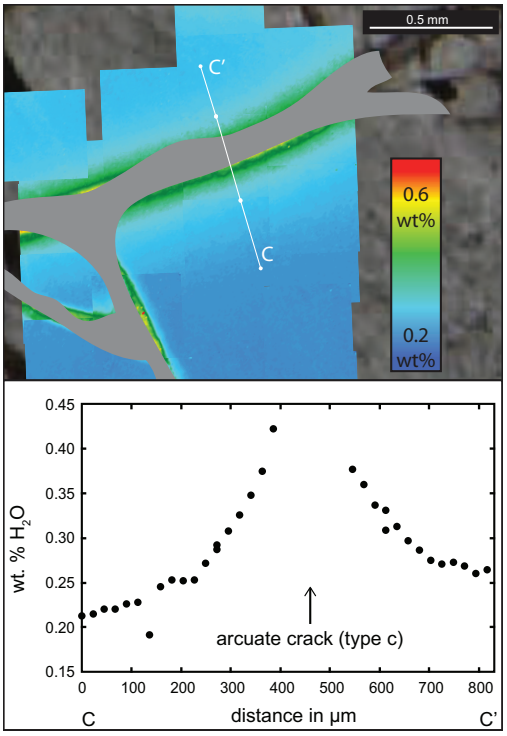

FIGURE 5.4: Distribution of water around a crack of type c. The asymmetry is interpreted as due to the crack not being perfectly straight and perpendicular to the surface of the measured wafer.

any evidence for crack healing and the short lengths of the cracks indicate brittle failure at low temperatures.

Spherulite growth is estimated to start at a minimum undercooling of ΔT = 150 °C; spherulites of the type found in the Ngongotaha dome rhyolite are produced at ΔT = 245–395 °C [48]. For a liquidus of 1000 °C (calculated using MELTS [58], rhyolite composition and bulk water content at atmospheric pressure) undercooling by ΔT corresponds to temperatures of 850 °C and 765–605 °C, respectively. Watkins et al. [181] suggested 400 °C to be the lower limit of spherulite growth within reasonable timescales.

Spherulite growth rates range between 0.25 nm/s and 4 nm/s [29]. For the spherulite in Fig. 3 (diameter of about 900 μm), this would mean that the spherulites grew over timescales of 62.5 h to 1000 h. Cooling rates at T_g in rhyolitic flow features are estimated to be 0.001 to 10 °C/min in settings with sub–surface conductive heat loss [e.g 49, 64]. Under these conditions the glass would have cooled from an eruptive temperature of 815 °C [128] to 400 °C in ≈45 min to ≈325 days, assuming Newtonian cooling at ambient temperatures of 10 °C. The spatial association between spherulites and type b cracks and the similar width of diffusion distance of water species indicate that spherulites and type b cracks formed concurrently under similar conditions. We have shown that spherulites started growing above T_g (≈655 °C), as the flow banding is deflected and

cracks that are offsetting the spherulitic bands have rehealed. The open, radial cracks of type b that surround spherulites are formed during spherulite growth, due to the brittle and sub-T_g behavior of the glass.

With these observational temperature and timescale constraints, we can model diffusion profiles for the water distributions found in sample Ng–10–7. The model assumes atmospheric pressure (10^5 Pa), as the samples were collected near the surface of the dome. A simple solution of Fick's second law of diffusion was used according to Tomozawa and Davis [167]. Both ends of the model domain have fixed water concentrations as boundary conditions. This model is best suited to compare the temperatures and timescales of different features of hydration. According to Zhang and Ni [196], a complementary error function (erfc) is sufficient to be used as a solution as shown in the equation:

$$C(x) = C_b erfc(\frac{x}{2\sqrt{Dt}}) \tag{5.1}$$

with C as the concentration, C_b as the boundary concentration (both in kg/kg and normalized to the far field concentration), x as the distance (in m), t as the timescale (in s). The diffusivity of water in peraluminous rhyolite glasses (m^2/s) was calculated according to Zhang and Ni [196] as:

$$D_{H_2O_t}^{rhyolite} = C_b exp(-18.1 + 1.888P - \frac{9699 + 3626P}{T}) \tag{5.2}$$

where T is temperature in K, P is pressure (GPa), in this case atmospheric pressure (10^5 Pa = 10^{-4} GPa), and C_b is the boundary concentration of total H_2O (H_2O_t) in wt.% ($C_w = 1$ for H_2O_t of 1 wt.%). Diffusivity changes due to concentration differences along the profile were neglected and fixed at the maximum level of the boundary. Despite this model not accounting for geometrical effects (e.g. growth of the spherulite and spherical diffusion; see also Castro et al. [29], Hesse [69] and Watkins et al. [181] for alternative models), our data fits reasonably well for a range of $t - T$ conditions (Fig. 5.5) and produces similar length scales as the model by Hesse [69] for the growth rates given by Castro et al. [29]. Time-temperature pairs with a good agreement could be found for each set of data (Fig. 5.6). This shows that the conditions for hydration are at elevated temperatures (well above ambient temperatures of 10 °C).

The conditions for hydration related to spherulite growth in the model lie within the timescales and temperatures discussed earlier, assuming spherulite growth at an average temperature of ≈600 °C (suggesting the onset of hydration at $T \gtrapprox T_g$) and occuring over 3–5 days. For spherulites, this temperature range probably starts at 765 °C$> T > T_g$; however, we can assume sub–T_g hydration for low strain rate volume change–driven cracks. Geometrical effects during growth of the spherulites were not taken into account

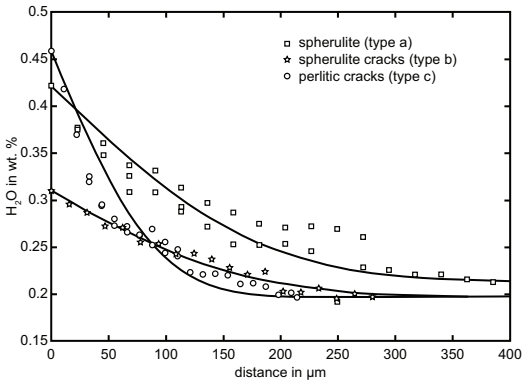

FIGURE 5.5: Water distribution around spherulite rims (squares), radial cracks around spherulites (stars) and perlitic cracks (circles). An example of diffusion models is given for each set of data, corresponding to: type a: 480 h at 475 °C or 100 h at 580 °C for spherulites; type b: 400 h at 400 °C or 1200 h at 350 °C for spherulitic cracks; type c: 650 h at 450 °C or 5500 h at 350 °C. Data sets are shown in relation to distance from crack (in both directions for types b and c).

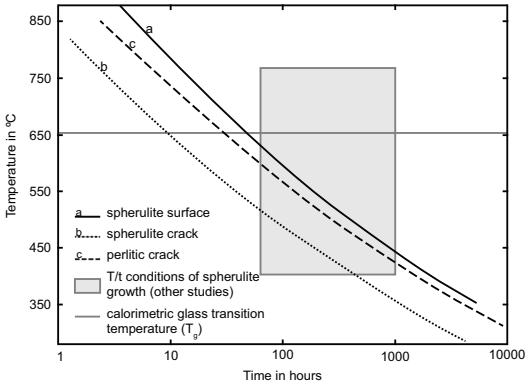

FIGURE 5.6: Diffusion models for different T/t conditions that fit water distribution in measured data, $T-t$ conditions for spherulite growth in other studies and the calorimetric T_{g} at a heating rate of 10 °C/min. Although overall timescales and temperatures could vary, the lengthscales of diffusion away from cracks suggest that perlitic cracks formed when the magma was roughly 50 °C cooler than when spherulite cracks formed.

and the diffusion was assumed to start instantly after growth; therefore, the timescales are a minimum estimate. The amount of diffused water is less than the water content of the crystallized melt. Hence, this is most likely a redistribution of magmatic water rather than post–eruptive hydration by meteoric water.

Spherulitic radial cracks (type b) fit lower temperature ranges at the timescale of spherulite growth. This represents a delay in the onset of cracking and hydration towards the end of spherulite growth and/or a limited time where the required water and temperature are available. This agrees with textural observations, as these cracks have a limited water supply related to the growth of spherulites and must have opened after T_{g} was crossed but while spherulite growth was still proceeding and there was still a source of water available. The hydration along perlitic cracks (type c) fits a wide range of conditions for diffusion; however, perlitic cracks do not intersect spherulites, but rather

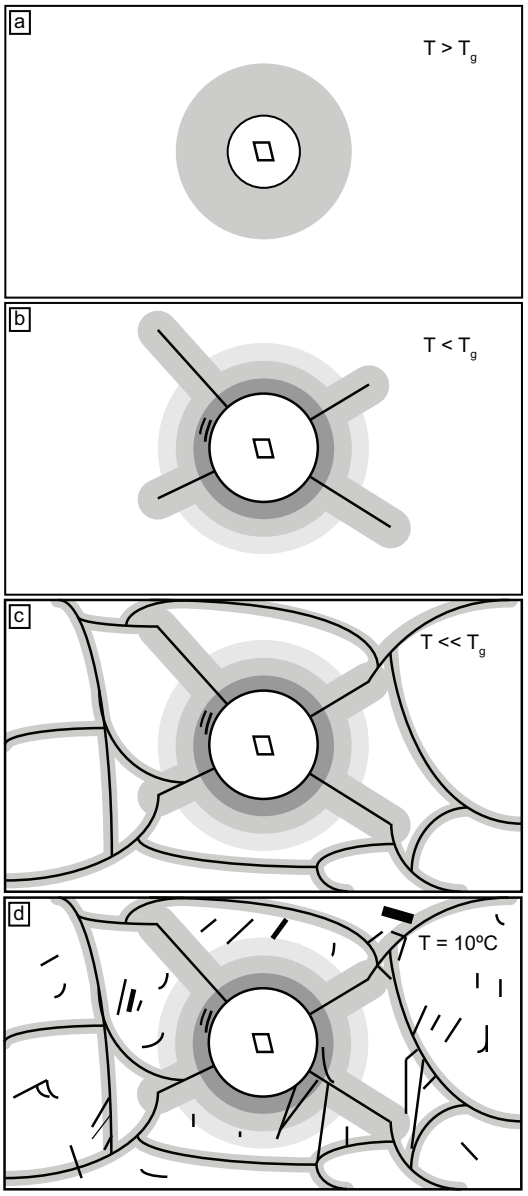

FIGURE 5.7: Model of alteration in a cooling lava dome. Grey areas have locally increased water contents and cracks are drawn as black lines. The scale of the frame is in the range of millimeters. a: A spherulite forms around a microlite nucleus (shown as diamond at center of spherulite) and results in a hydration halo. b: Radial and concentric cracks form around the spherulite; water travels along the radial cracks and diffuses into the surrounding glass. c: Perlitic cracks form and allow circulation of water (and therefore further hydration) at much lower temperatures. d: Cracks form at ambient temperatures that are not hydrated.

they merge with the spherulitic cracks. This shows that pelitization must have occurred after spherulite related cracking. Average temperatures around 450 °C for ≈650 h are consistent with the diffusion profiles measured (Fig. 5.6). On the other hand, quenching due to the down flow of meteoric water and slower cooling with hydration at higher temperatures is also plausible.

5.4 Implications for a cooling lava dome

Common textural features in magma are formed in late stages of cooling. In this case study, spherulitic, anhydrous minerals formed first (Fig. 5.7a), producing cracks that acted as channels for water to be redistributed during crystal growth (Fig. 5.7b). At lower temperatures, perlitic cracks formed allowing water (from meteoric and/or magmatic sources) to flux through the dome (Fig. 5.7c). At ambient temperatures (10 °C average), additional cracks opened that were not subsequently hydrated due to the low temperatures (Fig. 5.7d). We conclude that hydration occurred only at temperatures between T_g and roughly ≈400 °C over timescales of days to months. Temperatures and timescales of hydration around these textural features depend largely on individual cooling rates and chemical compositions as well as crystal and bubble contents. However, we demonstrate that local changes in hydration and textures occur soon after effusive eruption of fresh lava. This has significant implications for the stability and permeability of lava domes, considering the formation of cracks weakens the brittle parts of domes, and therefore may initiate dome collapses and block and ash flows. Cracks produced during cooling of a lava dome can also act as pathways for degassing of freshly introduced magma. This could possibly overcome glassy barriers of low permeability in volcanic plugs [79, 109, 133, 188].

Chapter 6

Conclusions

Water distribution in volcanic rocks is heterogeneous, showing microscopic gradients of hydration and dehydration across all common volcanic textures (Fig. 6.1). This study shows, that water distribution patterns are a powerful tool to discriminate textural features and confine their thermal and temporal evolution. By employing high resolution Fourier transform infrared spectroscopic techniques on natural and experimentally altered rocks in combination with textural studies, a conceptual model of the texture formation during many stages of volcanic eruptions was developed (Fig. 6.1).

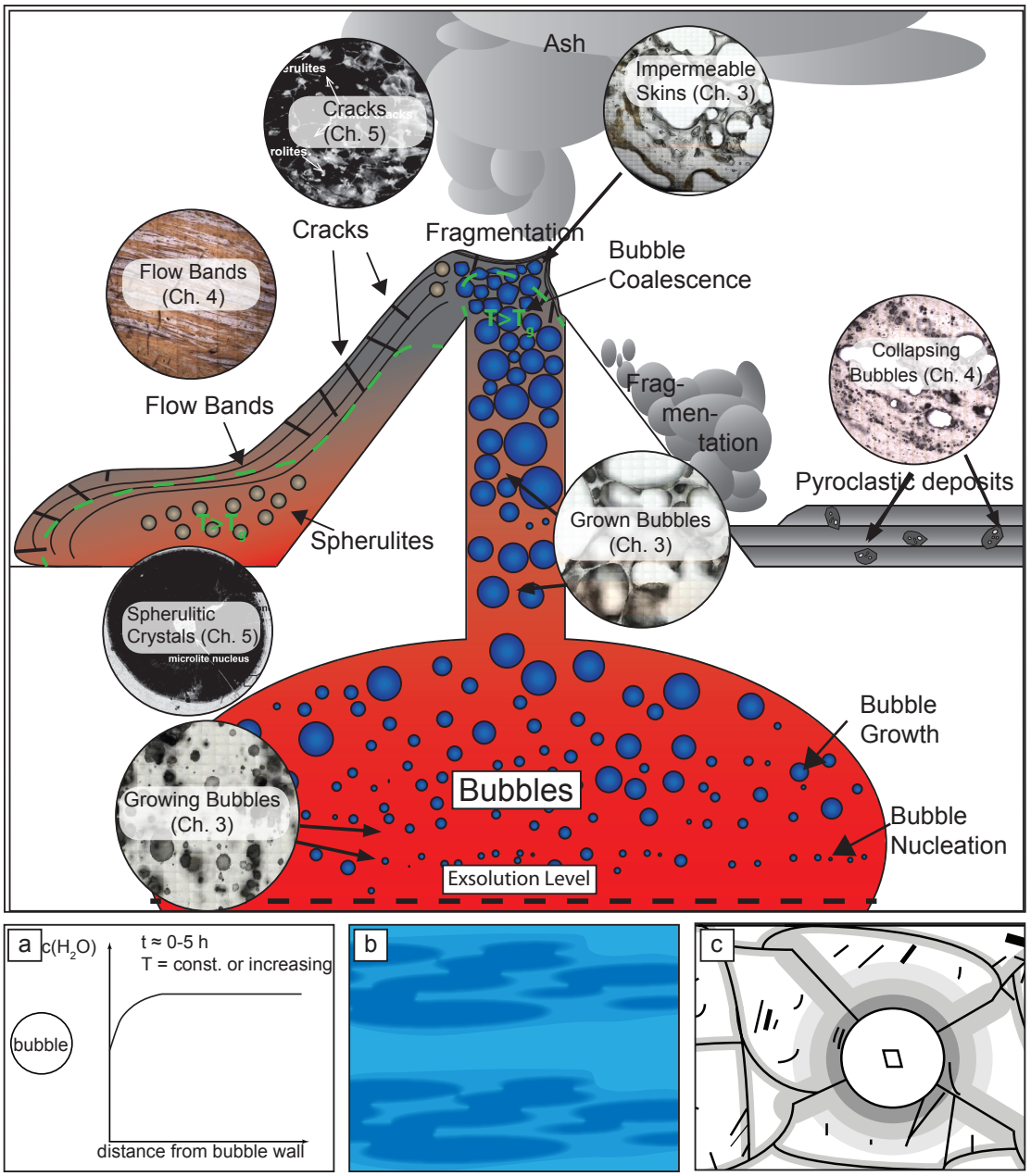

FIGURE 6.1: Common textures in magma evolve during ascent, eruption and emplacement. The formation of bubbles, flow bands, crystals and cracks occurs over wide ranges of temperatures and is associated by water redistribution. Numerical and conceptual models of water redistribution based on high-resolution FTIR analyses, as well as textural analysis could show the processes, temperature and timescales during evolution of textures in a cooling magma. Key-points are: a: Water diffusion profiles preserve temperature regimes of bubble formation and collapse until equilibration. b: Water resorption due to the retrograde solubility of water could lead to bubble collapse and the formation of flow bands. c: Textures in a cooling lava dome form within hours to months at temperatures slightly above the glass transition to ambient temperatures.

Bubble formation usually marks the onset of water oversaturation during magma rise in volcanic eruptions (Fig. 6.1). If bubbles are quenched while still growing through diffusion of water, a dehydration rim can be observed around most of the vesicles, preserving water diffusion profiles that can be modeled with diffusion modeling at fixed boundary conditions (3). Similar water distributions may be observed around bubbles in pyroclastic material that was erupted right after bubble growth and was not hydrated post-eruption [180]. If the melt stagnates unquenched, water exsolution rims will be equilibrated in timescales of days (Chapter 3), depending on diffusivities, viscosities and extent of gradients. This is commonly the case for medium volumes of magmatic foams, which experience long timescales at viscosities that allow for diffusion e.g. in lava domes and plugs or in large lava flows and pyroclastic flow deposits (Chapter 3 and 4). If, however, the temperature of the magma/lava decreases before equilibration as a relaxed melt, water increases may be observed around the bubbles. Therefore, rocks that do show increases of water around otherwise isolated bubbles, have a complex, non-monotonic thermal history. This could e.g. be used to determine whether an erupted rock was ejected after initial bubble growth, or whether its ascent was involving stages of short–term stagnation. Collapsing of foams is dominated by degassing through a permeable network [21]. However, permeable networks can be sealed by formation of bubble free melt that preferentially forms on surfaces due to collapse of bubbles (3), while dehydrating further through diffusion. Shearing of melt further increases permeabilities [19, 118] by creating degassing pathways through connecting and stretching vesicles in foams. The breaking of a degassed sealed surface layer could be an additional important result of structural shearing and fracturing of volcanic foams, and result in large jumps in permeability.

Completely bubble free rhyolite melts are rare, as outgassing through a bubble network is limited at low porosities and bubble movement in a high viscosity melts is slow in cooling magma. The rare cases of bubble free glass therefore have to be explained by shear driven outgassing during flow band formation and re-sorption of small bubbles (Fig. 6.1, Chapter 4). I can show that some natural samples show signs of bubble collapse due to water re-sorption (Chapter 4). Water heterogeneities could also be observed across flow banding in otherwise bubble free melt. These heterogeneities are due to layering of differently dehydrated rocks formed by the remnants of late re-sorption and outgassing of water into the surrounding melt.

Flow banding can also be present as heterogeneous distributions of crystals. These crystals are often the result of late stage crystal growth below solidus temperatures. In special circumstances of high viscosities and ideal cooling rates, the crystals grow radially as spherulites (Fig. 6.1). It could be shown that spherulites start growing at temperatures above the glass transition, i.e. in a melt. However, we have evidence for

continuing growth once the melt becomes a glass. As the anhydrous crystal grows water that was dissolved in the melt or glass is redistributed into haloes of water around the crystals. Cracks around the crystals that form because of volume changes associated with the crystal growth are hydrated with magmatic water (Fig. 6.1). At lower temperatures a connected network of arcuate (perlitic) cracks may form. This network is also hydrated, however independently from crystal growth and at longer timescales. This could possibly be explained by fracturing due to thermal stress and the successive hydration by meteoric water, as the lava cools further. More cracks may form at ambient temperatures, however, timescales of hydration are prohibitively long to allow for comparable hydration rims from lavas from recent volcanic eruptions.

The textures of volcanic rocks provide a window into eruptive processes. High-resolution water profiles in volcanic rocks can help to confine timescales and temperatures of their formation. Qualitative and quantitative evaluation of the distribution and length-scales of water heterogeneities in rhyolitic rocks can help to create important conceptual models of eruption processes. This could be used as a tool to identify the thermal history and evolution of volcanic rocks for a better understanding of volcanic eruptions.

Question	What answer could be provided?	
1. What technique is best suited for quantitative water analysis at high spatial resolution?	FTIR is at the moment the most reliable, readily available technique. Synchrotron light sources an FPA detectors open new possibilities in terms of spatial resolution and mapping techniques.	Chapter 2
2. What is the best way to prepare fragile samples of vesicular, cracked and fragile glass?	Sample preparation techniques and methods during analysis depend highly on the properties of each individual sample. An overview of techniques in Chapter 2 will help to assess the challenges of measurements at the diffraction limit of resolution.	
3. What are typical water distribution patterns around bubbles and can they be used as a proxy for volcanic processes?	There are at least different patterns of water distribution around the bubbles: increases, decreases and homogeneous distribution. These can be associated with distinct cooling/bubble growth histories for the samples of this study.	Chapter 3
4. Is bubble resorption due to cooling possible and what is the impact on volume and water distribution of volcanic rocks?	Bubble resorption is possible, however, a volumetric effect of the resorption could not conclusively be detected. In other scenarios (sheared bubbles) this could however prove to be an important process of bubble collapse in highly viscous magmas.	
3. What are typical timescales of isobaric bubble growth and could this be measured in natural samples?	The timescales associated with the water distribution patterns range between 2 h - 24h. However, temperatures are slightly higher than typical eruptive temperatures.	
5. Are there water heterogeneities associated to flow bands?	Yes, I could detect a slight increase of water across a flow band.	Chapter 4
6. What are flow bands and how do they form?	One possible mechanism of flow band formation is the collapse of a foam and the heterogeneous resorption of water due to localized shearing within the melt.	
7. Could flow banding be associated to the collapse of magmatic foams?	Water increases could be found in resorbing bubbles in a natural melt. However, this only states one possiblity for the creation of water heterogeneities in flow bands and heterogeneous devolatization is equally possible.	
8. At what temperatures do spherulites form and do they form below the glass transition?	Spherulites form above the glass transition temperature, however, the samples in this study show contiuing growth below Tg.	Chapter 5
9. How do Spherulites relate to other textures in volcanic domes in terms of temperature, timescales and formation processes?	Spherulites form cracks during their growth, that are later being matched by spherulitic cracking. The relations between the generations of cracks can be used to determine the order of formation.	
10. Have all cracks found in volcanic glass formed at the same time and temperature?	No, water distribution patterns and textural relations show at least 3 generations of cracks: spherulitic cracks, perlitic cracks and low-T (ambient temperature) cracking.	
11. What are possible processes that lead to cracking in magma?	Crystal growth, thermal stressing and brittle deformation are the three processes that presumably lead to cracking in the samples studied.	
12. What are perlitic cracks, how do they form and at what temperature range and timescales.	Perlitic cracks are an open network that forms at low temperatures (~400ºC) and are hydrated over the course of days to months, possibly by meteoric water.	

TABLE 6.1: Statements to the aim of this study.

Appendix A

Digital Appendix

The digital appendix contains the following files:

- The folder *FTIR maps* contains .pdf files of FTIR absorption peaks of water in the near IR. These were measured at the Australian Synchrotron. All diagrams and maps show absorbances rather than water distribution. The sample names refer to BL - Ben Lomond, Ng - Ngongotaha, MI- Mayor Island, LGM - Little Glass Mountain.
- The file BL24.wmv is a time-lapse video file of a heating experiment on a sample from Ben Lomond. Temperature was 950 °C, total time were 24 h. The real time of the experiment is shown in the top left corner in hh:mm:ss.

Bibliography

[1] SW Anderson and JH Fink. Hydrogen-isotope evidence for extrusion mechanisms of the Mount St Helens lava dome. *Nature*, 341, 1989. URL `http://www.nature.com/nature/journal/v341/n6242/abs/341521a0.html`.

[2] L. M. Anovitz, D. R. Cole, and M. Fayek. Mechanisms of rhyolitic glass hydration below the glass transition. *American Mineralogist*, 93(7):1166–1178, July 2008. ISSN 0003-004X. doi: 10.2138/am.2008.2516. URL `http://ammin.geoscienceworld.org/cgi/doi/10.2138/am.2008.2516`.

[3] L. J. Applegarth, H. Tuffen, M. R. James, H. Pinkerton, and K. V. Cashman. Direct observations of degassing-induced crystallization in basalts. *Geology*, 41 (2):243–246, December 2012. ISSN 0091-7613. doi: 10.1130/G33641.1. URL `http://geology.gsapubs.org/cgi/doi/10.1130/G33641.1`.

[4] PA Ashwell, B. M. Kennedy, D.M. Gravley, Jim W Cole, and Felix W. von Aulock. Insights into caldera and regional structures and magma body distribution from lava domes at Rotorua Caldera, New Zealand. *Journal of Volcanology and Geothermal Research*, submitted, 2012.

[5] P.A. Ashwell, J.W. Cole, B. M. Kennedy, D.M. Gravley, and F.W. von Aulock. Insights into caldera and regional structures and magma body distribution from lava domes at Rotorua Caldera, New Zealand. *Journal of Volcanology and Geothermal Research*, Accepted, 2013.

[6] N Bagdassarov, A. Dorfman, and Donald B. Dingwell. Effect of alkalis, phosphorus, and water on the surface tension of haplogranite melt. *American Mineralogist*, 85:33–40, 2000. URL `http://www.intl-ammin.geoscienceworld.org/content/85/1/33.short`.

[7] NS Bagdassarov, Donald B. Dingwell, and MC Wilding. Rhyolite magma degassing: an experimental study of melt vesiculation. *Bulletin of volcanology*, 57:587–601, 1996. URL `http://www.springerlink.com/index/FYL0X0VTBKUL4DQ0.pdf`.

[8] Liping Bai, Don R Baker, and Mark Rivers. Experimental study of bubble growth in Stromboli basalt melts at 1 atm. *Earth and Planetary Science Letters*, 267:533 – 547, 2008. doi: 10.1016/j.epsl.2007.11.063.

[9] Don R Baker, P Lang, G Robert, J Bergevin, E Allard, and L Bai. Bubble growth in slightly supersaturated albite melt at constant pressure. *Geochimica et Cosmochimica Acta*, 70(7):1821–1838, 2006. ISSN 00167037. doi: 10.1016/j.gca.2006.01.011. URL `http://linkinghub.elsevier.com/retrieve/pii/S0016703706000421`.

[10] Don R Baker, L. Mancini, M. Polacci, M.D. Higgins, G.a.R. Gualda, R.J. Hill, and M.L. Rivers. An introduction to the application of X-ray microtomography to the three-dimensional study of igneous rocks. *Lithos*, 148:262–276, September 2012. ISSN 00244937. doi: 10.1016/j.lithos.2012.06.008. URL `http://linkinghub.elsevier.com/retrieve/pii/S0024493712002319`.

[11] Harald Behrens. Near-infrared spectroscopic determination of water species in glasses of the system MAlSi3O8 (M = Li, Na, K) : an interlaboratory study. *Chemical Geology*, 128(1-4):41–63, June 1996. ISSN 00092541. doi: 10.1016/0009-2541(95)00162-X. URL `http://linkinghub.elsevier.com/retrieve/pii/000925419500162X`.

[12] Harald Behrens, N Tamic, and François Holtz. Determination of the molar absorption coefficient for the infrared absorption band of CO2 in rhyolitic glasses. *American Mineralogist*, 5:5–10, 2004. URL `http://ammin.geoscienceworld.org/content/89/2-3/301.short`.

[13] Harald Behrens, J Roux, D Neuville, and M Siemann. Quantification of dissolved H2O in silicate glasses using confocal microRaman spectroscopy. *Chemical Geology*, 229(1-3):96–112, May 2006. ISSN 00092541. doi: 10.1016/j.chemgeo.2006.01.014. URL `http://linkinghub.elsevier.com/retrieve/pii/S0009254106000544`.

[14] J D Blower, J P Keating, H M Mader, and J C Phillips. The evolution of bubble size distributions in volcanic eruptions. *Journal of Volcanology and Geothermal Research*, 120:1–23, 2002.

[15] M. J. Branney and R. S. J. Sparks. Fiamme formed by diagenesis and burial-compaction in soils and subaqeuous sediments. *Journal of the Geological Society*, 147(6):919–922, December 1990. ISSN 0016-7649. doi: 10.1144/gsjgs.147.6.0919. URL `http://jgs.lyellcollection.org/cgi/doi/10.1144/gsjgs.147.6.0919`.

[16] Hélène Bureau, Caroline Raepsaet, Hicham Khodja, Anna Carraro, and Cyril Aubaud. Determination of hydrogen content in geological samples using elastic recoil detection analysis (ERDA). *Geochimica et Cosmochimica Acta*, 73(11):3311–3322, June 2009. ISSN 00167037. doi: 10.1016/j.gca.2009.03.009. URL `http://linkinghub.elsevier.com/retrieve/pii/S0016703709001513`.

[17] Alain Burgisser and James E. Gardner. Experimental constraints on degassing and permeability in volcanic conduit flow. *Bulletin of Volcanology*, 67(1):42–56, May 2004. ISSN 0258-8900. doi: 10.1007/s00445-004-0359-5. URL `http://www.springerlink.com/index/10.1007/s00445-004-0359-5`.

[18] A. Cabrera, R. F. Weinberg, H. M. N. Wright, S. Zlotnik, and Ray Cas. Melt fracturing and healing: A mechanism for degassing and origin of silicic obsidian. *Geology*, 39(1):67–70, December 2010. ISSN 0091-7613. doi: 10.1130/G31355.1. URL `http://geology.gsapubs.org/cgi/doi/10.1130/G31355.1`.

[19] Luca Caricchi, Anne Pommier, Mattia Pistone, Jonathan M. Castro, Alain Burgisser, and Diego Perugini. Strain-induced magma degassing: insights from simple-shear experiments on bubble bearing melts. *Bulletin of Volcanology*, April 2011. ISSN 0258-8900. doi: 10.1007/s00445-011-0471-2. URL `http://www.springerlink.com/index/10.1007/s00445-011-0471-2`.

[20] Katharine V. Cashman and R. S. J. Sparks. How volcanoes work: A 25 year perspective. *Geological Society of America Bulletin*, (X):1–27, January 2013. ISSN 0016-7606. doi: 10.1130/B30720.1. URL `http://gsabulletin.gsapubs.org/cgi/doi/10.1130/B30720.1`.

[21] Katharine V. Cashman, M. T. Mangan, and S Newman. Surface degassing and modifications to vesicle size distributions in active basalt flows. *Journal of volcanology and geothermal research*, 61(1-2):45–68, 1994. URL `http://cat.inist.fr/?aModele=afficheN&cpsidt=4116452`.

[22] Katharine V. Cashman, B Sturtevant, Paolo Papale, and Oded Navon. Magmatic fragmentation. *Encyclopedia of volcanoes*, pages 421–430, 2000. URL `http://scholar.google.com/scholar?hl=en&btnG=Search&q=intitle:Magmatic+Fragmentation#0`.

[23] Jonathan M. Castro. Constraints on rheology of obsidian lavas based on mesoscopic folds. *Journal of Structural Geology*, 21, 1999. URL `http://linkinghub.elsevier.com/retrieve/pii/S019181419900070X`.

[24] Jonathan M. Castro. Microlite textures and volatile contents of obsidian from the Inyo volcanic chain, California. *Geophysical Research Letters*, 31(18):5–8, 2004.

ISSN 0094-8276. doi: 10.1029/2004GL020489. URL http://www.agu.org/pubs/crossref/2004/2004GL020489.shtml.

[25] Jonathan M. Castro and Donald B. Dingwell. Rapid ascent of rhyolitic magma at Chaitén volcano, Chile. *Nature*, 461(7265):780–3, 2009. ISSN 1476-4687. doi: 10.1038/nature08458. URL http://www.ncbi.nlm.nih.gov/pubmed/19812671.

[26] Jonathan M. Castro, Michael Manga, and Katharine V. Cashman. Dynamics of obsidian flows inferred from microstructures: insights from microlite preferred orientations. *Earth and Planetary Science Letters*, 199(1-2):211–226, May 2002. ISSN 0012821X. doi: 10.1016/S0012-821X(02)00559-9. URL http://linkinghub.elsevier.com/retrieve/pii/S0012821X02005599.

[27] Jonathan M. Castro, Donald B. Dingwell, Alexander R L Nichols, and James E. Gardner. New insights on the origin of flow bands in obsidian. *Geological Society of America Special Paper*, 396(05):55–65, 2005. doi: 10.1130/2005.2396(05).

[28] Jonathan M. Castro, Michael Manga, and Michael C. Martin. Vesiculation rates of obsidian domes inferred from H 2 O concentration profiles. *Geophysical Research Letters*, 32(21):1–5, 2005. ISSN 0094-8276. doi: 10.1029/2005GL024029. URL http://www.agu.org/pubs/crossref/2005/2005GL024029.shtml.

[29] Jonathan M. Castro, P Beck, Hugh Tuffen, Alexander R L Nichols, Donald B. Dingwell, and M C Martin. Timescales of spherulite crystallization in obsidian inferred from water concentration profiles. *American Mineralogist*, 93(11-12):1816–1822, 2008. ISSN 0003-004X. doi: 10.2138/am.2008.2904. URL http://ammin.geoscienceworld.org/cgi/doi/10.2138/am.2008.2904.

[30] Jonathan M. Castro, Elizabeth Cottrell, Hugh Tuffen, Amelia V Logan, and Katherine A Kelley. Spherulite crystallization induces Fe-redox redistribution in silicic melt. *Chemical Geology*, 268(3-4):272–280, 2009. ISSN 0009-2541. doi: 10.1016/j.chemgeo.2009.09.006. URL http://dx.doi.org/10.1016/j.chemgeo.2009.09.006.

[31] Jonathan M. Castro, Alain Burgisser, C. Ian Schipper, and Simona Mancini. Mechanisms of bubble coalescence in silicic magmas. *Bulletin of Volcanology*, 74(10):2339–2352, October 2012. ISSN 0258-8900. doi: 10.1007/s00445-012-0666-1. URL http://www.springerlink.com/index/10.1007/s00445-012-0666-1http://link.springer.com/10.1007/s00445-012-0666-1.

[32] Jonathan M. Castro, Benoit Cordonnier, Hugh Tuffen, Mark J. Tobin, Ljiljana Puskar, Michael C. Martin, and Hans a. Bechtel. The role of melt-fracture degassing in defusing explosive rhyolite eruptions at volcán Chaitén. *Earth and*

Planetary Science Letters, 333-334:63–69, June 2012. ISSN 0012821X. doi: 10.1016/j.epsl.2012.04.024. URL http://linkinghub.elsevier.com/retrieve/pii/S0012821X12001914.

[33] D. J. Cherniak, Richard L. Hervig, J. Koepke, Youxue Zhang, and D. Zhao. Analytical Methods in Diffusion Studies. *Reviews in Mineralogy and Geochemistry*, 72 (1):107–170, November 2010. ISSN 1529-6466. doi: 10.2138/rmg.2010.72.4. URL http://rimg.geoscienceworld.org/cgi/doi/10.2138/rmg.2010.72.4.

[34] Peter Anthony Cocheo. *The solubility of water in basanitic melts at low pressures.* PhD thesis, Arizona State University, 1994.

[35] P. D. Cole, E S Calder, T H Druitt, R Hoblitt, R Robertson, R S J Sparks, and S. R. Young. Pyroclastic flows generated by gravitational instability of the 1996-97 Lava Dome of Soufriere Hills Volcano, Montserrat. *Geophysical Research Letters*, 25(18):3425–3428, September 1998. ISSN 00948276. doi: 10.1029/98GL01510. URL http://doi.wiley.com/10.1029/98GL01510.

[36] BK Davis and Jocelyn McPhie. Spherulites, quench fractures and relict perlite in a Late Devonian rhyolite dyke, Queensland, Australia. *Journal of volcanology and geothermal research*, 71(1):1–11, 1996. URL http://www.sciencedirect.com/science/article/pii/0377027395000631.

[37] J.R. Delaney and J.L. Karsten. Ion microprobe studies of water in silicate melts. Concentration-dependent water diffusion in obsidian. *Earth and Planetary Science Letters*, 52(1):191–202, January 1981. ISSN 0012821X. doi: 10.1016/0012-821X(81)90220-X. URL http://linkinghub.elsevier.com/retrieve/pii/0012821X8190220X.

[38] J.S. Denton, Hugh Tuffen, J.S. Gilbert, and N Odling. The hydration and alteration of perlite and rhyolite. *Journal of the Geological Society*, 166(5):895–904, 2009. ISSN 0016-7649. doi: 10.1144/0016-76492008-007. URL http://jgs.lyellcollection.org/cgi/doi/10.1144/0016-76492008-007.

[39] J D Devine, James E. Gardner, H P Brack, G D Layne, and M J Rutherford. Comparison Of Microanalytical Methods For Estimating H2o Contents Of Silicic Volcanic Glasses. *American Mineralogist*, 80(3-4):319–328, 1995.

[40] V. Di Matteo, M.R. Carroll, Harald Behrens, F. Vetere, and R.a. Brooker. Water solubility in trachytic melts. *Chemical Geology*, 213(1-3):187–196, December 2004. ISSN 00092541. doi: 10.1016/j.chemgeo.2004.08.042. URL http://linkinghub.elsevier.com/retrieve/pii/S0009254104003419.

[41] A. Di Muro, B Villemant, G Montagnac, B Scaillet, and B Reynard. Quantification of water content and speciation in natural silicic glasses (phonolite, dacite, rhyolite) by confocal microRaman spectrometry. *Geochimica et Cosmochimica Acta*, 70 (11):2868–2884, June 2006. ISSN 00167037. doi: 10.1016/j.gca.2006.02.016. URL http://linkinghub.elsevier.com/retrieve/pii/S0016703706001025.

[42] K. Diller, a. B. Clarke, B. Voight, and a. Neri. Mechanisms of conduit plug formation: Implications for vulcanian explosions. *Geophysical Research Letters*, 33(20):1–6, October 2006. ISSN 0094-8276. doi: 10.1029/2006GL027391. URL http://www.agu.org/pubs/crossref/2006/2006GL027391.shtml.

[43] Donald B. Dingwell. Volcanic Dilemma : Flow or Blow? *Science*, 273(5278):1054–1055, 1996. URL http://www.sciencemag.org/content/273/5278/1054.short.

[44] Donald B. Dingwell and S L Webb. Relaxation in silicate melts. *European Journal of Mineralogy*, 2(4):427–449, 1990.

[45] JE Dixon, EM Stolper, and JR Holloway. An experimental study of water and carbon dioxide solubilities in mid-ocean ridge basaltic liquids. Part I: calibration and solubility models. *Journal of Petrology*, 36(6):1607–1631, December 1995. URL http://petrology.oxfordjournals.org/content/36/6/1607.short.

[46] Patrick F Dobson, Samuel Epstein, and Edward M Stolper. Hydrogen isotope fractionation between coexisting vapor and silicate glasses and melts at low pressure. *Geochimica et Cosmochimica Acta*, 53(10):2723–2730, October 1989. ISSN 00167037. doi: 10.1016/0016-7037(89)90143-9. URL http://linkinghub.elsevier.com/retrieve/pii/0016703789901439.

[47] A. Einstein. Über die von der molekularkinetischen Theorie der Wärme geforderte Bewegung von in ruhenden Flüssigkeiten suspendierten Teilchen. *Annalen der Physik*, 322(8):549–560, 1905. ISSN 00033804. doi: 10.1002/andp.19053220806. URL http://doi.wiley.com/10.1002/andp.19053220806.

[48] PM Fenn. The Nucleation and Growth of Alkali Feldspars From Hydrous Melts. *The Canadian Mineralogist*, 15:135–161, 1977. URL http://canmin.geoscienceworld.org/content/15/2/135.short.

[49] Annika Ferk, R. Leonhardt, Felix W. von Aulock, Kai-uwe Hess, and Donald B. Dingwell. Paleointensities of phonolitic obsidian: Influence of emplacement rotations and devitrification. *Journal of Geophysical Research*, 116(B12): 1–18, December 2011. ISSN 0148-0227. doi: 10.1029/2011JB008397. URL http://www.agu.org/pubs/crossref/2011/2011JB008397.shtml.

[50] Gerald Fine and Edward Stolper. The speciation of carbon dioxide in sodium aluminosilicate glasses. *Contributions to Mineralogy and Petrology*, 91(2):105–121, 1985. ISSN 0010-7999. doi: 10.1007/BF00377759. URL `http://dx.doi.org/10.1007/BF00377759`.

[51] J.H. Fink. Structure and emplacement of a rhyolitic obsidian flow: Little Glass Mountain, Medicine Lake Highland, northern California. *Geological Society of America Bulletin*, 94(3):362, 1983. ISSN 0016-7606. URL `http://gsabulletin.gsapubs.org/content/94/3/362.short`.

[52] Irving Friedman and J. Obradovich. Obsidian hydration dating of volcanic events. *Quaternary Research*, 16(1):37–47, 1981. URL `http://linkinghub.elsevier.com/retrieve/pii/0033589481901265`.

[53] Irving Friedman and R L Smith. The deuterium content of water in some volcanic glasses. *Geochimica et Cosmochimica Acta*, 15(3):218–228, 1958. ISSN 00167037. doi: 10.1016/0016-7037(58)90059-0. URL `http://dx.doi.org/10.1016/0016-7037(58)90059-0http://linkinghub.elsevier.com/retrieve/pii/0016703758900590`.

[54] Irving Friedman, R L Smith, and W D Long. Hydration of natural glass and formation of perlite. *Geological Society of America Bulletin*, 77(March):323–328, 1966. URL `http://gsabulletin.gsapubs.org/content/77/3/323.short`.

[55] Hélène Gaonac'h, S Lovejoy, and D Schertzer. Percolating magmas and explosive volcanism. *Geophysical Research Letters*, 30(11):1559, 2003. ISSN 0094-8276. doi: 10.1029/2002GL016022. URL `http://onlinelibrary.wiley.com/doi/10.1029/2002GL016022/fullhttp://doi.wiley.com/10.1029/2002GL016022`.

[56] James E. Gardner, M H Ilton, and M R C Arroll. Bubble growth in highly viscous silicate melts during continuous decompression from high pressure. *Geochimica et Cosmochimica Acta*, 64(8):1473–1483, 2000.

[57] James E. Gardner, Kenneth S. Befus, James Watkins, Marc Hesse, and Nathan Miller. Compositional gradients surrounding spherulites in obsidian and their relationship to spherulite growth and lava cooling. *Bulletin of Volcanology*, 74(8):1865–1879, July 2012. ISSN 0258-8900. doi: 10.1007/s00445-012-0642-9. URL `http://www.springerlink.com/index/10.1007/s00445-012-0642-9`.

[58] Mark S. Ghiorso and Richard O. Sack. Chemical mass transfer in magmatic processes IV. A revised and internally consistent thermodynamic model for the interpolation and extrapolation of liquid-solid equilibria in magmatic systems at elevated temperatures and pressures. *Contributions to Mineralogy and Petrology*,

119(2-3):197–212, March 1995. ISSN 0010-7999. doi: 10.1007/BF00307281. URL http://www.springerlink.com/index/10.1007/BF00307281.

[59] Daniele Giordano, Alexander R L Nichols, and Donald B. Dingwell. Glass transition temperatures of natural hydrous melts: a relationship with shear viscosity and implications for the welding process. *Journal of Volcanology and Geothermal Research*, 142(1-2):105–118, 2005. ISSN 03770273. doi: 10.1016/j.jvolgeores.2004.10.015. URL http://linkinghub.elsevier.com/retrieve/pii/S0377027304004056.

[60] Daniele Giordano, J.K. K Russell, and Donald B. Dingwell. Viscosity of magmatic liquids: A model. *Earth and Planetary Science Letters*, 271(1-4):123–134, 2008. ISSN 0012-821X. doi: 10.1016/j.epsl.2008.03.038. URL http://linkinghub.elsevier.com/retrieve/pii/S0012821X08002240.

[61] C. Gonde, C. Martel, M. Pichavant, and H. Bureau. In situ bubble vesiculation in silicic magmas. *American Mineralogist*, 96(1):111–124, December 2010. ISSN 0003-004X. doi: 10.2138/am.2011.3546. URL http://ammin.geoscienceworld.org/cgi/doi/10.2138/am.2011.3546.

[62] Helge M. Gonnermann and Michael Manga. Flow banding in obsidian: A record of evolving textural heterogeneity during magma deformation. *Earth and Planetary Science Letters*, 236(1-2):135–147, July 2005. ISSN 0012821X. doi: 10.1016/j.epsl.2005.04.031. URL http://linkinghub.elsevier.com/retrieve/pii/S0012821X05002815.

[63] HM Gonnermann and M Manga. Nonequilibrium magma degassing: Results from modeling of the ca. 1340 A.D. eruption of Mono Craters, California. *Earth and Planetary Science Letters*, 238(1-2):1–16, 2005. ISSN 0012821X. doi: 10.1016/j.epsl.2005.07.021. URL http://linkinghub.elsevier.com/retrieve/pii/S0012821X05005029.

[64] Joachim Gottsmann and Donald B. Dingwell. The thermal history of a spatter-fed lava flow: the 8-ka pantellerite flow of Mayor Island, New Zealand. *Bulletin of Volcanology*, 64(6):410–422, September 2002. ISSN 0258-8900. doi: 10.1007/s00445-002-0220-7. URL http://www.springerlink.com/openurl.asp?genre=article&id=doi:10.1007/s00445-002-0220-7.

[65] Erik Hauri, Jianhua Wang, J.E. Dixon, P.L. King, Charles Mandeville, and Sally Newman. SIMS analysis of volatiles in silicate glasses: 1. Calibration, matrix effects and comparisons with FTIR. *Chemical Geology*, 183(1-4):99–114, 2002. URL http://www.sciencedirect.com/science/article/pii/S0009254101003758.

[66] Richard L. Hervig, Nelia Dunbar, H. R. Westrich, and P Kyle. Pre-eruptive water content of rhyolitic magmas as determined by ion microprobe analyses of melt inclusions in phenocrysts. *Journal of Volcanology and Geothermal Research*, 36 (4):293–302, 1989. ISSN 03770273. doi: 10.1016/0377-0273(89)90075-9. URL `http://linkinghub.elsevier.com/retrieve/pii/0377027389900759`.

[67] Richard L. Hervig, Frank K. Mazdab, Gordon Moore, and Paul F. McMillan. *Melt Inclusions in Volcanic Systems - Methods, Applications and Problems*, volume 5 of *Developments in Volcanology*. Elsevier, 2003. ISBN 9780444511515. doi: 10.1016/S1871-644X(03)80025-6. URL `http://dx.doi.org/10.1016/S1871-644X(03)80025-6`.

[68] Kai-uwe Hess and Donald B. Dingwell. Viscosities of hydrous leucogranitic melts: A non-Arrhenian model. *The American Mineralogist*, 81(9/10):1297–1300, 1996. URL `http://www.minsocam.org/msa/AmMin/toc/Articles_Free/1996/Hess_p1297-1299_96.pdf`.

[69] Marc a. Hesse. A finite volume method for trace element diffusion and partitioning during crystal growth. *Computers & Geosciences*, 46:96–106, September 2012. ISSN 00983004. doi: 10.1016/j.cageo.2012.04.009. URL `http://linkinghub.elsevier.com/retrieve/pii/S009830041200132X`.

[70] Ivan L Heureux. A new model of volatile bubble growth in a magmatic system : Isobaric case. *October*, 112:1–14, 2007. doi: 10.1029/2006JB004872.

[71] François Holtz, Harald Behrens, Donald B. Dingwell, and W Johannes. H2o Solubility In Haplogranitic Melts - Compositional, Pressure, And Temperature-Dependence. *American Mineralogist*, 80(1-2):94–108, 1995.

[72] BF Houghton, SD Weaver, Colin J. N. Wilson, and M A Lanphere. Evolution of a Quaternary peralkaline volcano: Mayor Island, New Zealand. *Journal of volcanology ...*, 51(3):217–236, 1992. URL `http://www.sciencedirect.com/science/article/pii/037702739290124V`.

[73] M C S Humphreys, T Menand, J D Blundy, and K Klimm. Magma ascent rates in explosive eruptions: constraints from H2O diffusion in melt inclusions. *Earth and Planetary Science Letters*, 270:25–40, 2008.

[74] Shaul Hurwitz and Oded Navon. Bubble nucleation in rhyolitic melts: Experiments at high pressure, temperature, and water content. *Earth and Planetary Science Letters*, 122:267–280, 1994. URL `http://www.sciencedirect.com/science/article/pii/0012821X94900019`.

[75] Y Ida. Driving force of lateral permeable gas flow in magma and the criterion of explosive and effusive eruptions. *Journal of Volcanology and Geothermal Research*, 162(3-4):172–184, 2007. ISSN 03770273. doi: 10.1016/j.jvolgeores.2007.03.005. URL `http://linkinghub.elsevier.com/retrieve/pii/S0377027307000741`.

[76] Phillip D. Ihinger, Richard L. Hervig, Paul F. McMillan, Youxue Zhang, and Edward M Stolper. Analytical methods for volatiles in glasses. *Reviews in Mineralogy and Geochemistry*, 30(1):67–121, January 1994. URL `http://www.sciencedirect.com/science/article/pii/S001670379900277X`.

[77] J.B Johnson and J.M Lees. Plugs and chugsseismic and acoustic observations of degassing explosions at Karymsky, Russia and Sangay, Ecuador. *Journal of Volcanology and Geothermal Research*, 101(1-2):67–82, August 2000. ISSN 03770273. doi: 10.1016/S0377-0273(00)00164-5. URL `http://linkinghub.elsevier.com/retrieve/pii/S0377027300001645`.

[78] B. M. Kennedy, Oliver Spieler, B. Scheu, U. Kueppers, Jacopo Taddeucci, and Donald B. Dingwell. Conduit implosion during Vulcanian eruptions. *Geology*, 33(7):581–584, 2005. ISSN 0091-7613. doi: 10.1130/g21488.1. URL `http://geology.gsapubs.org/cgi/doi/10.1130/G21488.1`.

[79] B. M. Kennedy, a.M. Jellinek, J.K. Russell, Alexander R L Nichols, and N. Vigouroux. Time-and temperature-dependent conduit wall porosity: A key control on degassing and explosivity at Tarawera volcano, New Zealand. *Earth and Planetary Science Letters*, September 2010. ISSN 0012821X. doi: 10.1016/j.epsl.2010.08.028. URL `http://linkinghub.elsevier.com/retrieve/pii/S0012821X10005406`.

[80] L. A. Kennedy, J. K. Russell, and E. Nelles. Origins of Mount St. Helens cataclasites: Experimental insights. *American Mineralogist*, 94(7):995–1004, June 2009. ISSN 0003-004X. doi: 10.2138/am.2009.3129. URL `http://ammin.geoscienceworld.org/cgi/doi/10.2138/am.2009.3129`.

[81] Caroline Klug and Katharine V. Cashman. Permeability development in vesiculating magmas: implications for fragmentation. *Bull. Volcanol.*, 58(2-3):87–100, 1996. ISSN 0258-8900. doi: 10.1007/s004450050128. URL `http://www.springerlink.com/openurl.asp?genre=article&id=doi:10.1007/s004450050128`.

[82] U Kueppers, B Scheu, Oliver Spieler, and Donald B. Dingwell. Field-based density measurements as tool to identify preeruption dome structure: set-up and first results from Unzen volcano, Japan. *Journal of Volcanology and Geothermal Research*, 141(1-2):65–75, 2005. doi: 10.1016/j.jvolgeores.2004.09.005.

[83] RA Lange. A revised model for the density and thermal expansivity of K2O-Na2O-CaO-MgO-Al2O3-SiO2 liquids from 700 to 1900 K: extension to crustal magmatic temperatures. *Contributions to Mineralogy and Petrology*, pages 1–11, 1997. URL `http://www.springerlink.com/index/P63JTBQ3BPJFR49A.pdf`.

[84] RL Lange and ISE Carmichael. Thermodynamic properties of silicate liquids with emphasis on density, thermal expansion and compressibility. *Reviews in Mineralogy and ...*, 24(1):25–64, 1990. URL `http://rimg.geoscienceworld.org/content/24/1/25.short`.

[85] Jessica F. Larsen and James E. Gardner. Experimental constraints on bubble interactions in rhyolite melts: implications for vesicle size distributions. *Earth and Planetary Science Letters*, 180:201–214, 2000.

[86] Jessica F. Larsen, MH Denis, and James E. Gardner. Experimental study of bubble coalescence in rhyolitic and phonolitic melts. *Geochimica et cosmochimica acta*, 68(2):333–344, 2004. doi: 10.1016/S0016-7037(03)00412-5. URL `http://www.sciencedirect.com/science/article/pii/S0016703703004125`.

[87] Yan Lavallée, Kai-uwe Hess, and Benoit Cordonnier. Non-Newtonian rheological law for highly crystalline dome lavas. *Glass*, (9):843–846, 2007. doi: 10.1130/G23594A.1.

[88] Yan Lavallée, PG G Meredith, Donald B. Dingwell, K.U. K-U Hess, J Wassermann, B Cordonnier, A Gerik, and JH H Kruhl. Seismogenic lavas and explosive eruption forecasting. *Nature*, 453(7194):507–510, 2008. ISSN 0028-0836. doi: 10.1038/nature06980. URL `http://www.nature.com/nature/journal/vaop/ncurrent/full/nature06980.htmlhttp://www.ncbi.nlm.nih.gov/pubmed/18497822`.

[89] Yan Lavallée, P. M. Benson, M. J. Heap, K.-U. Hess, a. Flaws, B. Schillinger, P. G. Meredith, and Donald B. Dingwell. Reconstructing magma failure and the degassing network of dome-building eruptions. *Geology*, February 2013. ISSN 0091-7613. doi: 10.1130/G33948.1. URL `http://geology.gsapubs.org/cgi/doi/10.1130/G33948.1`.

[90] Priscille Lesne, Bruno Scaillet, Michel Pichavant, Giada Iacono-Marziano, and Jean-Michel Beny. The H2O solubility of alkali basaltic melts: an experimental study. *Contributions to Mineralogy and Petrology*, 162(1):133–151, November 2010. ISSN 0010-7999. doi: 10.1007/s00410-010-0588-x. URL `http://link.springer.com/10.1007/s00410-010-0588-x`.

[91] Y Liu, Youxue Zhang, and Harald Behrens. Solubility of H2O in rhyolitic melts at low pressures and a new empirical model for mixed H 2 O-CO 2 solubility in

rhyolitic melts, J. *Journal of Volcanology and Geothermal Research*, 143:219–235, 2005.

[92] Yang Liu and Youxue Zhang. Bubble growth in rhyolitic melt. *Earth and Planetary Science Letters*, 181:251–264, 2000.

[93] C Le Losq and DR Neuville. Determination of water content in silicate glasses using Raman spectrometry: Implications for the study of explosive volcanism. *American ...*, 97:779–790, 2012. URL `http://ammin.geoscienceworld.org/content/97/5-6/779.short`.

[94] S Lovejoy, Hélène Gaonac'h, and D Schertzer. Bubble distributions and dynamics: the expansion-coalescence equation. *Journal of Geophysical Research*, 109doi: 101029/, 2004.

[95] Vladimir Lyakhovsky and S Hurwitz. Bubble growth in rhyolitic melts: experimental and numerical investigation. *Bulletin of volcanology*, pages 19–32, 1996. URL `http://www.springerlink.com/index/T09R8A9A7P5QDVJR.pdf`.

[96] M Manga. Deformation of flow bands by bubbles and crystals. *SPECIAL PAPERS-GEOLOGICAL SOCIETY OF ...*, 396:47–53, 2005. doi: 10.1130/0-8137-2396-5.47. URL `http://books.google.com/books?hl=en&lr=&id=efqyc-fh82YC&oi=fnd&pg=PA47&dq=Deformation+of+flow+bands+by+bubbles+and+crystals&ots=osZmPhfKUS&sig=wL0KasCnzRP7qnLtIyFCNRq-A7E`.

[97] M. T. Mangan. Decompression experiments identify kinetic controls on explosive silicic eruptions. *Geophysical Research Letters*, 31(8):L08605, 2004. ISSN 0094-8276. doi: 10.1029/2004GL019509. URL `http://doi.wiley.com/10.1029/2004GL019509`.

[98] M. T. Mangan and Thomas W. Sisson. Evolution of melt-vapor surface tension in silicic volcanic systems: Experiments with hydrous melts. *Journal of Geophysical Research*, 110(B1):B01202, 2005. ISSN 0148-0227. doi: 10.1029/2004JB003215. URL `http://doi.wiley.com/10.1029/2004JB003215http://onlinelibrary.wiley.com/doi/10.1029/2004JB003215/fullhttp://www.agu.org/pubs/crossref/2005/2004JB003215.shtml`.

[99] M. T. Mangan, Katharine V. Cashman, and S Newman. Vesiculation of basaltic magma during eruption. *Geology*, (L), 1993. URL `http://geology.gsapubs.org/content/21/2/157.short`.

[100] RR Marshall. Devitrification of Natural Glass. *Geological Society of America Bulletin*, (October):1493–1520, 1961. URL `http://gsabulletin.gsapubs.org/content/72/10/1493.short`.

[101] I. M. McIntosh, E. W. Llewellin, M. Humphreys, Jessica F. Larsen, and J. D. Blower. Reconstructing the Growth History of Bubbles in Magma from Preserved Volatile Concentrations in Glass. *AGU Fall Meeting Abstracts*, -1:2366, December 2010. URL http://adsabs.harvard.edu/abs/2010AGUFM.V43B2366M.

[102] Jocelyn McPhie, M Doyle, and S.R. Allen. *Volcanic textures: a guide to the interpretation of textures in volcanic rocks*. CODES, University of Tasmania, Hobart, 1993. ISBN 085901522. URL http://scholar.google.com/scholar?hl=en&btnG=Search&q=intitle:Volcanic+textures+:+a+guide+to+the+interpretation+of+textures+in+volcanic+rocks#0.

[103] Lisa M Miller and Randy J Smith. Synchrotrons versus globars, point-detectors versus focal plane arrays: Selecting the best source and detector for specific infrared microspectroscopy and imaging applications. *Vibrational Spectroscopy*, 38 (1-2):237–240, July 2005. ISSN 09242031. doi: 10.1016/j.vibspec.2005.03.010. URL http://linkinghub.elsevier.com/retrieve/pii/S0924203105000676.

[104] J Mongrain, Jessica F. Larsen, and P L King. Rapid water exsolution, degassing and bubble collapse observed experimentally in K-phonolite melts. *Journal of Volcanology and Geothermal Research*, 173:178–184, 2008. doi: 10.1016/j.jvolgeores.2008.01.026.

[105] Gordon Moore, Torsten Vennemann, and I. S. E. Carmichael. Solubility of water in magmas to 2 kbar. *Geology*, 23(12):1099, 1995. ISSN 0091-7613. doi: 10.1130/0091-7613(1995)023⟨1099:SOWIMT⟩2.3.CO;2. URL http://geology.gsapubs.org/cgi/doi/10.1130/0091-7613(1995)023<1099:SOWIMT>2.3.CO;2.

[106] H.W. Morse, C.H. Warren, and J.D.H. Donnay. Artificial spherulites and related aggregates. *American Journal of Science*, 5(137):421, 1932. URL http://www.ajsonline.org/cgi/content/abstract/s5-23/137/421.

[107] Catherine C. Mourtada-Bonnefoi and Didier Laporte. Experimental study of homogeneous bubble nucleation in rhyolitic magmas. *Geophysical Research Letters*, 26(23):3505–3508, December 1999. ISSN 00948276. doi: 10.1029/1999GL008368. URL http://www.agu.org/pubs/crossref/1999/1999GL008368.shtmlhttp://doi.wiley.com/10.1029/1999GL008368.

[108] CT Cornelius T. Moynihan. Structural relaxation and the glass transition. *Reviews in Mineralogy and Geochemistry*, 32(1):1–19, January 1995. URL http://rimg.geoscienceworld.org/cgi/content/abstract/32/1/1http://rimg.geoscienceworld.org/cgi/content/long/32/1/1.

[109] Sebastian Mueller, Oleg Melnik, Oliver Spieler, Bettina Scheu, and Donald B. Dingwell. Permeability and degassing of dome lavas undergoing rapid decompression: An experimental determination. *Bull. Volcanol.*, 67(6):526–538, 2004. ISSN 0258-8900. doi: 10.1007/s00445-004-0392-4. URL `http://www.springerlink.com/index/10.1007/s00445-004-0392-4`.

[110] Oded Navon and Vladimir Lyakhovsky. Vesiculation processes in silicic magmas. *Geological Society, London, Special Publications*, 145(1):27–50, January 1998. ISSN 0305-8719. doi: 10.1144/GSL.SP.1996.145.01.03. URL `http://sp.lyellcollection.org/content/145/1/27.shorthttp://sp.lyellcollection.org/cgi/doi/10.1144/GSL.SP.1996.145.01.03`.

[111] Oded Navon, Anatoly Chekhmir, and Vladimir Lyakhovsky. Bubble growth in highly viscous melts: theory, experiments, and autoexplosivity of dome lavas. *Earth and Planetary Science Letters*, 160(3-4):763–776, August 1998. ISSN 0012821X. doi: 10.1016/S0012-821X(98)00126-5. URL `http://linkinghub.elsevier.com/retrieve/pii/S0012821X98001265`.

[112] S. Newman, E.M. Stolper, and S. Epstein. Measurement of water in rhyolitic glasses: calibration of an infrared spectroscopic technique. *Am. Mineral.;(United States)*, 71:11-12, 1986. URL `http://www.osti.gov/energycitations/product.biblio.jsp?osti_id=6773661`.

[113] Alexander R L Nichols and R. J. Wysoczanski. Using micro-FTIR spectroscopy to measure volatile contents in small and unexposed inclusions hosted in olivine crystals. *Chemical Geology*, 242(3-4):371–384, 2007. ISSN 00092541. doi: 10.1016/j.chemgeo.2007.04.007. URL `http://linkinghub.elsevier.com/retrieve/pii/S0009254107001763http://dx.doi.org/10.1016/j.chemgeo.2007.04.007`.

[114] Satoshi Noguchi, Atsushi Toramaru, and Taketo Shimano. Crystallization of microlites and degassing during magma ascent: Constraints on the fluid mechanical behavior of magma during the Tenjo Eruption on Kozu Island, Japan. *Bulletin of Volcanology*, 68(5):432–449, January 2006. ISSN 0258-8900. doi: 10.1007/s00445-005-0019-4. URL `http://www.springerlink.com/index/10.1007/s00445-005-0019-4`.

[115] Marcus Nowak and Harald Behrens. Water in rhyolitic magmas: getting a grip on a slippery problem. *Earth and Planetary Science Letters*, 184(2):515–522, 2001. ISSN 0012821X. doi: 10.1016/S0012-821X(00)00343-5. URL `http://linkinghub.elsevier.com/retrieve/pii/S0012821X00003435`.

[116] FA Ochs and RA Lange. The density of hydrous magmatic liquids. *Science*, 283 (5406):1314–1317, 1999. URL http://www.sciencemag.org/content/283/5406/1314.short.

[117] Satoshi Okumura. Molar absorptivities of OH and H2O in rhyolitic glass at room temperature and at 400-600 C. *American Mineralogist*, 90(2-3):441–447, February 2005. ISSN 0003-004X. doi: 10.2138/am.2005.1740. URL http://ammin.geoscienceworld.org/cgi/doi/10.2138/am.2005.1740.

[118] Satoshi Okumura, Michihiko Nakamura, Shingo Takeuchi, Akira Tsuchiyama, Tsukasa Nakano, and Kentaro Uesugi. Magma deformation may induce non-explosive volcanism via degassing through bubble networks. *Earth and Planetary Science Letters*, 281(3-4):267–274, 2009. ISSN 0012821X. doi: 10.1016/j.epsl.2009.02.036. URL http://linkinghub.elsevier.com/retrieve/pii/S0012821X09001381.

[119] Jacqueline Owen, Hugh Tuffen, and D. W. McGarvie. Explosive subglacial rhyolitic eruptions in Iceland are fuelled by high magmatic H2O and closed-system degassing. *Geology*, 41(2):251–254, November 2012. ISSN 0091-7613. doi: 10.1130/G33647.1. URL http://geology.gsapubs.org/cgi/doi/10.1130/G33647.1.

[120] P. Papale, R Moretti, and D Barbato. The compositional dependence of the saturation surface of H2O+CO2 fluids in silicate melts. *Chemical Geology*, 229 (1-3):78–95, May 2006. ISSN 00092541. doi: 10.1016/j.chemgeo.2006.01.013. URL http://linkinghub.elsevier.com/retrieve/pii/S0009254106000532.

[121] Thomas Platz, Shane J Cronin, Katharine V. Cashman, Robert B Stewart, and Ian E.M. M Smith. Transition from effusive to explosive phases in andesite eruptions A case-study from the AD1655 eruption of Mt. Taranaki, New Zealand. *Journal of Volcanology and Geothermal Research*, 161(1-2):15–34, 2007. ISSN 03770273. doi: 10.1016/j.jvolgeores.2006.11.005. URL http://linkinghub.elsevier.com/retrieve/pii/S0377027306003908.

[122] Thomas Platz, Shane J Cronin, Jonathan N Procter, Vincent E Neall, and Stephen F Foley. Non-explosive, dome-forming eruptions at Mt. Taranaki, New Zealand. *Geomorphology*, 136(1):15–30, January 2012. ISSN 0169555X. doi: 10.1016/j.geomorph.2011.06.016. URL http://linkinghub.elsevier.com/retrieve/pii/S0169555X11003126.

[123] M Potuzak and Donald B. Dingwell. Temperature-dependent thermal expansivities of multicomponent natural melts between 993 and 1803 K. *Chemical Geology*, 229: 10 – 27, 2006. doi: 10.1016/j.chemgeo.2006.01.009.

[124] Alexander A Proussevitch and D. L Sahagian. Bubbledrive-1: A numerical model of volcanic eruption mechanisms driven by disequilibrium magma degassing. *Journal of Volcanology and Geothermal Research*, 143(1-3):89–111, May 2005. ISSN 03770273. doi: 10.1016/jvolgeores.204.09.012. URL `http://linkinghub.elsevier.com/retrieve/pii/S0377027305000375`.

[125] Alexander A Proussevitch and Dork L. Sahagian. Dynamics of coupled diffusive and decompressive bubble growth in magmatic systems. *Journal of Geophysical Research*, 101(B8):17447, 1996. ISSN 0148-0227. doi: 10.1029/96JB01342. URL `http://www.agu.org/pubs/crossref/1996/96JB01342.shtml`.

[126] Alexander A Proussevitch, DL Sahagian, and AT Anderson. Dynamics of diffusive bubble growth in magmas: Isothermal case. *Journal of geophysical . . .*, 98, 1993. URL `http://www.agu.org/pubs/crossref/1993/93JB02027.shtml`.

[127] M.J. Richardson and N.G. Savill. Derivation of accurate glass transition temperatures by differential scanning calorimetry. *Polymer*, 16(10):753–757, October 1975. ISSN 00323861. doi: 10.1016/0032-3861(75)90194-9. URL `http://linkinghub.elsevier.com/retrieve/pii/0032386175901949`.

[128] J Richnow. *Eruptional And Post-Eruptional Processes In Rhyolite Domes*. Phd thesis, Unversity of Canterbury, 1999. URL `http://ir.canterbury.ac.nz/handle/10092/5724`.

[129] G. Robert, J.K. Russell, D. Giordano, and C. Romano. High-temperature deformation of volcanic materials in the presence of water. *American Mineralogist*, 93(1):74–80, January 2008. ISSN 0003-004X. doi: 10.2138/am.2008.2665. URL `http://ammin.geoscienceworld.org/cgi/doi/10.2138/am.2008.2665`.

[130] C Romano, Donald B. Dingwell, and Harald Behrens. The temperature dependence of the speciation of water in NaAlSi3O8 -KAlSi3O8 melts : an application of fictive temperatures from synthetic derived. *Contributions to Mineralogy and Petrology*, 122:1–10, 1995.

[131] C Romano, JE Mungall, T Sharp, and Donald B. Dingwell. Tensile strengths of hydrous vesicular glasses: An experimental study. *American Mineralogist*, 81(9):1148–1154, 1996. ISSN 0003-004X. URL `http://minsocam.org/MSA/ammin/toc/Articles_Free/1996/Romano_p1148-1154_96.pdf`.

[132] Melissa D. Rotella, Colin J. N. Wilson, Simon J. Barker, and Ian C. Wright. Highly vesicular pumice generated by buoyant detachment of magma in subaqueous volcanism. *Nature Geoscience*, 6(2):129–132, January 2013. ISSN 1752-0894. doi: 10.1038/ngeo1709. URL `http://www.nature.com/doifinder/10.1038/ngeo1709`.

[133] A.C. Rust and Katharine V. Cashman. Permeability of vesicular silicic magma: inertial and hysteresis effects. *Earth and Planetary Science Letters*, 228(1-2):93–107, November 2004. ISSN 0012821X. doi: 10.1016/j.epsl.2004.09.025. URL http://linkinghub.elsevier.com/retrieve/pii/S0012821X04005771.

[134] A.C. Rust, M Manga, and Katharine V. Cashman. Determining flow type, shear rate and shear stress in magmas from bubble shapes and orientations. *Journal of Volcanology and Geothermal Research*, 122:111–132, 2003.

[135] A.C. Rust, Paul J Wallace, and Katharine V. Cashman. Magma degassing buffered by vapor flow through brecciated conduit margins. *Geology*, 32(4):349, 2004. ISSN 0091-7613. doi: 10.1130/G20388.2. URL http://geology.gsapubs.org/cgi/doi/10.1130/G20388.2.

[136] Steve T. Sahetapy-Engel and Andrew J L Harris. Thermal structure and heat loss at the summit crater of an active lava dome. *Bull. Volcanol.*, 71(1):15–28, 2008. ISSN 0258-8900. doi: 10.1007/s00445-008-0204-3. URL http://www.springerlink.com/index/10.1007/s00445-008-0204-3.

[137] C. Ian Schipper, James D.L. White, and Bruce F Houghton. Syn- and post-fragmentation textures in submarine pyroclasts from L'ihi Seamount, Hawai'i. *Journal of Volcanology and Geothermal Research*, 191(1-2):93–106, March 2010. ISSN 03770273. doi: 10.1016/j.jvolgeores.2010.01.002. URL http://dx.doi.org/10.1016/j.jvolgeores.2010.01.002http://linkinghub.elsevier.com/retrieve/pii/S0377027310000168.

[138] B C Schmidt and Harald Behrens. Water solubility in phonolite melts: Influence of melt composition and temperature. *Chemical Geology*, 256(3-4):259–268, 2008. doi: 10.1016/j.chemgeo.2008.06.043.

[139] Bernhard Schrader. *Infrared and raman spectroscopy : methods and applications.* VCH Verlagsgesellschaft mbH, 1 edition, 1995. ISBN 3-527-26446-9.

[140] S. J. Seaman. Microtexture development during rapid cooling in three rhyolitic lava flows. *American Mineralogist*, 98(2-3):304–318, February 2013. ISSN 0003-004X. doi: 10.2138/am.2013.4313. URL http://ammin.geoscienceworld.org/cgi/doi/10.2138/am.2013.4313.

[141] Sheila J Seaman, M Darby Dyar, and Nebojsa Marinkovic. The effects of heterogeneity in magma water concentration on the development of flow banding and spherulites in rhyolitic lava. *Journal of Volcanology and Geothermal Research*, 183 (3-4):157–169, 2009. ISSN 0377-0273. doi: 10.1016/j.jvolgeores.2009.03.001. URL http://dx.doi.org/10.1016/j.jvolgeores.2009.03.001.

[142] TG Sharp, R. J. Stevenson, and Donald B. Dingwell. Microlites and nanolites in rhyolitic glass: microstructural and chemical characterization. *Bulletin of volcanology*, pages 631–640, 1996. URL http://www.springerlink.com/index/VQQ14PT00JH4JV02.pdf.

[143] Thomas Shea, Lucia Gurioli, Jessica F. Larsen, Bruce F. Houghton, Julia E. Hammer, and Katharine V. Cashman. Linking experimental and natural vesicle textures in Vesuvius 79AD white pumice. *Journal of Volcanology and Geothermal Research*, 192(1-2):69–84, April 2010. ISSN 03770273. doi: 10.1016/j.jvolgeores.2010.02.013. URL http://linkinghub.elsevier.com/retrieve/pii/S0377027310000570.

[144] Alexander G Shtukenberg, Yuri O Punin, Erica Gunn, and Bart Kahr. Spherulites. *Chemical reviews*, 112(3):1805–38, March 2012. ISSN 1520-6890. doi: 10.1021/cr200297f. URL http://www.ncbi.nlm.nih.gov/pubmed/22103741.

[145] JV Smith. Structural analysis of flow-related textures in lavas. *Earth-Science Reviews*, 57:279–297, 2002. URL http://www.sciencedirect.com/science/article/pii/S0012825201000812.

[146] R.K. Smith, R.L. Tremallo, and G.E. Lofgren. Growth of megaspherulites in a rhyolitic vitrophyre. *American Mineralogist*, 86(5-6):589, 2001. ISSN 0003-004X. URL http://ammin.geoscienceworld.org/cgi/content/abstract/86/5-6/589.

[147] Robert Stephen John Sparks. The Dynamics of Bubble Formation and Growth in Magmas: A Review and Analysis. *Journal of Volcanology and Geothermal Research*, 3:1–37, 1978. URL http://adsabs.harvard.edu/abs/1978JVGR...3....1S.

[148] Robert Stephen John Sparks. Causes and consequences of pressurisation in lava dome eruptions. *Earth and Planetary Science Letters*, 150(3-4):177–189, 1997. URL http://linkinghub.elsevier.com/retrieve/pii/S0012821X9700109X.

[149] RSJ Sparks, S.R. Tait, and Y Yanev. Dense welding caused by volatile resorption. *Journal of the Geological ...*, 156:217–225, 1999. URL http://jgs.geoscienceworld.org/content/156/2/217.short.

[150] Frank J. Spera, David A. Yuen, John C. Greer, and Granville Sewell. Dynamics of magma withdrawal from stratified magma chambers. *Geology*, 14(9):723, 1986. ISSN 0091-7613. doi: 10.1130/0091-7613(1986)14⟨723:DOMWFS⟩2.0.CO;2. URL http://geology.gsapubs.org/cgi/doi/10.1130/0091-7613(1986)14<723:DOMWFS>2.0.CO;2.

[151] Oliver Spieler, B. M. Kennedy, U Kueppers, Donald B. Dingwell, B Scheu, and Jacopo Taddeucci. The fragmentation threshold of pyroclastic rocks: Earth and. *Planetary Science Letters*, v:101016/jepsl200407016, 2004.

[152] M.V. Stasiuk, J. Barclay, M R Carroll, Claude Jaupart, J.C. Ratté, Robert Stephen John Sparks, and S.R. Tait. Degassing during magma ascent in the Mule Creek vent (USA). *Bull. Volcanol.*, 58(2):117–130, 1996. URL `http://www.springerlink.com/index/BH116QCF95TCBLXD.pdf`.

[153] Christopher M. Stevenson and Steven W. Novak. Obsidian hydration dating by infrared spectroscopy: method and calibration. *Journal of Archaeological Science*, 38(7):1716–1726, July 2011. ISSN 03054403. doi: 10.1016/j.jas.2011.03.003. URL `http://linkinghub.elsevier.com/retrieve/pii/S0305440311000781`.

[154] R. J. Stevenson, RM Briggs, and APW Hodder. Physical volcanology and emplacement history of the Ben Lomond rhyolite lava flow , Taupo Volcanic Centre , New Zealand. *New Zealand Journal of Geology and Geophysics*, 37(3):345–358, 1994. URL `http://www.tandfonline.com/doi/abs/10.1080/00288306.1994.9514625`.

[155] R. J. Stevenson, Donald B. Dingwell, S L Webb, and N S Bagdassarov. The equivalence of enthalpy and shear stress relaxation in rhyolitic obsidians and quantification of the liquid-glass transition in volcanic processes. *Journal of Volcanology and Geothermal Research*, 68(95):297–306, 1995. ISSN 03770273. URL `http://www.sciencedirect.com/science/article/B6VCS-4002K2P-3/2/7603142eda3c5c94fac0698160650d5a`.

[156] R. J. Stevenson, Nicholas S Bagdassarov, Donald B. Dingwell, and C Romano. The influence of trace amounts of water on the viscosity of rhyolites. *Bull. Volcanol.*, 60(2):89–97, 1998. URL `http://www.springerlink.com/index/XKGFEXHDRGF53EDR.pdf`.

[157] John Stix, Roberto C. Torres, Lourdes M. Narváez, Gloria Patricia Cortés, Jaime A. Raigosa, Gómezo Diego M., and Robert Castonguay. A model of vulcanian eruptions at Galeras volcano, Colombia. *Journal of Volcanology and Geothermal Research*, 77:285–303, 1997. URL `http://www.sciencedirect.com/science/article/pii/S037702739600100X`.

[158] Edward Stolper, Gerald Fine, Thomas Johnson, and Sally Newman. Solubility of carbon dioxide in albitic melt, November 1987. URL `http://authors.library.caltech.edu/33447/`.

[159] Edward M Stolper. The speciation of water in silicate melts. *Geochimica et Cosmochimica Acta*, 46(12):2609–2620, 1982. ISSN 00167037. doi: 10.1016/0016-7037(82)90381-7. URL http://linkinghub.elsevier.com/retrieve/pii/0016703782903817.

[160] Edward M Stolper. Water in silicate glasses: An infrared spectroscopic study. *Contributions to Mineralogy and Petrology*, 81(1):1–17, 1982. ISSN 0010-7999. doi: 10.1007/BF00371154. URL http://link.springer.com/10.1007/BF00371154.

[161] S.E. E Swanson, M.T. T Naney, H. R. Westrich, and J. C. Eichelberger. Crystallization history of Obsidian Dome, Inyo Domes, California. *Bull. Volcanol.*, 51(3):161–176, 1989. ISSN 0258-8900. URL http://www.springerlink.com/index/T102340858727157.pdf.

[162] Jacopo Taddeucci, Oliver Spieler, M Ichihara, Donald B. Dingwell, and P Scarlato. Flow and fracturing of viscoelastic media under diffusion-driven bubble growth: An analogue experiment for eruptive volcanic conduits, Earth Planet. *Sci. Lett*, 243:771–785, 2006.

[163] B. Taisne and C. Jaupart. Magma degassing and intermittent lava dome growth. *Geophysical Research Letters*, 35(20):1–5, October 2008. ISSN 0094-8276. doi: 10.1029/2008GL035432. URL http://www.agu.org/pubs/crossref/2008/2008GL035432.shtml.

[164] Bruce E Taylor, J. C. Eichelberger, and H. R. Westrich. Hydrogen isotopic evidence of rhyolitic magma degassing during shallow intrusion and eruption. *Nature*, 306(5943):541–545, 1983. ISSN 0028-0836. doi: 10.1038/306541a0. URL http://www.nature.com/doifinder/10.1038/306541a0.

[165] Yves Thibault and JohnR. Holloway. Solubility of CO2 in a Ca-rich leucitite: effects of pressure, temperature, and oxygen fugacity. *Contributions to Mineralogy and Petrology*, 116(1-2):216–224, 1994. ISSN 0010-7999. doi: 10.1007/BF00310701. URL http://dx.doi.org/10.1007/BF00310701.

[166] Akihiko Tomiya. Numerical study of nucleation and growth of bubbles in viscous magmas. *Journal of Geophysical Research-Solid Earth*, 100(B2):1913–1931, 1995. URL http://www.agu.org/pubs/crossref/1995/94JB02775.shtml.

[167] Minoru Tomozawa and K Davis. Time dependent diffusion coefficient of water into silica glass at low temperatures1. *Materials Science and Engineering A*, 272(1):114–119, November 1999. ISSN 09215093. doi: 10.1016/S0921-5093(99)00463-3. URL http://linkinghub.elsevier.com/retrieve/pii/S0921509399004633.

[168] M.J. J Toplis, Joachim Gottsmann, R. Knoche, and Donald B. Dingwell. Heat capacities of haplogranitic glasses and liquids. *Geochimica Et Cosmochimica Acta*, 65 (12):1985–1994, 2001. URL http://linkinghub.elsevier.com/retrieve/pii/S0016703701005944.

[169] Atsushi Toramaru. Vesiculation Process and Bubble Size Distributions in Ascending Magmas With Constant Velocities. *Journal of Geophysical Research*, 94(89): 17523–17542, 1989.

[170] Atsushi Toramaru and T Miwa. Vesiculation and crystalization under instantaneous decompression: Numerical study and comparison with laboratory experiments. *Journal of Volcanology and Geothermal Research*, 177(4):983–996, 2008. ISSN 03770273. doi: 10.1016/j.jvolgeores.2008.07.013. URL http://linkinghub.elsevier.com/retrieve/pii/S0377027308004277.

[171] H Tuffen, Jacqueline Owen, and LJ Applegarth. Measurement of volatile concentrations in volcanic glasses using thermogravimetric analysis: comparison with micro-analytical methods. *EGU General Assembly ...*, 14:11347, 2012. URL http://adsabs.harvard.edu/abs/2012EGUGA..1411347T.

[172] Hugh Tuffen and Jonathan M. Castro. The emplacement of an obsidian dyke through thin ice: Hrafntinnuhryggur, Krafla Iceland. *Journal of Volcanology and Geothermal Research*, 185(4):352–366, September 2009. ISSN 03770273. doi: 10.1016/j.jvolgeores.2008.10.021. URL http://linkinghub.elsevier.com/retrieve/pii/S0377027308005726.

[173] Hugh Tuffen and Donald B. Dingwell. Fault textures in volcanic conduits: evidence for seismic trigger mechanisms during silicic eruptions. *Bull. Volcanol.*, 67(4): 370–387, 2004. ISSN 0258-8900. doi: 10.1007/s00445-004-0383-5. URL http://www.springerlink.com/index/10.1007/s00445-004-0383-5.

[174] Hugh Tuffen, Donald B. Dingwell, and H. Pinkerton. Repeated fracture and healing of silicic magma generate flow banding and earthquakes. *Geology*, 31(12):1089, 2003. URL http://geology.gsapubs.org/content/31/12/1089.full.

[175] A Turek, C Riddle, BJ Cozens, and NW Tetley. Determination of chemical water in rock analysis by Karl Fischer titration. *Chemical Geology*, 17:261–267, 1976. URL http://www.sciencedirect.com/science/article/pii/0009254176900401.

[176] OF Tuttle and NL Bowen. Origin of granite in the light of experimental studies in the system NaAlSi3O8-KAlSi3O8-SiO2-H2O: Geol. *Soc. America Mem*, 74(153), 1958. URL http://scholar.google.com/scholar?hl=en&btnG=Search&q=

intitle:Origin+of+granite+in+the+light+of+experimental+studies+in+the+system+NaAlSi3O8-KAlSi3O8-SiO2-H2O#0.

[177] F.W. von Aulock, a.R.L. Nichols, B. M. Kennedy, and C. Oze. Timescales of texture development in a cooling lava dome. *Geochimica et Cosmochimica Acta*, March 2013. ISSN 00167037. doi: 10.1016/j.gca.2013.03.012. URL http://linkinghub.elsevier.com/retrieve/pii/S0016703713001543.

[178] Paul J Wallace. Volatiles in subduction zone magmas: concentrations and fluxes based on melt inclusion and volcanic gas data. *Journal of Volcanology and Geothermal Research*, 140(1-3):217–240, 2005. ISSN 03770273. doi: 10.1016/j.jvolgeores.2004.07.023. URL http://linkinghub.elsevier.com/retrieve/pii/S0377027304002884.

[179] Paul J Wallace, AT Alfred T. Anderson, and AM Andrew M Davis. Quantification of pre-eruptive exsolved gas contents in silicic magmas. *Nature*, 377(6550):612–616, 1995. ISSN 0028-0836. doi: 10.1038/377612a0. URL http://www.nature.com/nature/journal/v377/n6550/abs/377612a0.htmlhttp://www.nature.com/doifinder/10.1038/377612a0.

[180] J. M. Watkins, M. Manga, and D. J. DePaolo. Bubble geobarometry: A record of pressure changes, degassing, and regassing at Mono Craters, California. *Geology*, pages 1–4, June 2012. ISSN 0091-7613. doi: 10.1130/G33027.1. URL http://geology.gsapubs.org/cgi/doi/10.1130/G33027.1.

[181] Jim Watkins, Michael Manga, Christian Huber, and Michael Martin. Diffusion-controlled spherulite growth in obsidian inferred from H2O concentration profiles. *Contributions to Mineralogy and Petrology*, 157(2):163–172, July 2008. ISSN 0010-7999. doi: 10.1007/s00410-008-0327-8. URL http://www.springerlink.com/index/10.1007/s00410-008-0327-8.

[182] S Webb and R Knoche. The glass-transition, structural relaxation and shear viscosity of silicate melts. *Chemical Geology*, 128:165–183, 1996.

[183] SL Webb and Donald B. Dingwell. Non-Newtonian rheology of igneous melts at high stresses and strain rates: experimental results for rhyolite, andesite, basalt, and nephelinite. *Journal of Geophysical ...*, 95, 1990. URL http://epub.ub.uni-muenchen.de/6012/.

[184] H. R. Westrich. Determination of water in volcanic glasses by Karl-Fischer titration. *Chemical geology*, 63:335–340, 1987. URL http://www.sciencedirect.com/science/article/pii/0009254187901707.

[185] H. R. Westrich and Eichel. Gas transport and bubble collapse in rhyolitic magma: an experimental approach. *Bulletin of Volcanology*, 56:447–458, 1994. URL `http://www.springerlink.com/index/QMQ1786137137826.pdf`.

[186] Andrew W. Woods and Takehiro Koyaguchi. Transitions between explosive and effusive eruptions of silicic magmas. *Nature*, 370(6491):641–644, August 1994. ISSN 0028-0836. doi: 10.1038/370641a0. URL `http://www.nature.com/doifinder/10.1038/370641a0`.

[187] H. M. N. Wright, Katharine V. Cashman, P. a. Mothes, M. L. Hall, a. G. Ruiz, and J.-L. Le Pennec. Estimating rates of decompression from textures of erupted ash particles produced by 1999-2006 eruptions of Tungurahua volcano, Ecuador. *Geology*, 40(7):619–622, May 2012. ISSN 0091-7613. doi: 10.1130/G32948.1. URL `http://geology.gsapubs.org/cgi/doi/10.1130/G32948.1`.

[188] Heather M. N. Wright, Jeffery J. Roberts, and Katharine V. Cashman. Permeability of anisotropic tube pumice: Model calculations and measurements. *Geophysical Research Letters*, 33(17):2–7, 2006. ISSN 0094-8276. doi: 10.1029/2006GL027224. URL `http://www.agu.org/pubs/crossref/2006/2006GL027224.shtml`.

[189] HeatherM.N. Wright, KatharineV. Cashman, Mauro Rosi, and Raffaello Cioni. Breadcrust bombs as indicators of Vulcanian eruption dynamics at Guagua Pichincha volcano, Ecuador. *Bulletin of Volcanology*, 69(3):281–300, 2007. ISSN 0258-8900. doi: 10.1007/s00445-006-0073-6. URL `http://dx.doi.org/10.1007/s00445-006-0073-6`.

[190] R. J. Wysoczanski and K Tani. Spectroscopic FTIR imaging of water species in silicic volcanic glasses and melt inclusions: An example from the Izu-Bonin arc. *Journal of Volcanology and Geothermal Research*, 156:302–314, 2006.

[191] S. Yamashita. Experimental Study of the Effect of Temperature on Water Solubility in Natural Rhyolite Melt to 100 MPa. *Journal of Petrology*, 40(10):1497–1507, October 1999. ISSN 0022-3530. doi: 10.1093/petroj/40.10.1497. URL `http://www.petrology.oxfordjournals.org/cgi/doi/10.1093/petroj/40.10.1497`.

[192] Shumpei Yoshimura and Michihiko Nakamura. Diffusive dehydration and bubble resorption during open-system degassing of rhyolitic melts. *Journal of Volcanology and Geothermal Research*, 178(1):78–87, 2008. ISSN 0377-0273. doi: 10.1016/j.jvolgeores.2008.01.017. URL `http://dx.doi.org/10.1016/j.jvolgeores.2008.01.017`.

[193] Shumpei Yoshimura and Michihiko Nakamura. Chemically driven growth and resorption of bubbles in a multivolatile magmatic system. *Chemical Geology*, 276

(1-2):18–28, September 2010. ISSN 00092541. doi: 10.1016/j.chemgeo.2010.05.010. URL http://linkinghub.elsevier.com/retrieve/pii/S0009254110001749.

[194] Youxue Zhang. H2O in rhyolitic glasses and melts: measurement, speciation, solubility, and diffusion. *Reviews of Geophysics*, 37(4):493–516, 1999. URL http://www.agu.org/pubs/crossref/1999.../1999RG900012.shtml.

[195] Youxue Zhang. H 2 O in Rhyolitic Glasses and Melts: Measurement, Speciation, Solubility, and Diffusion. *Reviews of Geophysics and Space Physics*, 37(4):493–516, 1999. ISSN 8755-1209. doi: 10.1029/1999RG900012. URL http://www.agu.org/pubs/crossref/1999/1999RG900012.shtml.

[196] Youxue Zhang and H. Ni. Diffusion of H, C, and O Components in Silicate Melts. *Reviews in Mineralogy and Geochemistry*, 72(1):171–225, November 2010. ISSN 1529-6466. doi: 10.2138/rmg.2010.72.5. URL http://rimg.geoscienceworld.org/cgi/doi/10.2138/rmg.2010.72.5.

[197] Youxue Zhang, Edward M Stolper, and G Wasserburg. Diffusion of water in rhyolitic glasses. *Geochimica et Cosmochimica Acta*, 55(2):441–456, 1991. ISSN 00167037. doi: 10.1016/0016-7037(91)90003-N. URL http://linkinghub.elsevier.com/retrieve/pii/001670379190003N.

[198] Youxue Zhang, Z Xu, and Harald Behrens. Hydrous species geospeedometer in rhyolite: improved calibration and application. *Geochimica et Cosmochimica Acta*, 64 (19):3347–3355, 2000. URL http://linkinghub.elsevier.com/retrieve/pii/S0016703700004245.

[199] Youxue Zhang, Z Xu, M Zhu, and Haoyue Wang. Silicate melt properties and volcanic eruptions. *Rev. Geophysics*, 45(2006):1–27, 2007. doi: 10.1029/2006RG000216.1. URL http://www.umich.edu/~youxue/publications/Zhang2007RG.pdf.